Scientific Technical Report

Seismic Structure of the Central Andean Subduction Zone from Local Earthquake Data

Dissertation
zur Erlangung des Grades eines Doktors
der Naturwissenschaften
am Fachbereich Geowissenschaften
der Freien Universität Berlin

vorgelegt von
Bernd Schurr (M.Sc.)

2000

Es ist gleich, ob einer mit dem Preßlufthammer oder an seiner Schreibmaschine verzweifelt. Nur die Theorien verstümmeln, was doch so klar ist, die Philosophien und die Wissenschaften insgesamt, die sich der Klarheit in den Weg stellen mit ihren unbrauchbaren Erkenntnissen.

— Thomas Bernhard, Der Keller

Abstract

The central Andes are formed by a complex interaction of both subduction related and tectonic processes on a lithospheric scale. In this thesis, the deep structure of the entire mountain range and underlying subduction zone has been investigated with local earthquake data.

Seismologic data from the PUNA experiment, a temporary array of 60 seismographs deployed across the Andes at approximately 23.5°S, were analyzed. P and S arrival times of 426 intermediate depth earthquakes were inverted for 1-D average velocity structure and hypocentral coordinates. Average velocities and v_p/v_s in the crust are low, indicating a felsic composition. Average mantle velocities are high but difficult to interpret because of the presence of a fast velocity slab at depth. Although the hypocenters sharply define a 35° dipping Benioff zone, seismicity in the slab is not continuous. The spatial clustering of earthquakes is thought to reflect inherited heterogenities of the subducted oceanic lithosphere. Additionally, 57 crustal earthquakes were located. Seismicity concentrates in the fold and thrust belts of the foreland and Eastern Cordillera, and along and south of the El Toro-Olacapato-Calama Lineament (TOCL), a major shear zone cutting through the entire Andes. Focal mechanisms of two earthquakes at this structure exhibit left lateral strike-slip mechanisms similar to the suggested kinematics of the TOCL. Further seismicity in the Puna is restricted to the area south of the TOCL.

Data from the PUNA network were merged with data from the earlier PISCO and ANCORP experiments for a combined tomographic inversion. Although the deployments did not coincide in time, spatial overlap was achieved by re-occupying existing sites. Travel times and t^* operators from P wave spectra of about 1600 earthquakes were inverted for 3-D models of v_p, v_p/v_s, and P wave attenuation. All three attributes provide a consistent image of the entire subduction zone on a lithospheric scale. The tomographic images reveal low velocities and high attenuation in crust and mantle underlying the Western Cordillera and most of the Puna plateau, indicative of weak rheology and mostly asthenospheric mantle. In contrast, forearc and eastern foreland are characterized by high Q_p values, in accordance with thermal models.

The lithosphere beneath the Atacama depression was found to be seismically very strong. It is believed to be an old, cold structure, that displaces hot isotherms and also the volcanic front a 100 km to the east. Although the block has clearly subsided, its seismic properties are hard to reconcile with extension and crustal thinning as has been suggested in previous studies. Instead, it is proposed that the block subsides as a whole along weak zones, characterized by low velocities and low Q_p values, surrounding it.

Low Q_p regions in mantle and crust are interpreted as indicating presence of aqueous fluids and partial melts. Continuous anomalies connect the different earthquake clusters in 100 and 200 km depth and the active volcanoes in the Western Cordillera and in the backarc. It is suggested that water is conveyed into the mantle wedge due to earthquake ruptures that may trigger hydro-fracturing. Water then fluxes melting in the hot mantle wedge. Melt ascent ways, as imaged by seismic Q_p, are not straight up to the base of volcanoes, as is often implicitly assumed. Instead, melt sources are located on significantly different depth levels, and ascent ways follow different patterns and cover significant horizontal distance.

Between 23°S and 24°S, a high velocity, high Q_p structure beneath the Eastern Cordillera and eastern Puna is interpreted as delaminating and detaching continental lithosphere that has been thickened in the orogenic process. South of this structure, the mantle is characterized by low velocities, high v_p/v_s ratios, and low Q_p values. It is believed that here lithosphere originally underlying Andean crust has already been removed. This is supported by new estimates of crustal thickness and volcanic activity. It is proposed that lithospheric delamination beneath the Puna is sanctioned by inherited weak lithospheric rheology and weakening due to pure shear deformation.

Zusammenfassung

Die zentralen Anden wurden in einem komplexen Zusammenspiel subduktions-typischer und tektonischer Prozesse gebildet. Die tiefe Struktur des gesamten Orogens und der darunterliegenden Subduktionszone wurde in dieser Arbeit mit lokalen Erdbebendaten untersucht.

Seismologische Daten des PUNA Experimentes, eines temporären Netzes von 60 Seismografen verteilt über die gesamten Anden bei 23,5° südlicher Breite, wurden analysiert. P und S Laufzeiten von 426 mitteltiefen Erdbeben wurden nach einem 1-D Geschwindigkeitsmodell und Hypozentralparametern invertiert. Durchschnittliche Geschwindigkeiten und v_p/v_s Verhältnisse in der Kruste sind niedrig und legen eine felsische Zusammensetzung der Gesteine nahe. Geschwindigkeiten im Mantel sind hoch, aber schwierig zu interpretieren wegen der seismisch schnellen subduzierten ozeanischen Platte. Obwohl die Hypozentren im Querschnitt eine scharf umrissene Benioffzone definieren, konzentriert sich die Seismizität in vereinzelten Schwärmen, die eventuell Schwächezonen in der subduzierten Platte widerspiegeln. Es wurden auch 57 krustale Erdbeben lokalisiert. Seismizität konzentriert sich entlang den Faltungsgürteln des Vorlandes und der Ostkordillere und entlang und südlich des El Toro-Olacapato-Calama Lineaments (TOCL), einer großen trans-andinen Scherzone. Die Herdmechanismen zweier Erdbeben an dieser Struktur sind dextrale Blattverschiebungen, ähnlich der vermuteten Bewegungsrichtung der Störung. Die weitere krustale Seismizität im Plateau ist auf den Bereich südlich des TOCL's begrenzt.

PUNA Daten wurden mit Daten von den vorangegangenen PISCO und ANCORP Experimenten kombiniert und in einer tomografischen Inversion verwendet. Obwohl die Netze zu verschiedenen Zeiten betrieben wurden, konnte räumliche Überschneidung durch das Wiederbesetzen früherer Standorte erreicht werden. Laufzeiten und t^* Operatoren aus P-Wellen Spektren von ungefähr 1600 Erdbeben wurden nach 3-D Modellen für v_p, v_p/v_s und P-Wellen Absorption invertiert. Die drei Parameter liefern ein konsistentes Bild der gesamten Subduktionszone im Lithosphärenmaßstab. Die tomografischen Querschnitte zeigen niedrige Geschwindigkeiten und hohe Dämpfung in Kruste und Mantel unterhalb

des vulkanischen Bogens und des Puna Plateaus. Dies deutet auf eine schwache Rheologie und hauptsächlich asthenosphärischen Mantel hin. Im Gegensatz dazu weisen der *forearc* und das östliche Vorland, wie von thermischen Modellen erwartet, hohe Q_p Werte auf.

Die Lithosphäre unterhalb der Atacama-Depression konnte als seismisch besonders fest identifiziert werden. Es wird angenommen, daß sie eine alte, sehr kalte Struktur darstellt, die die heißen Isothermen und den vulkanischen Bogen 100 km nach Osten verschiebt. Obwohl sich der Atacamablock sicherlich abgesenkt hat, sind seine seismische Eigenschaften nicht mit Extension und Krustenverdünnung zu vereinbaren. Es wird angenommen, daß sich der Block als Ganzes entlang der ihn umgebenden Schwächezonen senkt.

Bereiche hoher Dämpfung im Mantel und in der Kruste deuten wahrscheinlich auf wässrige Fluide und partielle Schmelzen hin. Kontinuierliche Anomalien verbinden die Erdbebenschwärme in 100 und 200 km Tiefe mit den aktiven Vulkanen der Westkordillere und des *backarcs*. Es wird vorgeschlagen, daß Wasser durch Erdbeben induzierte *hydro-fractures* von der subduzierten Platte in den Mantel transportiert wird. Das Wasser induziert dann Schmelzen im heißen Mantelkeil. Die durch Q_p abgebildeten Aufstiegswege der Schmelzen verlaufen nicht, wie meist angenommen, senkrecht zu den Vulkanwurzeln, sondern Schmelzen entspringen in verschiedenen Tiefen und legen größere horizontale Wege zurück.

Zwischen 23°S und 24°S wird eine Zone hoher Geschwindigkeiten und hohen Q_p's unter der Ostkordillere und der Puna als sich ablösende verdickte kontinentale Lithosphäre interpretiert. Südlich dieser Struktur weist der Mantel niedrige Geschwindigkeiten, hohe v_p/v_s Verhältnisse und niedrige Q_p Werte auf. Es wird vorgeschlagen , daß hier die Mantellithosphäre, die ursprünglich unterhalb der andinen Kruste lag, schon abgelöst wurde. Dies Annahme wird bestärkt durch neue Schätzungen der Krustendicke und durch vulkanische Aktivität. Es wird vorgeschlagen, daß lithosphärische Delamination unter der Puna durch eine bereits vorhandene schwache lithosphärische Rheologie und durch Schwächung aufgrund von *pure shear* Deformation ermöglicht wird.

Resumen

Los Andes Centrales están formados gracias a una compleja interacción entre procesos tectónicos y relativos a la subducción a escala litosférica. En esta tesis se ha estudiado la estructura profunda de todo el orógeno y de la zona de subducción inferior con datos de los sismos locales.

Se han analizado los datos sismológicos del experimento PUNA, en base a una red de 60 sismógrafos repartidos a lo largo de los Andes, aproximadamente en los 23.5° de latitud sur. Los tiempos de transmisión P y S de 426 sismos localizados a media profundidad se invirtieron por un modelo unidimensional de velocidad y coordenadas hipocentrales. El promedio de velocidades y la relación v_p/v_s en la corteza son bajas y dan indicios de una composición félsica. El promedio de velocidades en el manto es alto, no obstante dificil de interpretar debido a la alta velocidad sísmica de la placa oceánica. A pesar de que los hipocentros muestran claramente la zona de Benioff, la seismicidad se concentra en grupos aislados que en ocasiones presentan zonas débiles en la placa de subducción. Se localizaron 57 sismos en la corteza. La seismicidad se concentra en las cadenas de pliegues y cabalgamientos del antepaís y de la Cordillera Este, así como a lo largo y al sur del Toro-Olacapato-Calama Lineament (TOCL), una gran zona transandina de cizallamiento. Los mecanismos focales de dos sismos en esta estructura muestran una falla lateral parecida a la cinemática del TOCL. El resto de la seismicidad en la Puna tiene su límite en el área al sur del TOCL.

Los datos del PUNA han sido combinados con otros de experimentos anteriores: PISCO y ANCORP y utilizados en una inversión tomográfica. A pesar de que las redes estuvieron en funcionamiento durante periodos distintos, se logró la superposición espacial reocupando antiguos puntos existentes. Los tiempos de transmisión y los operadores t^* de ondas P espectrales de aproximadamente 1600 terremotos fueron invertidos por modelos tridimensionales de v_p, v_p/v_s y atenuación de ondas P. Los tres parámetros proporcionan una imagen consistente de toda la zona de subducción a escala litosférica. Las imágenes tomográficas revelan bajas velocidades y altas atenuaciones en la corteza y el manto por debajo de la Cordillera del Oeste y la Meseta de la Puna, lo que indica la existencia de

una reología débil y de un manto principalmente astenosférico. Por el contrario el fore-arc y el antepaís del este se caracterizan por altos valores Q_p, conforme a modelos termales.

La litosfera por debajo de la Depresión de Atacama se distingue por una fuerte reología. Se supone que representa una estructura vieja y fría que desplaza las isotermas de temperaturas elevadas y el frente volcánico unos 100 km hacia el Este. A pesar de que el bloque de Atacama está claramente hundido, sus propiedades sísmicas son difíciles de conciliar con la extensión y afinamiento de la corteza propuestos en anteriores estudios. De otro modo se sugiere el hundimiento del bloque a lo largo de las zonas débiles circundantes, caracterizadas por bajas velocidades y bajos valores Q_p.

Las regiones de bajos Q_p en el manto y la corteza se interpretan como indicadores de la presencia de fluídos acuosos y mezclas fundidas parcialmente. Continuas anomalías unen los diferentes grupos sísmicos en una profundidad de 100 y 200 km con volcanes activos de la Cordillera Oeste y del back-arc. Se sugiere además que el agua es transportada de la placa de subducción al manto debido a las fracturas hidráulicas generadas por los sismos. El agua induce la fusión en la cuenca caliente del manto. Los caminos ascendentes que siguen los fluidos no suben perpendiculares a la base del volcán, como normalmente se supone, sino que por el contrario los fluidos están localizados a diferentes niveles y atraviesan horizontalmente largas distancias.

Una zona de altas velocidades y altos Q_p por debajo de la Cordillera Este y de la Puna situada entre los 23° y 24° de latitud sur se interpreta como litosfera continental separada y engrosada durante el proceso orogénico. Al sur de esta estructura, el manto se caracteriza por sus bajas velocidades, altas relaciones v_p/v_s y bajos valores Q_p. Se supone que aquí la litosfera, que originariamente se encontraba debajo de la corteza andina, se ha despegado. Nuevas estimaciones sobre la densidad de la corteza y de la actividad volcánica corroboran esta suposición. Se sugiere que la delaminación litosférica por debajo de la Puna es favorecida por la existencia de una reología litosférica débil y por una debilitación a causada pa la deformación del *pure shear*.

Contents

Chapter 1

Introduction

Subduction zones, with their graceful volcanic arcs, and largest (Chile 1960, Alaska 1964) and deepest (almost 700 km) earthquakes, are the most spectacular expression of plate tectonic theory. Cold oceanic lithospheric plates, that sink into the deep mantle in subduction zones, represent the down-welling limbs of mantle convection, and their negative buoyancy (slab pull) is a driving force for plate motions. Subduction zones are regions of complex mass transfer between crust, mantle, hydrosphere, and atmosphere. Arc volcanism that almost universally accompanies subduction, makes the most important contribution to formation of continental crust, and cycling of volatiles and rare earth elements into the deep mantle at subduction zones significantly influences the bulk composition of the earth.

Not surprisingly, subduction zones have been the object of vigorous research in all geoscientific disciplines since their discovery more than three decades ago. Nonetheless, many basic processes governing the subduction system are still not well understood. Why does arc volcanism occur above cold descending slabs that chill the surrounding mantle? It is now widely accepted that volatiles carried along in the subducted sediments, crust, and oceanic mantle play an utmost important role for most of the phenomena accompanying subduction. For example, H_2O released from the subducted slab, might ultimately be responsible for subduction zone earthquakes by reducing normal stresses, as well as for magmatism by reducing the solidus temperature of peridotite.

Temperature and volatiles, the most important factors in the subduction system, also strongly influence the elastic and anelastic behavior of rocks, and consequently seismic wave propagation. This can be exploited in seismology to derive their spatial distribution by imaging acoustic- and shear-wave speed, impedance contrasts or attenuation of seismic energy. Seismic wave velocity and attenuation are sensitive indicators of lithology, rheology, and the state of earth's crust and mantle. This information is invaluable in tackling

geodynamical problems.

In this thesis the subduction zone of the Central Andes is studied. The Andes have formed in a complex interplay of subduction related and tectonic processes. The Central Andes with the associated Altiplano-Puna high plateau constitute the second largest continental land-mass on earth, rivaled only by the Tibetan highland. Whereas in the case of the Himalayas, where two buoyant continental plates collide, crustal thickening and uplift is quite intuitive, processes leading to formation of a plateau above a subduction zone are puzzling.

These topics have been in the focus of the Collaborative Research Center (SFB 267) "Deformation Processes in the Andes", an interdisciplinary research initiative established in 1993 by researchers of Berlin and Potsdam. Since then, a multitude of geologic, petrologic, geodetic, and geophysical data have been acquired and analyzed to decipher the geologic and tectonic evolution of the Andean region. The above questions are also the topic of this thesis, that is based on analysis of seismological data collected within the SFB 267.

In the beginning of this work, a short overview of the geologic history of the subduction zone is provided. Emphasis is given to the period between Miocene time and present, in which the present subduction geometry has been in place, and in which the high plateau has been uplifted. It follows a short presentation of current geodynamic concepts and models on Andean plateau formation.

In Chapter 3, new earthquake data from a temporary, passive seismic experiment, deployed within the SFB 267 on the Puna plateau of north-western Argentina, are analyzed. Earthquakes inside the subducted Nazca plate are located with high precision, and focal mechanisms that describe stresses acting on the slab are computed. In addition, crustal seismicity in the plateau and adjacent foreland is analyzed. These data constitute the first estimate on present-day deformation of the Puna plateau. A shortened version of this Chapter has been published in *Geophysical Research Letters* [*Schurr et al.*, 1999].

Chapter 4, comprises the largest part of the thesis. Data from three seismic experiments are combined and used in local earthquake tomography. Three dimensional models of acoustic- and shear-wave speed, as well as *P*-wave attenuation are derived for the entire subduction zone from forearc to backarc. Similar high resolution models exist only for the extensively studied Japanese subduction zone. The models give a quite consistent picture, that contributes to a better understanding of both, general subduction related processes, i.e. fluid and magma generation, as well as Andean specific topics, i.e. lithospheric structure and shortening. In addition to a general discussion of the results, three topics are picked out and treated in more detail: The deep seismic structure and probable

evolution of the Atacama depression, the sources and ascent ways of fluids and melts in the Central Andean subduction zone, and the role of the mantle lithosphere in Andean mountain building. The Thesis is concluded with an outlook on remaining questions and possible avenues of future research.

Chapter 2

Geodynamic Setting of the Central Andes

2.1 Tectonic Setting of the Andes

The Andean mountain chain stretches over about 5000 km from the Caribbean to Tierra del Fuego along the western margin of South America. Rising from an over 8000 m deep deep-sea-trench to almost 7000 m high peaks, their relief is the highest on earth. The Andes are the most popular example of an active continental plate margin. They are name-giving to the whole class of oceanic plate subduction beneath continental lithosphere: the Andean- or Cordilleran-type margins. The oceanic Nazca plate that is presently subducted beneath South America, is separated by three spreading centers from other oceanic plates: To the north by the Galapagos ridge from the Cocos plate, to the east by the fast spreading East Pacific Rise from the Pacific plate, and to the south by the Chile ridge from the Antarctic plate. Presently, the Nazca plate moves at a rate of 5.1 cm/yr to the east, while the South American continent overrides it at 3.4 cm/yr westwards with respect to the absolute hot-spot reference frame [*DeMets et al.*, 1990]. This results in a slightly oblique ENE directed convergence between the two plates with a velocity of 8.5 cm/yr (Figure 2.1). Off the Central Andes, the currently subducted portion of the ocean floor is with 40 – 46 Ma [*Müller et al.*, 1997] relatively young.

2.2 Morpho-Tectonic Units of the Central Andes

The Andes are not a single homogeneous tectonic entity, but exhibit significant along and across strike variation in tectonic style, uplift history, and magmatism. Major along strike
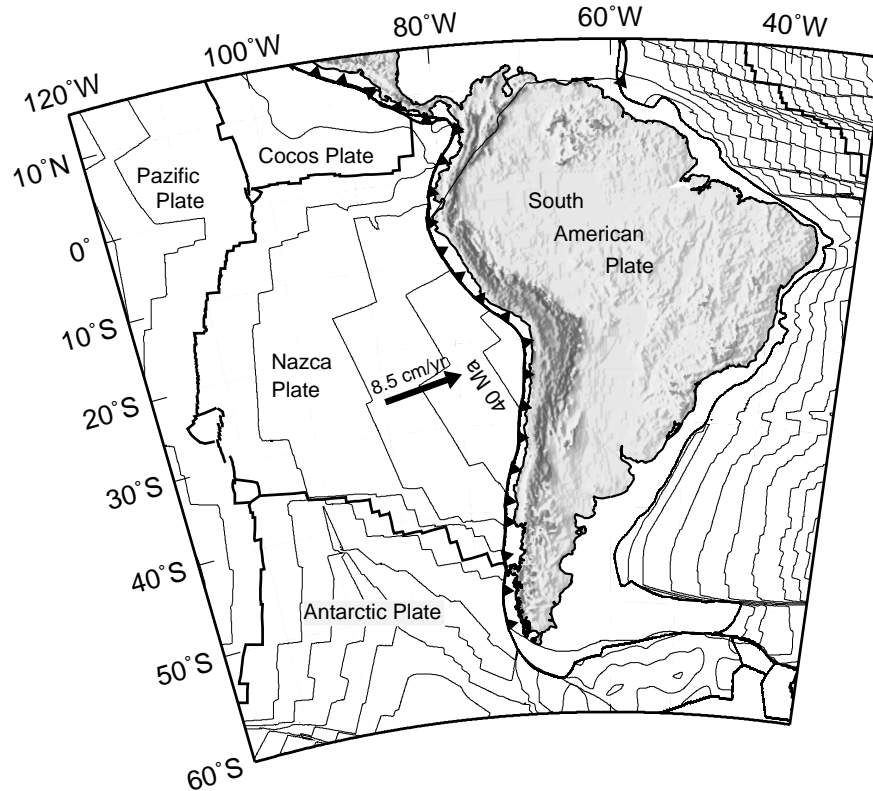
Figure 2.1: Plate-tectonic setting around the South American continent. Thick lines are spreading ridges and transform plate boundaries, convergent margins are indicated by barbed lines. Ocean-age isochrons are shown for every 10 Ma. Currently, 46 Ma old oceanic Nazca lithosphere is subducted at a rate of $\approx$ 8.5 cm/yr beneath the central Andes [*DeMets et al.*, 1990].

segmentation mainly reflects a varying geometry of the subducted Nazca plate. Between latitudes 2°S–15°S and 28°S–33.5°S, the Nazca plate subducts almost flat (5° – 10°), whereas elsewhere it subducts at an intermediate angle of about 30° (Figure 2.2). The flat slab regions lack volcanic activity since the late Miocene. Above the three steeply dipping segments of oceanic crust, active volcanic regions are referred to as northern, central, and southern volcanic zone (NVZ, CVZ, and SVZ) respectively. In general, Andean domains coincide with these zones, i.e. the NVZ corresponds to the Northern Andes, the CVZ and flanking flat slab regions correspond to the Central Andes, and the SVZ corresponds to the Southern Andes. While the Northern and Southern Andes form narrow mountain belts, the Central Andes are characterized by a more than 3000 m high and about 300 –

400 km wide plateau (Figure 2.2).

Our study area lies in the Central Andes between 20°S and 25°S, south of the marked bend in the South American coastline near Arica (Figure 2.2). Here, the forearc consists of the Coastal Cordillera that is separated from the Precordillera by the Longitudinal Valley (Figure 2.3). The Western Cordillera (WC) forms the present magmatic arc and constrains the central Andean plateau to the east. Here, the plateau is the substrate of Miocene to recent strato-volcanoes which include the world's highest active volcano (Mt. Llullaillaco, 6723 m, 24.7°S).

The backarc consists of a high plateau, the Miocene fold and thrust belt of the Eastern Cordillera (EC), and a compressional foreland. The high plateau is divided into the Altiplano of Peru and Bolivia in the north and the north-west Argentine Puna in the south. The Altiplano is an internally drained basin with an average elevation of ≈ 3500 m and little topography, confined by the Western and Eastern Cordilleras. By contrast, the Puna is characterized by a more rugged relief and an average elevation about 1 km higher than the Altiplano. The forelands of both plateau areas differ also in their deformational style: East of the Altiplano, the Subandean Ranges form an active thin-skinned fold and thrust belt. East of the Puna, in the Santa Barbara Ranges, deformation involves also basement rocks. The transition between these two segments occurs approximately between 22°S and 23°S.

2.3   Tectonic history of the Central Andes

2.3.1   Jurassic to Oligocene history (200–25 Ma)

Subduction of oceanic lithosphere beneath the South American Continent has occurred continously for more than 200 Ma under varying convergence parameters. The present forearc consists of rocks that record a progressive eastward migration of magmatic arcs probably as a result of retreat of the oceanic margin due to tectonic erosion [*von Huene & Scholl*, 1991]. The oldest igneous rocks, the Jurassic volcanic rocks of the Coastal Cordillera, were deposited on sea level [*Scheuber et al.*, 1994]. During early Cretaceous time, the center of igneous activity shifted to the former backarc into the Longitudinal Valley (Figure 2.3). Subduction of the spreading ridge between the ancient Aluk and Farallon plates caused a change from an tensional stress regime in the Jurassic to a compressional one.

In late Eocene time, the magmatic arc shifted again eastward onto the present Precordillera. The arc was affected by a period of intense deformation known as the Incaic
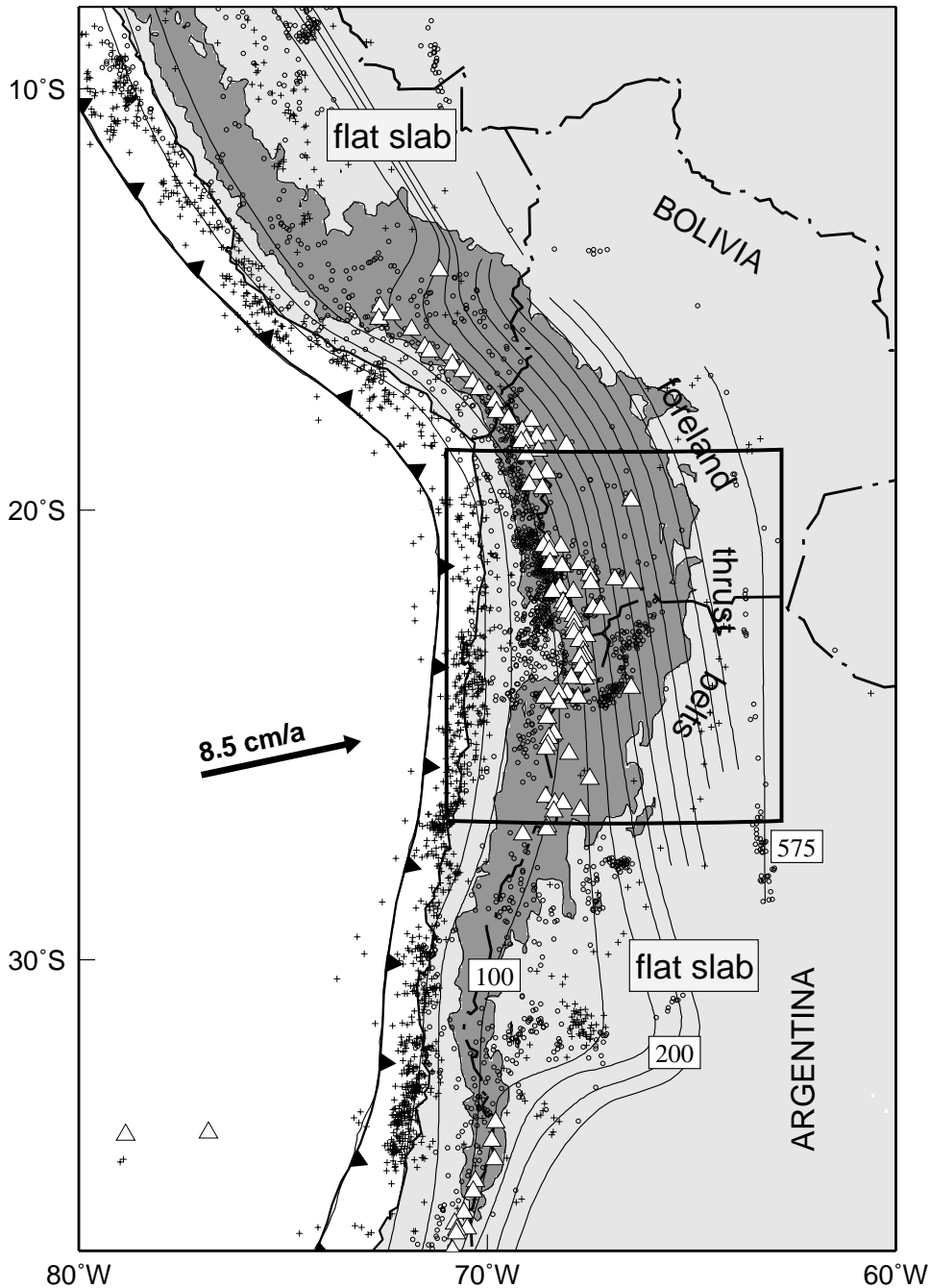
Figure 2.2: Overview of the central Andean subduction zone. Regions above 3000 m are dark grey, indicating the approximate extent of the Central Andean Plateau. Contour lines show the depth of the Wadati-Benioff-Zone [*Cahill & Isacks*, 1992]. White triangles indicate active volcanoes. Well located earthquakes of the last 30 years [*Engdahl et al.*, 1998] are plotted for the mantle as circles (depth $\geq$ 40 km) and the crust as crosses (depth $\leq$ 40 km). Crustal seismicity is confined to the seismogenic part of the subduction zone and the foreland thrust belts. The study area and extent of Figure 2.3 is outlined by the rectangle. The highly symmetrical Central Andean Plateau lies above a region of moderately steep (30°) subduction and is flanked by regions of flat subduction. Above the flat slab there is no recent volcanism.
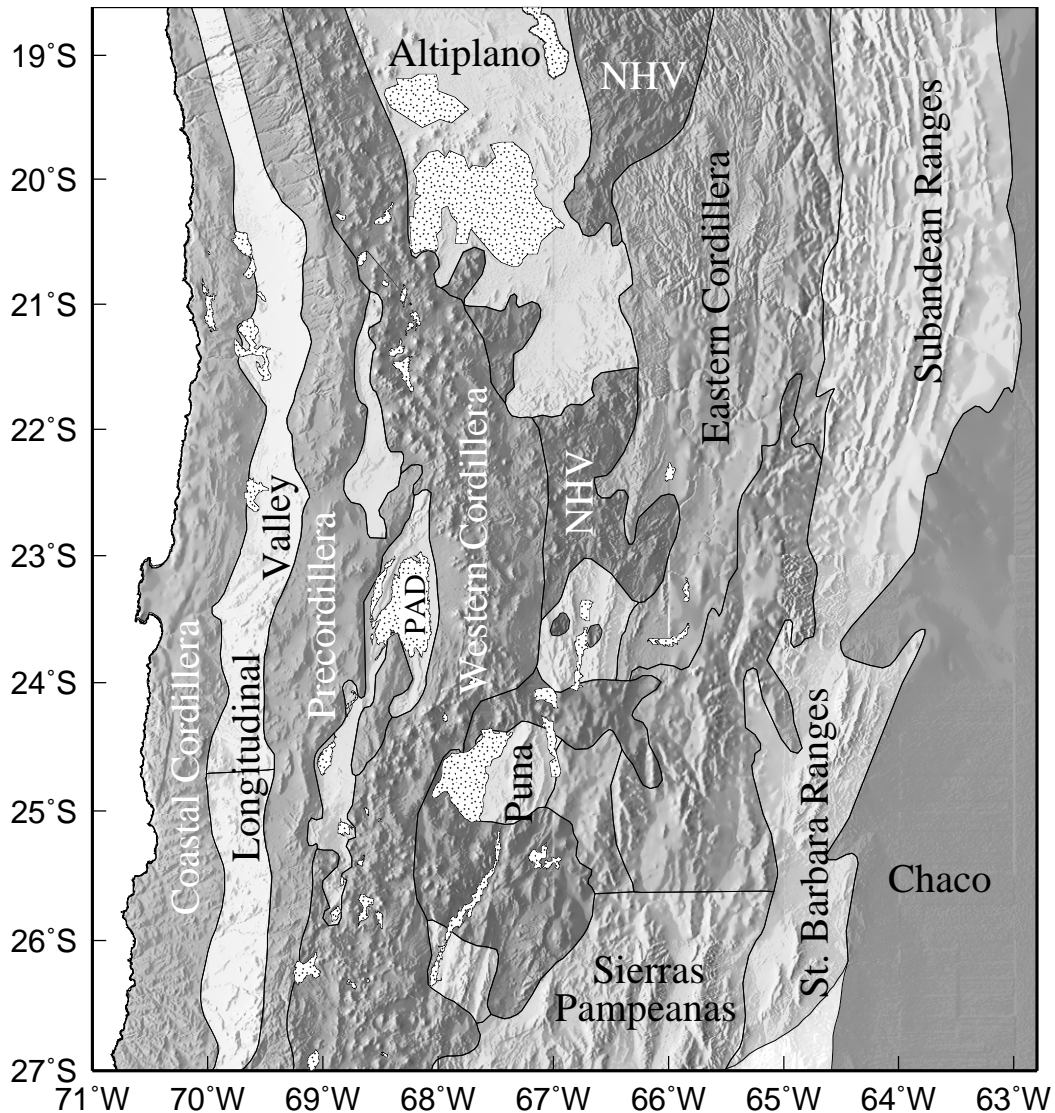
Figure 2.3: Morpho-Tectonical units of the Central Andes after *Reutter & Götze* [1994]. Dotted areas are salt pans. PAD abbreviates the Pre-Andean Depression, NHV stands for Neogene-Holocene Volcanic rocks.

tectonic phase, that initiated as a result of rapid increase in the rate of plate convergence. Both arc-parallel strike-slip movements along the Precordilleran Fault System [*Reutter et al.*, 1996], and arc-normal shortening is documented. Deformation affected also the backarc region and the EC [*Lamb et al.*, 1997]. Up to 5 km thick sediments have been deposited into the compressional basins of the proto-Altiplano [*Allmendinger et al.*, 1997]. At 25 Ma, the Western Cordillera may have reached up to 50% of its present elevation [*Gregory-Wodzicki*, 2000].

2.3.2   Miocene to Holocene history (25 Ma to present)

Magmatism

Following magmatic quiescence in the Oligocene [*Coira et al.*, 1982], magmatic activity shifted eastward to its present location, the WC. In places, volcanic activity reaches as far east as the EC. The oldest igneous rocks are about 28 Ma. From late Oligocene to early Miocene time (26 – 16.5 Ma), volcanism south of 25°S is restricted to the WC, between 24°S–25°S and north of 22°S, it extends across the plateau to the EC. Between 22°S–24°S, where presently the magmatic arc is displaced some 100 km to the east by the Atacama depression, there was a gap in magmatic activity. Magmas are andesitic to dacitic, but also basaltic to mafic in the backarc.

During middle Miocene (16 – 12 Ma), dacitic to andesitic eruptions spread across the backarc plateau in the southern Puna and Altiplano and small granitoid stocks and extrusive domes were emplaced between 22°S–24°S. Backarc mafic magmatism ceased in the entire region, while in the WC, stratovolcanoes continued to erupt south of 25°S and ignimbrites were deposited north of 21°S.

In late Miocene (12 Ma), an intense flare-up of voluminous ignimbrite eruptions started and lasted until late Pliocene (3 – 2 Ma). Huge volumes erupted from collapse calderas defining the NW-SE trending transverse volcanic zones across the plateau [e.g., *Riller et al.*, 2000]. Of particular importance is the magmatic activity between 21.5°S and 23°S, referenced as Altiplano-Puna Volcanic Complex (APVC) by *de Silva* [1989]. The onset of this volcanism has been attributed to an increase in convergence rate [*de Silva*, 1989], or to a steepening of the subducted slab [*Kay et al.*, 1995]. In contrast, *Riller et al.* [2000] argue for the onset of strike-slip faulting, as a result of the transition in the deformation regime from vertical thickening to orogen-parallel stretching on the plateau. Strike-slip faults apparently tapped mid-crustal magma chambers and triggered ignimbrite eruptions. Other important centers of ignimbrite volcanism located away from the APVC include the Los Frailes Volcanic fields in the eastern Altiplano (20°S, 66°W) and the Cerro Galán volcanic complex in the southern Puna (26°S, 67°W).

During the youngest period (2 Ma to present) of Central Andean magmatism, andesitic to dacitic composite stratovolcanic dome complexes erupted in the WC. Mafic monogenetic cones and fissure flows occurred in the backarc. Based on trace-element characteristics, *Kay et al.* [1994] distinguished three volcanic groups: An intra-plate group erupted above the current seismic gap in the southern Puna (26°S–27°S, Cerro Galán). To a first degree they are the most voluminous and are also the highest percent melt. Intermediate volume calc-alkaline lavas are found just to the north, south, and west of the intra-plate flows. Further to the north, at 24°S, small shoshonitic flows occur locally along the El Toro

fault zone. The change from shoshonitic chemistry to calc-alkaline to intra-plate-type basalts from north to south is regarded evidence for lithospheric thinning. Based on the particular chemistry of these mafic magmas, geophysical data [*Whitman et al.*, 1992], and because horizontal crustal extension is very limited, lithospheric delamination has been postulated to have occurred beneath the southern Puna [*Kay & Kay*, 1993].

Cerro Tuzgle in the easternmost Puna is the only Quaternary backarc strato-volcano. Its magmas formed by a complex mixing process in the mantle and thickened crust [*Coira & Kay*, 1993]. The Tuzgle volcanic rocks can be divided into two groups with different mantle precursors: an older, more voluminous rhyodacitic to mafic andesitic sequence and a younger andesitic one [*Coira & Kay*, 1993]. Cerro Tuzgle is situated directly above a vigorous earthquake cluster at a depth of about 200 km (Figure 2.2).

Deformation and Uplift of the Plateau

Uplift of the Altiplano/Puna plateau started probably in the Miocene (23 Ma), although the exact timing is difficult to establish. Tectonic shortening appears to have progressed from west to east. *Gregory-Wodzicki* [2000] reviewed estimates for the age and magnitude of uplift from a variety of sources. Fission-track data, indicative of tectonic denudation, from the EC of Bolivia suggest two cooling events, one at around 22 Ma and another around 10 – 15 Ma. Internal drainage may have developed as early as 25 Ma in the Altiplano and at 15 Ma in the southern Puna. The data that were revised in this respect seem to indicate that the WC was not more than half of its present elevation at 25 Ma. The Altiplano and EC may have reached 25 – 30% of their present altitude at 20 Ma and 14 Ma respectively. Uplift accelerated at 10 Ma during the so called Quechua tectonic phase, whereby the Altiplano and EC rose to about 2000 – 3500 m since then. Deformation in the EC is thought to have ended at $\approx$ 9 Ma based on an undeformed erosional surface [*Gubbels et al.*, 1993]. Deformation propagated then further east into the Subandean thrust-belts, where since then all upper-crustal deformation has been accomplished. In the Puna shortening began towards the end of the Oligocene [*Kraemer et al.*, 1999], and may be still active (Chapter 3.3.3).

The magnitude of horizontal shortening in the plateau and foreland varies considerably along strike. *Kley & Monaldi* [1998] summarized published and their own estimates for crustal shortening based on balanced cross-sections and compare these to shortening calculated from current topography. In their study, they assume isostatic equilibrium (crustal thickness $\propto$ topographic elevation), constant original crustal thickness of 40 km, and that all crustal thickening is due to tectonic shortening (Figure 2.4). There is a strong variation in measured crustal shortening related to the foreland structural style
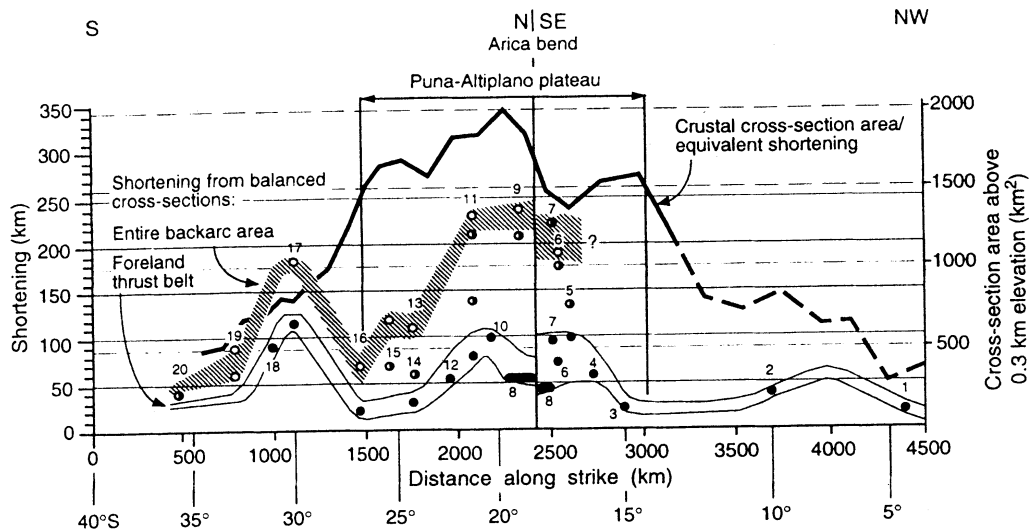
Figure 2.4: Along strike variation of horizontal shortening in the Central Andes. Equivalent shortening curve (thick black line) is calculated from crustal cross-section area, assuming all crustal thickening is tectonic. Shortening curves for backarc and foreland are derived from geologic shortening estimates. Note large discrepancies between crustal area and geologic shortening estimates north and south of the Arica bend [from *Kley & Monaldi*, 1998].

(i.e. thin-skinned vs. thick-skinned). Shortening magnitudes are consistently too low, and discrepancies between calculated and measured values increase drastically towards the northern and southern ends of the plateau. Maximum shortening is observed at the Arica bend at approximately 20°S. At 21°S *Schmitz* [1994] shows that up to 80% of the crustal thickness can be attributed to crustal shortening, whereas at 27°S *Grier et al.* [1991] can account only for 30%. Although there are significant sources of errors in estimating crustal shortening, the major discrepancies (the minima north and south of the Arica bend) are considered to be robust [*Kley & Monaldi*, 1998]. Particularly, in regions of thick-skinned foreland deformation, shortening is not sufficient to explain crustal thickness. Here, different processes have to be taken into account to explain the topography of the Central Andes. Lithospheric thinning, for example, may require a thinner crustal root, and thus also a smaller amount of shortening. Other possibilities include magmatic addition and under-plating, although this is difficult to reconcile for the backarc. Pre-Neogene shortening or lateral flow of lower crust from areas of excess vertical thickening may be viable options for the "missing" crustal thickness in some parts of the central Andes.

2.4 Geodynamic Models for the Formation of the Andean Plateau

The mechanisms responsible for generation and conservation of large continental plateaus is not well understood and widely discussed in geodynamic research. Among the proposed processes are tectonic shortening and under-plating, magmatic addition, lithospheric thinning, and hydration of mantle rocks. Due to its location above a subduction zone and associated abundant volcanism, formation of the central Andean plateau was originally attributed to magmatic processes [*James*, 1971]. However, in order to explain crustal thickness by magmatic addition, unrealistically large amounts of igneous rocks would be necessary. Analysis of Neogene deformation on the eastern margin of the plateau led to models that rely mostly on tectonic shortening and lithospheric thinning to explain crustal thickness and average elevation [*Isacks*, 1988; *Roeder*, 1988]. *Isacks* [1988] developed a two-stage model for thickening and uplift of the plateau (Figure 2.5): In *stage 1* the lithosphere underlying the current extent of the plateau has been thermally softened during an episode of low angle subduction. Note, that the inclination of the subducted slab is thought to have been the exact opposite from today: steep subduction to the north and south, with only a narrow swath of lithosphere thermally softened there, and low-angle to flat subduction inbetween. Deformation began around 25 Ma in the Altiplano and was distributed over the entire weakened part. In *stage 2* (12 - 6 Ma) shortening ceased on the plateau and shifted eastward, where the whole foreland is underthrust and driven into the plateau's lower crust like a hydraulic ram. Thus, upper crustal deformation is localized in the foreland thrust-belts, whereas the plateau surface lifts undeformed due to lower crustal ductile deformation. These two stages are sketched in Figure 2.5 taken from a more recent publication of *Gubbels et al.* [1993].

However, many new geophysical and geological investigations have revealed major along strike variations of lithospheric structure, timing and amount of shortening, deformational style, topography, and magmatism [e.g., *Whitman et al.*, 1992, 1996; *Kley & Monaldi*, 1998] that necessitate more complex models. While shortening in the Altiplano ceased and jumped eastward to form the thin-skinned foreland thrust belts 10 Ma ago as in *Isacks* [1988]'s model, deformation in the Puna has been active until as late as 2 Ma. Based on a rather qualitative, regional study of seismic Q using small aperture networks in the Jujuy and San Juan provinces, as well as a permanent seismic station in La Paz, Bolivia, *Whitman et al.* [1992] and *Whitman et al.* [1996] revealed generally high Q beneath the Altiplano and low Q beneath the Puna and interpreted these as different thicknesses of the respective mantle lids. A tomographic study of the Altiplano [*Myers et al.*, 1998] confirms the seismically weakly attenuating Altiplano lithosphere, but finds higher attenuation
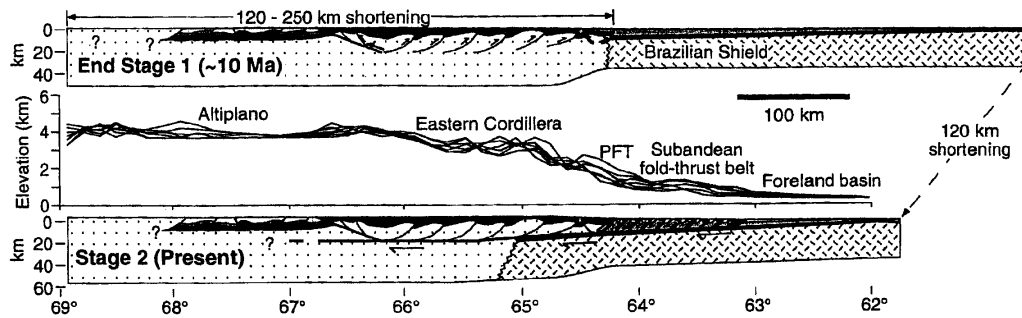
Figure 2.5: Two-stage model of plateau formation [*Isacks*, 1988]. In the first stage deformation is distributed in the plateau. In the second stage the foreland is underthrust beneath the plateau, upper crustal deformation jumps to the east, whereas the plateau rises without being substantially strained due to ductile deformation in the lower crust. From *Gubbels et al.* [1993].

beneath the Eastern Cordillera, which together with the the presence of ignimbrites in the Los Frailes Volcanic Field were taken as indication of locally delaminated lithosphere. These observations, however, are not unequivocal as very high heat flow [*Springer & Förster*, 1998] and high He^3/He^4 ratios [*Hoke et al.*, 1994] measured across the Altiplano have been interpreted in terms of thin lithosphere.

Nonetheless, differences in the state of mantle lithosphere beneath the northern and southern plateau are corroborated by changing patterns of backarc magmatism [*Kay et al.*, 1994, Chapter 1]. The absence of recent backarc volcanism in the Altiplano and the occurrence of shoshonitic to calc-alkaline to ocean-island-basalt-type lavas from the northern to southern Puna have also been taken as evidence for lithospheric thinning.

South of 22°S, where lithospheric thinning may commence, an important change in the style of foreland deformation occurs too. The thin-skinned Sub-Andean Ranges adjoining the Altiplano to the east are replaced by the thick-skinned St. Barbara Ranges that exhibit deep (up to 30 km) crustal seismicity [*Cahill et al.*, 1992; *Schurr et al.*, 1999], east of the Puna (Figure 2.3). These two different styles of upper crustal deformation have been interpreted as indicators for simple- and pure-shear modes of lithospheric shortening [*Allmendinger & Gubbels*, 1996], whereby each mode is controlled by inherited pre-Andean structure in basement and upper mantle. The pure-shear mode of deformation in the Puna provides no mechanism to transport cold lithosphere beneath the plateau, and also accommodates less shortening, in accordance with the two different mechanical states of plateau-lithosphere and southward decreasing shortening magnitudes [*Kley & Monaldi*, 1998, Figure 2.4].

These models are only applicable to the formation of the backarc plateau. The up to

60 km thick crust [*Wigger et al.*, 1991; *Graeber & Asch*, 1999; *Yuan et al.*, 2000] and high surface elevation of the forearc and arc though, require different processes. For the forearc, underplating of tectonically eroded crustal materials as well as hydration of peridotitic mantle, thus forming rocks with crust-like geophysical properties, have been suggested [*Giese et al.*, 1999]. For the Western Cordillera magmatic addition may be also important.

Chapter 3

Seismicity and Average Velocities beneath the Argentine Puna Plateau

3.1 The PUNA Experiment: Field Deployment and Data

The German lead Collaborative Research Center (SFB 267) "Deformation Processes in the Andes", an interdisciplinary initiative of several German geo-scientific research facilities[1] together with partners in South America,[2] carried out four passive seismic experiments between 1994 and 1997, deploying portable, mostly short-period, seismograph arrays between 20°S and 25°S from the Pacific coast across the Andean mountain range. The PISCO'94 (**P**royecto de **I**nvestigación **S**ismológica de la **C**ordillera **O**ccidental) seismic experiment was centered in the forearc region between 22°S and 24°S. It involved both an active part [*Schmitz et al.*, 1999] and a temporary passive array [*Graeber & Asch*, 1999; *Haberland & Rietbrock*, 2000]. The CINCA'95 (**C**rustal **I**nvestigación on- and off-shore **N**azca plate and **C**entral **A**ndes) campaign was aimed to investigate the seismogenic part of the subduction interface in the coastal region of Central Chile. An on-shore off-shore active source experiment [*Patzwahl et al.*, 1999], as well as a passive part involving both land- and ocean-bottom seismometer was conducted [*Husen et al.*, 1999; *Patzig*, 2000]. Ten days before the experiment started, the great M_w=8.0 Antofagasta earthquake [*Delouis et al.*, 1997] struck in the immediate vicinity of the study area. The

---

[1]Freie Universität Berlin, Technische Universität Berlin, Universität Potsdam, GeoForschungsZentrum Potsdam

[2]Universidád de Chile, Santiago, Chile; Universidád Cátolica del Norte, Antofagasta, Chile; Universidád Nacíonal de Salta, Argentina; Servicio Nacíonal de Geología y Míneria de Bolivia (SERGEOMIN), Bolivia

seismograph array recorded countless aftershocks [*Sobiesiak*, 2000]. The following year, the wide- and steep-angle traverse ANCORP'96 (**An**dean **C**ontinental **R**esearch **P**roject) [*ANCORP Working Group*, 1999], was again accompanied by an earthquake study. The passive array continued coverage of PISCO to the north, but additionally reached into the Bolivian backarc [*Rietbrock & Haberland*, 1998; *Haberland & Rietbrock*, 2000]. The seismological projects were flanked by a multitude of other geophysical, geological, petrological, and geodetic studies [*SFB-Berichtsband*, 1998].

So far activities were concentrated in the forearc and the Altiplano, producing detailed information about seismicity, stress distribution, subduction geometry, and crustal and lithospheric structure there. In contrast, the Argentine backarc region remained relatively unexplored. In the second half of 1997, a seismological experiment atop the Argentine Puna was conducted. The seismograph network stretched in N-S direction from the southern end of the Altiplano at 22°S to the gap in Benioff seismicity at roughly 25°S. In E-W direction it crossed the entire Andes, though with less dense coverage in the forearc region (Figure 3.1).

The PUNA (**P**lateau **U**ntersuchung **N**ord-west **A**rgentinien) seismograph network was in operation for approximately 100 days between late August and late November 1997. Most stations were equipped with short-period 1-Hz *Mark* L4-3D seismometer and *PDAS* data loggers recording continuously 100 samples per second (sps) (triangles in Figure 3.1). Coverage in the western part of the network was complemented by seven short-period vertical seismographs operated by University of Chile recording in a triggered mode 60 sps (inverted triangles in Figure 3.1) and five broadband instruments from a long-term deployment of the GeoForschungsZentrum Potsdam [*Bock et al.*, 1998] recording a continuous 20 sps data stream (squares in Figure 3.1). Stations were spread evenly across the plateau with an average spacing of about 40 km. Internal clocks were synchronized to universal standard time using GPS satellite signals. Multiple GPS and barometric altimeter measurements yielded site locations with an accuracy better than 50 m.

The continuous data streams were triggered in the lab with appropriate coincidence criteria detecting about 700 events within the network and its immediate vicinity. Seismic activity in the study area of the Andean backarc is more humble than in the forearc region that was the site of previous seismic field campaigns [*Comte et al.*, 1992; *Graeber & Asch*, 1999; *Haberland & Rietbrock*, 2000]. This might be in part due to very high attenuation beneath the Western Cordillera and the high plateau, suppressing many of the smaller events. In particular, events west of the magmatic arc could often not be observed at stations on the plateau.

P and *S* arrival times and first motion polarities were hand-picked [*Rietbrock & Scherbaum*, 1998] and used for preliminary location in a single-event location scheme [Hypo71, *Lee*

code	name	latitude [°]	longitude [°]	elevation [m]	data logger type	sensor type
ADG	Abro de Gallo	-24.3128	-66.4820	4528	PDAS	L4-3D
ARI	Salar de Arizaro	-24.7275	-67.4903	3575	PDAS	L4-3D
BUS	Burras	-23.3975	-66.1317	3575	PDAS	L4-3D
CAM	Campo Amarillo	-24.1376	-66.6995	4077	PDAS	L4-3D
CAU	Cauchari	-24.2268	-66.9587	3808	PDAS	L4-3D
COR	Coraya	-23.2082	-65.4095	3352	PDAS	L4-3D
EIN	Einstein	-22.9506	-67.6204	4000	PDAS	L4-3D
ELM	El Moreno	-23.9722	-65.8340	3723	PDAS	L4-3D
ESC	Esquina Colorado	-24.5700	-66.1893	3501	PDAS	L4-3D
FUN	Fundiciones	-22.5151	-66.1781	3884	PDAS	L4-3D
HUA	Huancar	-23.5916	-66.4364	3802	PDAS	L4-3D
IRY	Iruya	-22.8907	-65.2523	3930	PDAS	L4-3D
JER	Jeroglificos	-22.7430	-68.4308	3411	PDAS	L4-3D
JUY	Jujuy	-24.3139	-65.4214	1784	PDAS	L4-3D
LAC	Laguna Agua Calientes	-23.6180	-67.5454	4328	PDAS	L4-3D
LAQ	La Quiaca	-22.1540	-65.7293	3673	PDAS	L4-3D
LAS	Lascar	-23.3249	-67.7919	3845	PDAS	L4-3D
MIR	Miraflores	-23.0563	-65.8610	3529	PDAS	L4-3D
MLC	Mina La Casualidad	-25.0279	-68.2166	4095	PDAS	L4-3D
OLA	Olacapato	-23.6059	-66.7074	3958	PDAS	L4-3D
OR1	Oran	-23.1558	-64.3168	47	ORION	L4-3D
OR3	Rosario de la Frontera	-25.8380	-64.9312	841	ORION	L4-3D
OR4	Rivadavia	-24.1842	-62.8880	278	ORION	L4-3D
ORA	Oratorio	-22.1058	-66.0605	3868	PDAS	L4-3D
PDJ	Paso de Jama	-23.2960	-67.0069	4131	PDAS	L4-3D
PDM	Puesta del Marques	-22.5474	-65.6169	3642	PDAS	L4-3D
PGR	Pastos Grandes	-24.4281	-66.6669	4108	PDAS	L4-3D
PIR	Mina Pirquitas	-22.7568	-66.4677	4148	PDAS	L4-3D
PUR	Purmamarca	-23.6982	-65.5794	2905	PDAS	L4-3D
QUI	Quichagua	-22.9239	-66.3250	4204	PDAS	L4-3D
RAC	Rachayte	-22.8208	-66.0282	3597	PDAS	L4-3D
RSA	Rio San Antonio	-23.9998	-66.1773	3645	PDAS	L4-3D
SAC	San Antonio de los Cobres	-24.2745	-66.3178	3968	PDAS	L4-3D
SAL	Salta	-24.7027	-65.4190	1430	PDAS	L4-3D
SAT	Salar de Talar	-23.9153	-67.6939	3975	PDAS	L4-3D
SDC	Salar de Cauchari	-23.8970	-66.7992	3930	PDAS	L4-3D
SEY	Sey	-23.9707	-66.4889	4052	PDAS	L4-3D
SGR	Salinas Grande	-23.4043	-65.7734	3522	PDAS	L4-3D
SHM	Salar de Hombre Muerto	-25.1698	-67.0688	4059	PDAS	L4-3D
SIC	Paso de Sico	-23.8784	-67.1625	3833	PDAS	L4-3D
SOC	Socompa	-24.7378	-68.0790	4285	PDAS	L4-3D
SON	Soncuyo	-23.1196	-66.0219	3554	PDAS	L4-3D
SPQ	Salar de Pocitos o Quirón	-24.7669	-66.9447	3770	PDAS	L4-3D
SRO	Santa Rosa	-24.4585	-65.9417	3122	PDAS	L4-3D
TAC	Taca Taca	-24.4646	-67.7070	3563	PDAS	L4-3D
TAN	Tanques	-23.1268	-66.5190	4144	PDAS	L4-3D
TOG	Tolar Grande	-24.4037	-67.3312	3579	PDAS	L4-3D
TUG	Cerro Tuzgle	-24.0578	-66.5003	4720	PDAS	L4-3D
WSA	West Salar	-23.3701	-68.6390	2682	PDAS	L4-3D
PAR	Paranal	-24.6404	-70.3893	2358	REFTEK	STS2
COL	Colorado	-24.2380	-68.8628	3157	REFTEK	STS2
SOE	Socaire	-23.6097	-67.8822	3313	REFTEK	STS2
CON	Conchis	-21.9582	-68.7217	3441	REFTEK	STS2
MIC	Michilla	-22.6093	-70.1650	974	REFTEK	STS2
GOR	Sierra Gorda	-22.9391	-69.1959	1980	EDAS	L4C-1D
JAR	Sierra del Jardin	-23.5819	-69.2847	1970	EDAS	L4C-1D
SMA	Sierra Mariposa	-23.6656	-68.7491	2717	EDAS	L4C-1D
LIT	Litio	-23.6410	-68.3461	2429	EDAS	L4C-1D
TIL	Tilomonte	-23.7940	-68.1018	2505	EDAS	L4C-1D
CHA	Laguna Chaxa	-23.2880	-68.0930	2435	EDAS	L4C-1D
GUA	Guatin	-22.7558	-68.0710	3259	EDAS	L4C-1D

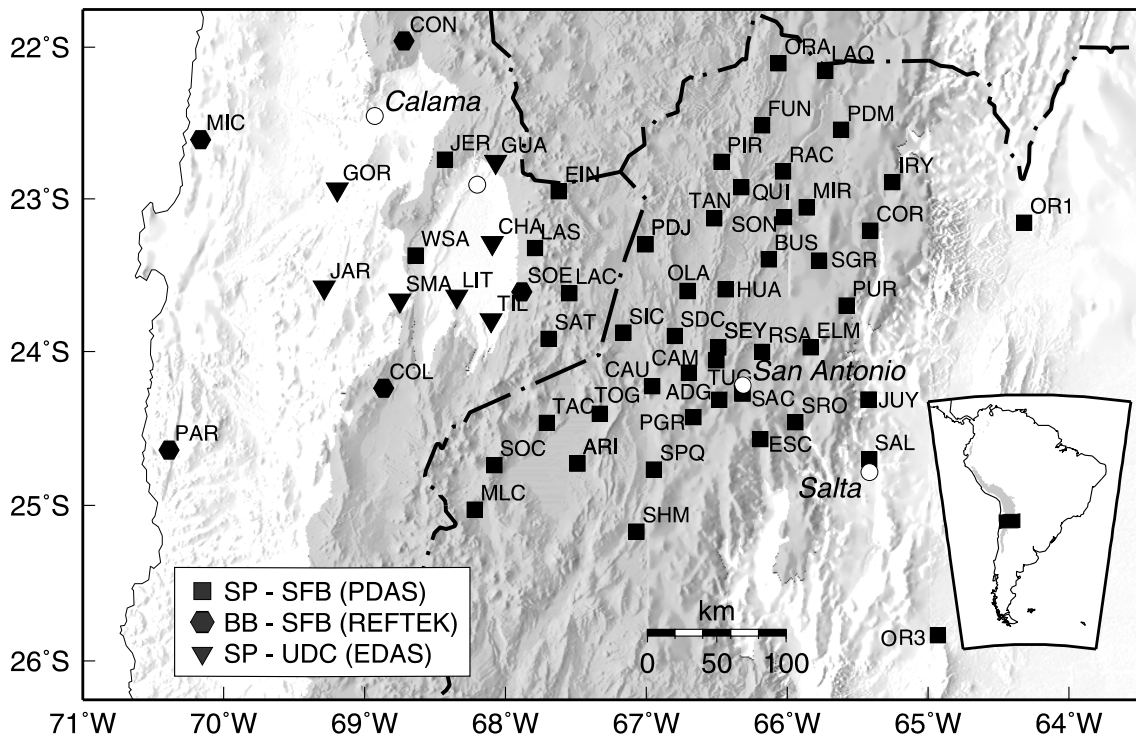**Table 3.1:** Station list of the PUNA experiment.

Figure 3.1: Site map of the PUNA'97 seismograph network. The area 3000 m above sea-level is shaded, approximately indicating the extent of the Puna-Altiplano plateau. Symbols are keyed by sensor type: squares – short-period 3-component , hexagon – broad band, inverted triangles – short-period vertical. The field headquarters were located in San Antonio de los Cobres in the Puna. Station coordinates are listed in Table 3.1.

& Lahr, 1975]. These data underwent further selection by discarding events with an azimuthal gap greater than 270°, and demanding for the intermediate depth events at least 15 readings (among those at least four *S* readings), whereas shallow events, owing to their lower abundance and smaller magnitudes, were also kept with a smaller number of picks. This reduced the data set to 483 events. Among these, 57 were shallow focus crustal events, the rest originated in the Benioff zone of the subducted Nazca plate. Accuracy of *P* times is estimated to be on average about 0.04 seconds. Determination of *S* arrivals was difficult because of the afore mentioned high attenuation which almost entirely blocked *S* energy at many sites. Because good *S*-times are crucial for precise depth assignment, picks were made on rotated and integrated records to avoid misinterpretation of compressional wave precursors and to enhance the damped, very low frequency *S* signal. This way about half the number of *P*-picks could be obtained for *S*, yet with significantly lower accuracy (≈0.5 sec).

3.2   1-D   Velocities,   Hypocenter,   and   Focal Mechanisms

Velocity information for the Puna region is very sparse. The only refraction experiment penetrated merely the upper crust [*Wigger et al.*, 1994] and a standard velocity model for the mantle (IASPEI91, *Kennett* [1991]) proved inadequate, producing large RMS residuals when locating the intermediate depth events. For that reason the arrival time data set was used for a joint inversion of 1-D velocity structure, station delays and hypocentral coordinates [*Crosson*, 1976; *Kissling et al.*, 1994]. In this inversion scheme the structure is parameterized by a stack of flat layers over a half space. Within each layer the velocity is assumed to be constant. The inverted velocity model will represent, ideally, the average (weighted by the total ray length) of the true 3-D velocities over the depth range of each layer. Such inversions have been applied in many areas with different degrees of complexity providing very good hypocentral estimates [e.g., *Kissling*, 1988; *Kissling & Lahr*, 1991; *Maurer & Kradolfer*, 1996]. Specifically, in the forearc and arc region of this subduction zone, hypocenter from a 1-D model differed only marginally from hypocenter of subsequently performed 3-D tomographic inversions [*Graeber & Asch*, 1999; *Comte et al.*, 1999]. This is because, if the hypocenter are well constrained, the unresolved part of the model is absorbed by the station delays and travel time residuals, rather than shifts in the hypocentral coordinates.

Both P and S velocities have been inverted using the code VELEST [*Kissling et al.*, 1994]. The crustal events were not used in the inversion. Because of their very shallow depth, rays would sample only the uppermost, likely very heterogeneous part of the model. A Wadati-diagram delivered a starting value for v_p/v_s of 1.75. A suite of starting models with 20 km layer thickness has been used to carefully sample the model space (dashed lines in Figure 3.2). The range of resulting velocity functions that fit the data equally well is shown as shaded band in Figure 3.2.   Most part of the velocity model is well constrained. Only the upper 60 km (crust) show large variations. There, all rays screen the model at similar steep angles, causing a strong trade-off between velocities and station delays. The model is also robust towards different data selection criteria, i.e. using only events with a maximum azimuthal gap of 230° respectively 180° did affect the outcome only minorly. To better represent the overall seismicity, the less stringent 270° maximum gap was used. For the final model (black line in Figure 3.2, Table 3.2), layers that were not well resolved (upper and lower most parts), or had similar velocities, were bundled together. The final model started from IASPEI91 [*Kennett*, 1991] mantle velocities and a 60 km thick crust with 6.0 km/s.

Hypocenter projections from this inversion are shown in Figure 3.3 as circles. Although
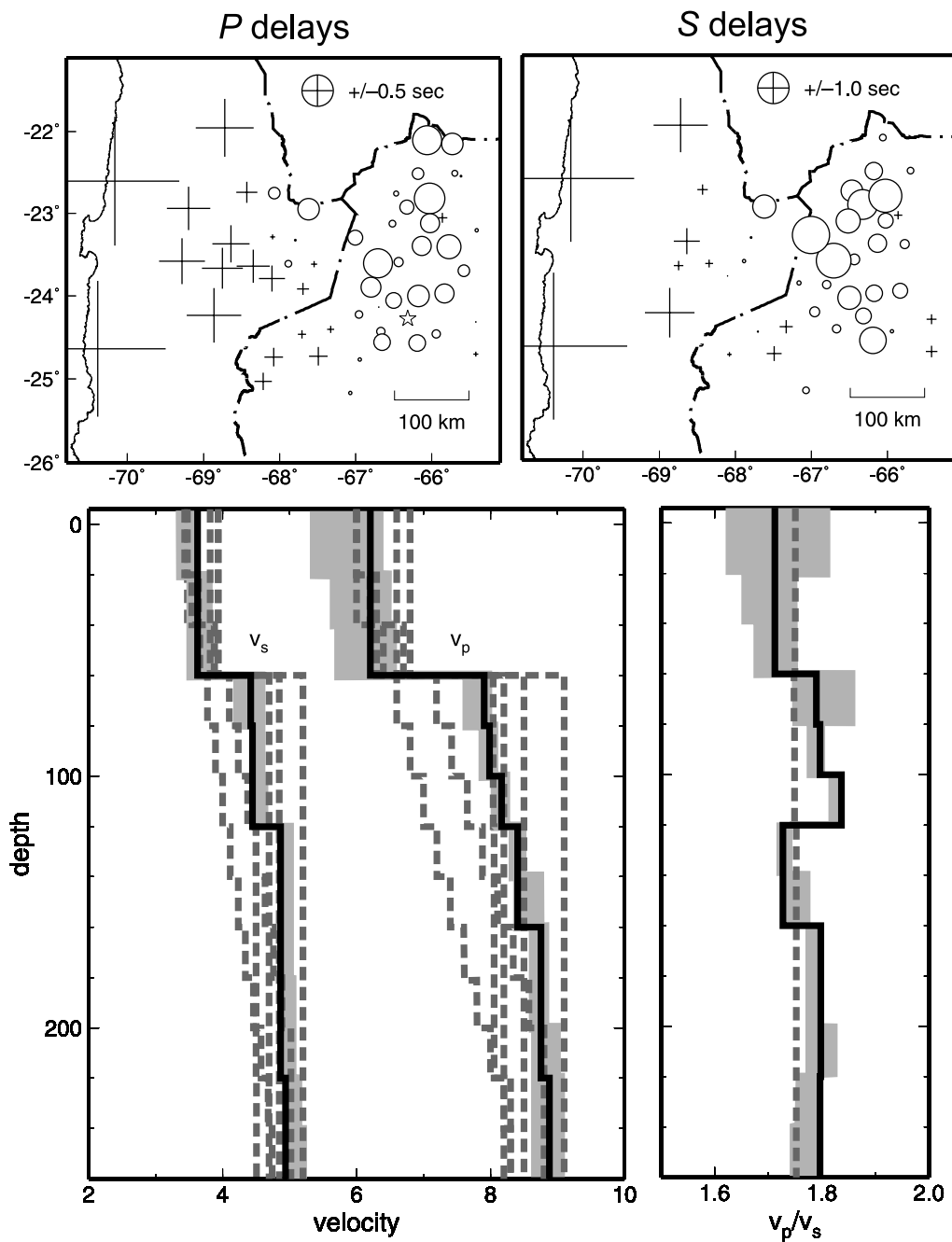
Figure 3.2: Velocity-depth function from a joint inversion for 1-D velocity structure, station delays, and hypocentral parameters (black line). The shaded area indicates the range of models that fit the data equally well. This range comes from inversion-runs with a suite of different starting models shown as broken lines. Above, P and S station delays are shown. Crosses indicate negative delays, circles positive ones. For the station marked with the star, the P-delay was constrained to zero. Values for station delays are listed in Appendix Table A.

depth [km]	v_p [km/sec]	v_s [km/sec]	v_p/v_s
0	6.21	3.62	1.71
60	7.91	4.42	1.79
80	7.99	4.45	1.80
100	8.17	4.45	1.84
120	8.41	4.87	1.73
160	8.75	4.87	1.80
220	8.85	4.82	1.83

Table 3.2: Minimum 1-D velocity model. Depth is depth to top of layer.

such joint inversions produce improved relative locations, the absolute positions can be biased. We compared the locally obtained hypocenter with a newly relocated tele-seismic data set from *Engdahl et al.* [1998] in depth cross sections and found excellent agreement in position and slope of the Benioff zone.

For 70 events in the center of the array, fault plane solutions were determined from first motion polarities using the computer program FPFIT [*Reasenberg & Oppenheimer*, 1985]. For our network aperture the deep seismicity provided only a limited cone of take-off angles, often constraining only one (the steeply dipping) of the two nodal planes well. Upper hemispheric projections of the nodal planes are shown in Figure 3.4.

The shallow crustal seismicity was located separately from the Benioff events. We also applied a joint inversion for hypocentral parameters and station delays, but did not invert for velocities. Epicenters and hypocenter projections on cross sections are displayed as crosses in Figure 3.3, and in more detail in Figure 3.5. The coarse-meshed network allowed only limited depth control for the shallow earthquakes.

Because of the small magnitudes and large station spacing, focal mechanisms could not be constrained from first motion polarities. Instead, a waveform inversion scheme was applied [*Schurr & Nàbělek*, 1999]. Here direct *P* and *S* pulses are modeled in a similar manner as it is routinely done for tele-seismic events. *Schurr & Nàbělek* [1999] showed that this technique can determine source parameters even with sparse station coverage. Nevertheless, because of the small magnitudes of the events and complex waveforms due to sub-horizontal ray paths through unknown structure, only two events could be modeled. The fault plane solutions, as well as an example of waveform fit are shown in Figure 3.5.
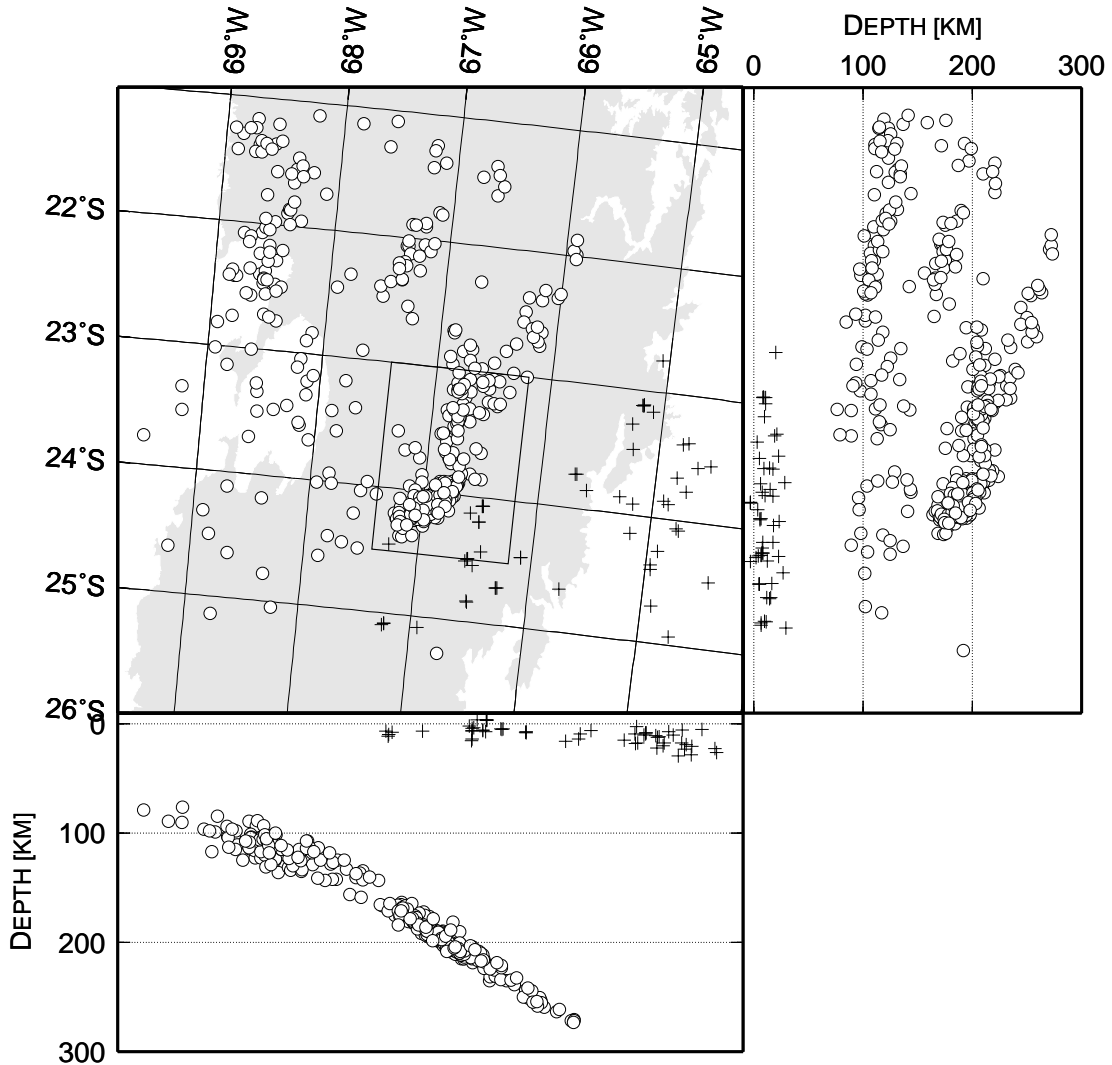
Figure 3.3: Epicenter map and vertical hypocenter projections of earthquakes located with the PUNA array. Benioff earthquakes are displayed as circles, crustal events are plotted as crosses. The Puna plateau is shaded in grey. The cross section is rotated 5° north from an east-west line in order to obtain best focusing of the Benioff zone. The rectangle denotes the outline of the map in Figure 3.4.

3.3 Results and Discussion

3.3.1 Velocities and Station Delays

Starting with a homogeneous gradient the inversion places the crust mantle boundary at 60 km depth. To test the sensitivity of our data to crustal thickness we also tried to fit other Moho depths. Whereas a 70 km thick crust increases data variance by seven percent, thinner crust is compensated by slower average crustal velocity without loss of
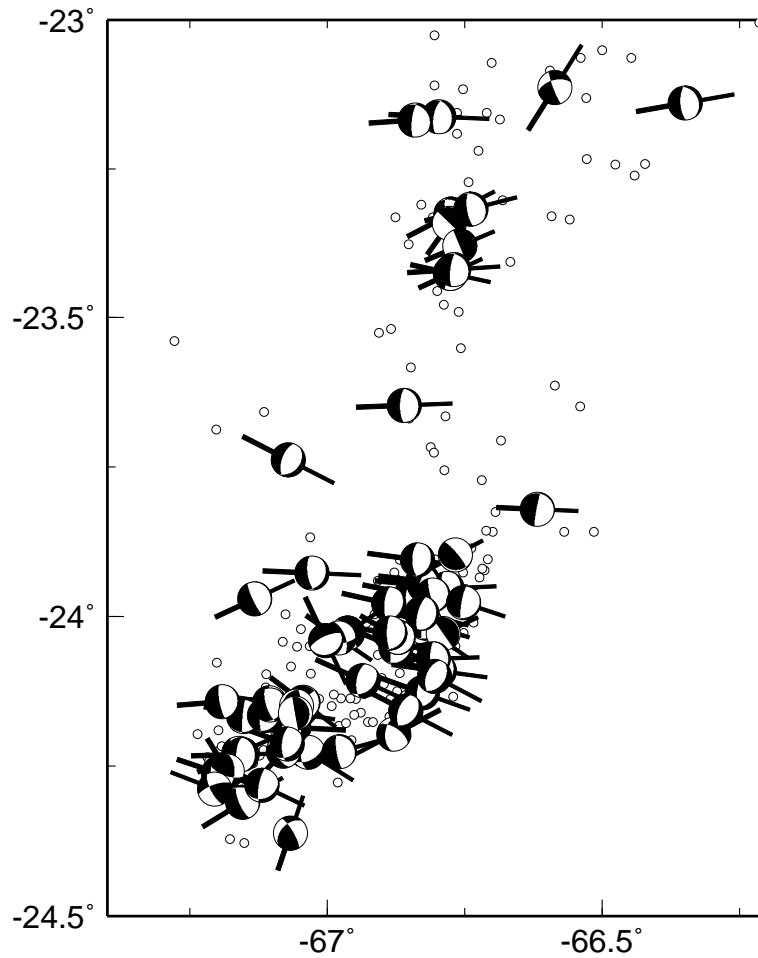
Figure 3.4: Upper hemispheric projections of fault plane solutions from 70 intermediate depth ($\approx$200 km) earthquakes beneath the Puna plateau (hypocentral parameters are listed in Table B in the Appendix). Black bars are tension axes projected onto the surface. Note that tension axes are oriented approximately perpendicular to the strike of the lineament defined by seismicity.

data fit (6.0 km/sec for 50 km, 5.7 km/sec for 40 km crustal thickness). To locate the shallow crustal earthquakes velocities of 5.8 km/sec or higher are needed in the upper 20 km, placing a lower bound on crustal thickness to 50 km. 50-60 km crustal thickness is in accordance with results from *Whitman* [1994] for the eastern margin of the plateau and also with Moho depths derived from a recent receiver function study [*Yuan et al.*, 2000].

Average velocity and v_p/v_s ratio in the crust are low, indicative of felsic material [*Rudnick & Fountain*, 1995; *Zandt et al.*, 1996]. Similar values have been found in the Altiplano, and were there interpreted as supportive of crustal shortening as cause of plateau uplift [*Zandt et al.*, 1996].

Mantle velocities increase gradually from 8 km/s to 8.7 km/sec at 200 km depth. These

velocities are too fast for normal mantle material. We believe that the high velocities at depth are the effect of the subducted slab. This has been corroborated with synthetic travel times from a two-dimensional slab model, showing that inverted 1-D velocities become increasingly influenced by the fast slab at depth. Although there is an increased v_p/v_s ratio in the uppermost mantle, the data do not require a low P-velocity zone at that depth range.

Station corrections show a systematic pattern from negative delays in the west to positive delays on the plateau and Eastern Cordillera, indicative of velocity decrease from west to east. The negative station corrections in the forearc agree with relative fast crustal velocities found there in refraction experiments [*Wigger et al.*, 1994; *Patzwahl et al.*, 1999; *Graeber & Asch*, 1999] but may also be caused by the slab. We interpret the positive delays at the eastern stations as indicative of lower average velocities in the mantle, because for these stations the effect of the slab becomes less influential.

3.3.2 Benioff Seismicity

Figure 3.3 shows epicenters and hypocenter-projections of the located seismicity. The cross section perpendicular to the strike of the subduction zone is rotated 5° N from the east-west direction. Here, the Benioff zone sharply defines a 35° dipping plane, tapering off to only 10 – 15 km thickness at 200 km depth. The dip appears constant from north to south. Seismicity is clustered between 100 and 120 km and between 180 km and 220 km depth. Three fingers of increased seismic rate striking north to northeast are perceptible on the map view. This is not an artefact caused by limited recording time, as seismicity plotted from several decades shows a similar pattern [e.g., *Barazangi & Isacks*, 1976; *Kirby et al.*, 1996; *Engdahl et al.*, 1998]. Seismic activity is lowest between 23°S and 25°S in the 100 km depth range.

The most prominent cluster is located in the center of the array in the depth range between 180 km and 220 km. Looking on top of the slab, this cluster has a elongated shape with several bends. It also marks a sharp boundary to the *Copiapo* seismic gap to the south. Focal mechanisms and tension axes for earthquakes from this cluster are shown in Figure 3.4. Most events have extensional mechanisms with their strikes approximately following the lineament.

The uneven distribution of seismicity in the subducted slab can either be caused by heterogeneities in stress or in state (i.e. strength, temperature). *Kirby et al.* [1996] speculate that these north to north-east trending clusters could be the seismic expression of subducted volcanic chains and ridges. Their increased crustal thickness would delay eclogite formation and dehydration, and thus also seismicity, to greater depth. Because

such structures get intensely faulted and broken as they enter subduction [e.g., *von Huene & Scholl*, 1991], they would also focus deformation as natural zones of weakness, just as fault zones do in the crust. The rotation of tension axes away from pure E-W extension, perpendicular to the trend of the lineament, supports this notion. Earthquakes could occur on roughly aligned, strongly hydrated faults and cracks.

3.3.3   Crustal Seismicity in the South American Plate

Only very little is known about present day deformation in the Puna plateau. A change in the stress regime from WNW-ESE compression and vertical extension to east-west compression and horizontal north-south extension approximately 2 m.y. ago was deduced from fault-slip measurements for the southern Puna [*Allmendinger et al.*, 1989; *Marrett et al.*, 1994]. Presently, east-west compression is expressed in the seismically active fold and thrust belt of the foreland and to some extent the Eastern Cordillera which forms the eastern flank of the plateau. For the plateau itself deformation appears to be concentrated at its northern and southern edges. Some normal faulting with north-south extension was found in the northern Altiplano [*Grange et al.*, 1984; *Sebrier et al.*, 1985], whereas strike-slip faulting seems to dominate in the southern Puna [*Allmendinger et al.*, 1989; *Marrett et al.*, 1994]. Very few shallow earthquakes in the Puna-Altiplano high plateau are reported from global networks. For the Puna only one single event strong enough to teleseismically constrain a focal mechanism has been recorded [*Chinn & Isacks*, 1983]. The event occurred just south of the study area, near the Salar de Antofalla, and had a oblique thrust mechanism.

The earthquakes located with our local network concentrate in the foreland, along the eastern edge of the Andes, and around the El Toro-Olacapato-Calama Lineament (TOCL) in the Puna. The easternmost events (Figure 3.3) belong to the Santa Barbara Ranges, a thick skinned N-S thrust belt with deep reaching, compressional seismicity. Event depths up to 30 km have been obtained from a local seismic experiment [*Cahill et al.*, 1992] and are confirmed by our data (vertical cross section in Figure 3.3). These events also had the largest magnitude (up to $M_l \approx 3$) from all recorded shallow seismicity. A second band of earthquakes spreads along the eastern slope of the Eastern Cordillera. This region also exhibits Quaternary N-S thrust faulting and known historic seismicity.

The TOCL has been recognized as a major shear zone probably crossing the entire Andes from the foreland in the southeast to the Chilean forearc in the northwest. Up to 20 km left-lateral displacement has been postulated along the lineament [*Allmendinger et al.*, 1983]. Several small centers of young mantle-derived backarc volcanism also occur along the TOCL. It has been suggested that the deep reaching fault serves as a conduit for the
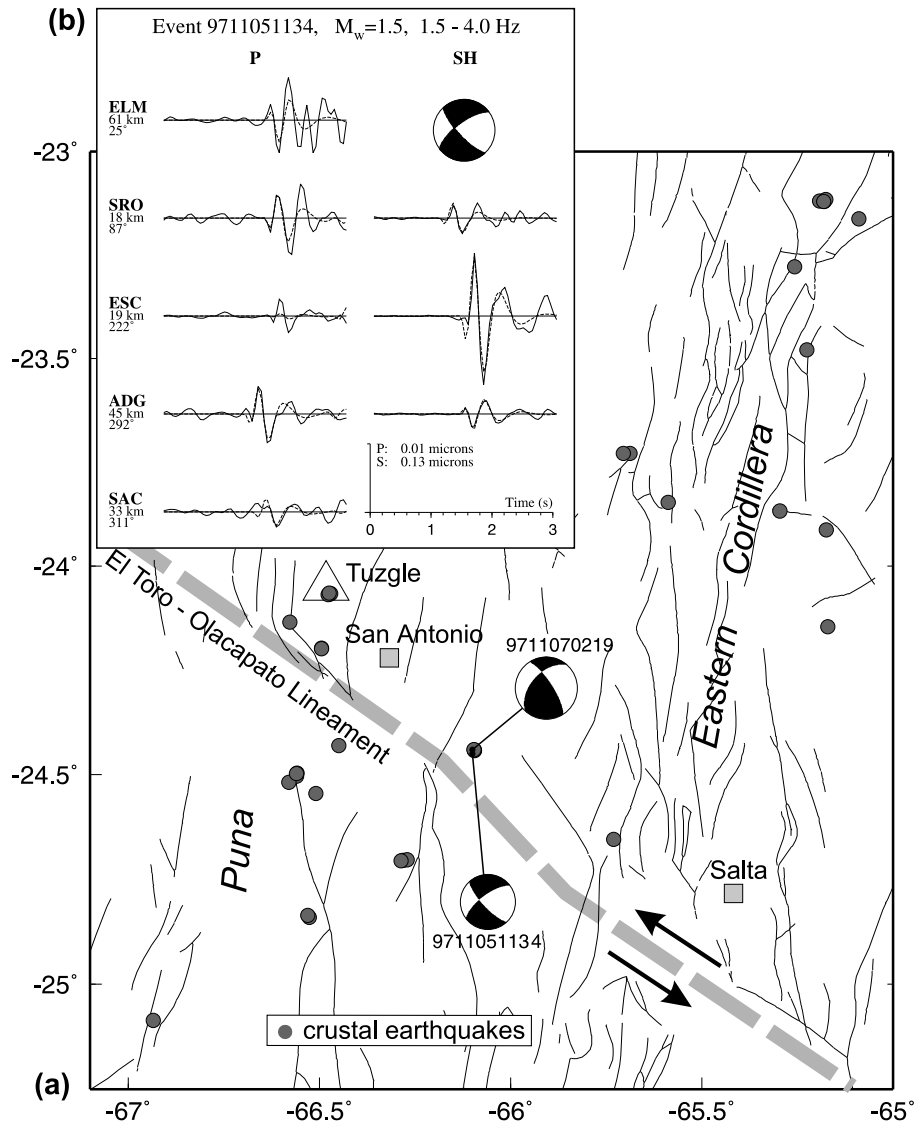
Figure 3.5: (a) Detailed map of crustal earthquakes. Black lines are mapped faults. Thick grey line indicates the approximate course of the TOCL. Lower hemispheric projections of the double-couple estimate from waveform inversion (focal parameters of the two events are listed in the Appendix Table B). **(b)** Example of waveform fit for a small crustal event. Solid lines are observed seismograms, broken lines best-fit synthetics.

dense shoshonitic lavas [*Schreiber & Schwab*, 1991; *Marrett & Emerman*, 1992]. Several of the recorded micro-earthquakes align along this structure (Figure 3.5). For two events we were able to determine the focal mechanism from waveform inversion. Their strikes and sense of slip agree well with presumed direction and kinematic of the TOCL, suggesting ongoing deformation along this shear zone (Figure 3.5).

A series of events, all occurring within several hours, was recorded at Cerro Tuzgle (Fig-

ure 3.5). This is a complex Quaternary strato-volcano approximately 200 km east of the modern magmatic arc [*Coira & Kay*, 1993]. All events are very shallow and have coherent waveforms indicative of similar mechanism and location. Whether this is a sign of magmatic or tectonic activity eludes us.

All other microseismicity in the Puna locates south of the TOCL. Although there are many mapped faults it is difficult to tie the earthquakes to any particular structure.

The fact that all historic seismicity and microseismicity in the Puna plateau is located at the TOCL and south of it suggests that the TOCL marks a structural boundary in the plateau. This is supported by the fact that young mafic backarc volcanism is also concentrated in the southern Puna and reaches north only up to the TOCL [*Allmendinger et al.*, 1997]. Because these dense lavas can rise through the thick crust only along deep reaching fault zones, the lack of mafic volcanism in the northern Puna could indicate absence of such zones of weakness. We believe that the Puna north of the TOCL behaves like a stable block with no internal deformation, whereas to the south, the plateau is weaker and internally deforming. The depths for events occurring inside the plateau crust are very shallow ($\leq$10 km), indicating a hot geotherm and a shallow brittle-ductile transition.

Chapter 4

Tomography

4.1 Introduction

In seismic tomography [*Aki et al.*, 1977] travel time (amplitude) anomalies of seismic waves recorded at seismograph arrays are back-projected into a three-dimensional model of seismic velocity (attenuation) by inversion of a system of equations linking the measurements to the wanted physical parameter. The method is widely used in scales ranging from millimeters (material science and medicine) to global studies of the entire earth.

In this thesis earthquakes inside the subducting Nazca plate beneath the Central Andes are used as sources for tomographic inversion. At 23°S, subducted oceanic lithosphere dips eastward at an angle of approximately 30° into South American mantle, intermittently releasing seismic energy at a high rate to a depth of 300 km. Landward the seismic slab extends beneath the Eastern Cordillera, illuminating the entire mountain range at lithospheric scale with high resolution. This region of crust and uppermost mantle is otherwise only with difficulty accessible geophysically. Seismic studies using active sources do normally not penetrate beneath the lower crust. Tele-seismic rays, owing to their steep incidence, do not provide good vertical resolution at that depth range, and the long wavelengths of surface waves are only sensitive to large-scale structures. The Benioff-zone-events emanate rays from different depth levels that sample the lithosphere at a variety of angles from sub-horizontal to near-vertical, making them particularly suitable for tomography.

Several large seismic experiments, aiming to image different parts of the Central Andean subduction zone, were conducted in recent years [*Dorbath et al.*, 1993; *Comte et al.*, 1992; *Myers et al.*, 1998, e.g.,]. The SFB 267 "Deformation Processes in the Andes", carried out four passive seismic experiments between 1994 and 1997, deploying portable, mostly

39

short-period, seismograph arrays between 20°S and 25°S from the Pacific coast across the Andean mountain range (Chapter 3). In this thesis data from the three experiments PISCO'94 , ANCORP'96, and PUNA'97 are combined, and inverted together for a 3-dimensional model of *P*-wave velocity, v_p/v_s ratio, and *P*-wave attenuation. The PISCO and ANCORP data have been analyzed previously. *Graeber & Asch* [1999] presented a 3-D v_p and v_p/v_s model for the forearc and western arc from PISCO travel time data. This was extended to the north with ANCORP data by *Rietbrock & Haberland* [1998]. PISCO and ANCORP *P*-wave spectra were used for a 3-D attenuation model by *Haberland & Rietbrock* [2000]. Now all these data are combined and supplemented by data from the PUNA network, to derive a consistent model of the entire subduction zone for v_p, v_p/v_s, and Q_p. The PUNA network extended coverage of the PISCO and ANCORP experiments to the east, across the recent magmatic arc and into the backarc plateau of the Argentine Puna, completing an important part in the deep Andean structural puzzle. In addition to the new terrain of the backarc region, it also opened up the important eastern edge of the PISCO network, the Western Cordillera, by its overlapping set-up. This region could only partly being resolved before [*Graeber & Asch*, 1999; *Haberland & Rietbrock*, 2000]. Although our new model comprises the entire subduction zone, discussion of results will mostly be restricted to those parts that are new or become significantly better resolved now (mainly the Western Cordillera and the Argentine backarc region), or are important in the overall interpretation. For details on results in the regions covered by the PISCO and ANCORP arrays refer to *Graeber* [1997]; *Graeber & Asch* [1999]; *Haberland* [1999]; *Haberland & Rietbrock* [2000]; *Rietbrock & Haberland* [1998].

4.2   Basic Theory and Methods

Here a short overview about the basic theory underlying local earthquake tomography, as well as its specific realization in the used computer code is given. For a thorough treatment the reader is referred to *Thurber* [1993] and references therein.

4.2.1   The Coupled Hypocenter Velocity Problem

In travel time tomography earthquake arrival times T are measured from seismograms. The absolute time T_{ij} is the ith earthquake's origin time τ_i plus the travel time t_{ij} recorded at the jth station:

$$T_{ij} = \tau_i + t_{ij}. \tag{4.1}$$

Both the travel time and the origin time are unknown. The travel time t can be expressed as a path integral along the seismic ray s through the slowness (reciprocal velocity) field

u:

$$t_{ij} = \int\limits_{path} u \, ds. \tag{4.2}$$

If we assume an initial model of slowness and preliminary estimates of hypocenter locations and origin times, e.g. from single-event-locations, theoretical arrival times T^{calc} can be calculated and compared to the observed ones:

$$r_{ij} = T_{ij} - T_{ij}^{calc}. \tag{4.3}$$

The residuals r_{ij} can then be related to perturbations of source and velocity parameters by a linear approximation (Taylor expansion around the initial hypocenters $\boldsymbol{x_i^0}$, origin times τ_i^0, and initial model m^0)

$$r_{ij} = \Delta\tau_i + \sum_{k=1}^{3} \frac{\partial t_{ij}}{\partial x_{ik}} \Delta x_{ik} + \sum_{l=1}^{L} \frac{\partial t_{ij}}{\partial u_l} \Delta u_l, \tag{4.4}$$

$$\Delta\tau_i = \tau_i - \tau_i^0, \ \ \Delta\mathbf{x_i} = \mathbf{x_i} - \mathbf{x_i^0}, \ \ \Delta u_l = u_l - u_l^0,$$

where the last term implies a discretization of the velocity model with the finite number of parameters L. $\partial t_{ij}/\partial u_l$ represent the relative influence of the lth model parameter on a travel time datum. Because in equation (4.4) a highly non-linear problem has been linearized, a solution is usually derived in an iterative procedure. All of these equations hold both for P and S waves.

4.2.2 v_p/v_s Tomography

v_p/v_s, or Poisson ratio is an important parameter to characterize rocks. It is sensitive to lithology and state (e.g. temperature, porosity, hydration) of subsurface rocks, and together with the P velocity greatly helps interpretation of tomographic images. There are good reasons to directly invert for v_p/v_s, instead of calculating its spatial distribution from independently derived P and S models. S arrival times are generally subject to much greater uncertainty than P picks. This is due to their arrival in the P coda, mode conversions, anisotropy, attenuation, and their inherently lower dominant frequency. This generally reduces the number of data, and together with the greater uncertainty, diminishes resolution of S models, hence hindering direct comparison with P wave models.

v_p/v_s is generally better known and varies less than v_s. Consequently, starting from a well constrained 3-dimensional v_p model with a constant v_p/v_s ratio, e.g. from a Wadati diagram, describes the S-velocity field better than a 1-dimensional v_s model from an inversion. Thus inverting for v_p/v_s based on a 3-dimensional v_p model yields an overall more consistent and better constrained model for S-velocity.

Derivation of v_p/v_s from $S - P$ times as data is equivalent to the above treatment for P (or S) times, except for the forward problem stated in (4.2), which is now expressed as

$$t_{ij}^{S-P} = \int\limits_{path} \left[\frac{1}{v_s} - \frac{1}{v_p} \right] ds = \int\limits_{path} \left[\frac{v_p}{v_s} - 1 \right] \frac{1}{v_p} \, ds. \qquad (4.5)$$

$S - P$ time residuals can be calculated based on the P wave velocities and an initial v_p/v_s model. They can be related to v_p/v_s model perturbations just as before.

4.2.3   Attenuation Tomography

Seismic attenuation modifies the spectrum of body-waves emitted at the source. Consequently Fourier amplitude spectra of body-wave arrivals are used as basic data in most local or regional attenuation studies. In general, the spectrum of a body-wave from the ith earthquake recorded at the jth station can be assembled from the following parts:

$$A_{ij}(f) = S_i(f)I_j(f)G(s) \exp(-\pi f \frac{t_{ij}}{Q_{ij}}), \qquad (4.6)$$

where $S(f)$ is the original source spectrum, $I(f)$ the recording instrument's response, $G(s)$ the amplitude loss due to geometrical spreading, and the exponential term at the end describes the influence of attenuation. Q is the *quality factor* and describes the fractional energy loss per cycle:

$$Q = -2\pi E/\Delta E. \qquad (4.7)$$

The whole path attenuation operator $t_{ij}Q_{ij}^{-1} = t_{ij}^*$ can be expressed as a path integral through field of $(Q(s)v(s))^{-1}$:

$$t_{ij}^* = \int\limits_{path} \frac{ds}{Q(s)v(s)}, \qquad (4.8)$$

where $v(s)$ is the velocity along the ray path. The path integral (4.8) closely resembles equation (4.2), the basic equation for travel time tomography. In fact, with a known velocity field v, i.e. from velocity tomography, the problem can be treated equivalently to travel-time tomography with known hypocenters and origin-times.

Determination of t^*

Whereas picking travel-times is quite trivial, determination of whole path attenuation (t^*) is a challenging task in its own right. Based on equation (4.6) there are different ways to isolate t^* from the spectrum, with the spectral ratio technique and spectral inversion the most widely used. Here a spectral inversion method [*Rietbrock*, 1996, 2000] is applied.

To calculate spectra $A_{ij}(f)$ we have to express the individual terms in (4.6). Because we model the observed spectra in the pass band of the recording system (1 Hz - 30 Hz), $I_j(f)$ can be set one, and $G(s)$ is simply $1/s$ for body waves. Remains the source spectrum, which, following *Scherbaum* [1990], we assume to obey

$$S_i(f) = \Omega_0 \frac{f_c^\gamma}{f_c^\gamma + f^\gamma}, \tag{4.9}$$

where Ω_0 is the low frequency spectral plateau that contains all frequency independent parts, f_c the corner frequency, and γ determines the high frequency spectral decay.

With $\gamma = 2$ for the so-called ω^2-source model [*Brune*, 1970, 1971], the observed spectrum $A(f)$ in (4.6) can be modeled as

$$A_{ij}(f) = \frac{\Omega_0' \exp(-\pi f t_{ij}^*)}{1 + \frac{f^2}{f_c^2}}. \tag{4.10}$$

Here Ω_0' additionally contains $G(s)$, the geometrical spreading factor. Ω_0' is also often termed the signal moment. Relation (4.10) has the three unknowns Ω_0', f_c, and t^*, which contribute to the spectrum in a highly non-linear fashion. Making things worse, the
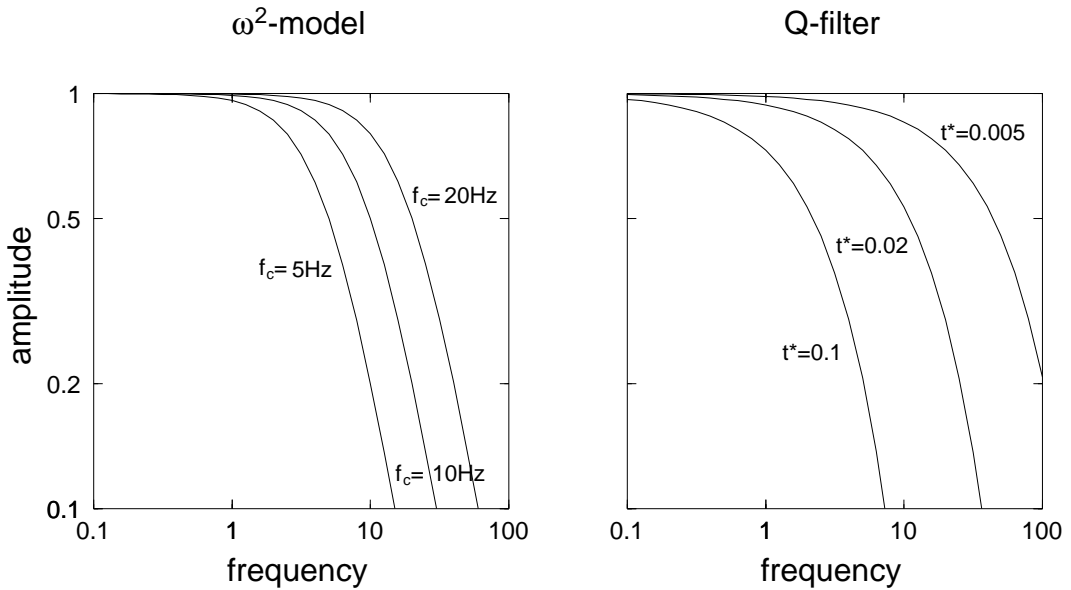

Figure 4.1: a) ω^2-source spectra of equation (4.9) [*Brune*, 1970, 1971] for different corner frequencies $f_c = 5$, 10, and 20 Hz. b) The absorption term or Q-filter (exponential term in equation (4.10)) operating on the source spectrum for $t^* = 0.1$, 0.02, and 0.005 s (f_c=10 Hz). For a travel time of 10 s this corresponds to Q values of 2000, 500, and 100.

'*Q-filter*' has a similar shape as the source-spectrum, rendering separation of the effects more difficult (Figure 4.1). In the method used here [*Rietbrock*, 2000], a linear inversion
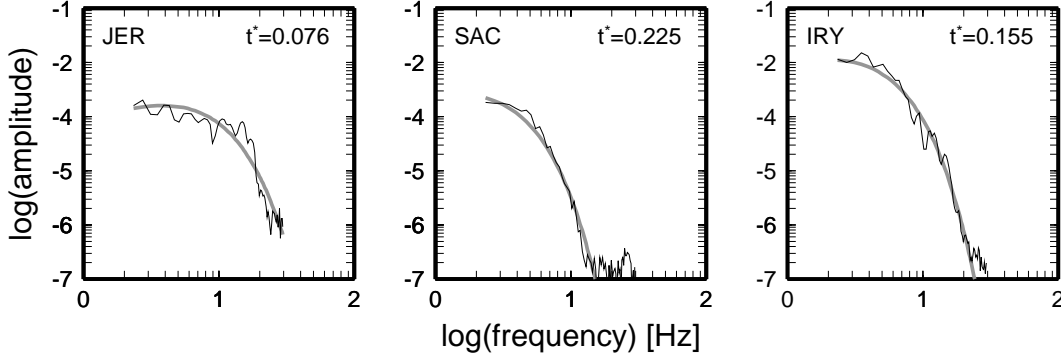
Figure 4.2: Observed (black) and best-fit synthetic (grey) spectra for three stations of the Puna network. The station JER is in the forearc and shows a different high frequency fall-off and a significant smaller t^* operator.

for Ω_0', combined with a grid search technique for the source corner frequency and the t^*-operator is applied. A single corner frequency f_c is sought for each source. This implies that directivity effects due to a finite rupture are negligible, which appears reasonable for the small magnitude events ($M_L \approx 1.0 - 4.5$) investigated. Ω_0''s are inverted for each event-station pair to account for the azimuthally varying radiation pattern of the source, geometrical spreading, site amplification, and velocity or density variations along the path. To obtain smooth observed spectra, they are computed with a multi-taper technique [*Park et al.*, 1987] with a frequency resolution of 4 Hz. Three examples of observed spectra with their modeled counterparts are shown in Figure 4.2.

The validity of the ω^2-source model has been checked by *Haberland* [1999] for the PISCO and ANCORP data. Comparing spectral inversion results to a spectral ratio technique, which makes no assumptions about the source model, no significant deviations beyond statistical errors could be established.

In addition to the assumption of the source model, frequency independent Q is implied in the inversion of equation (4.10). Laboratory measurements found frequency dependence of $Q \propto f^\alpha$ with $\alpha \approx 0.25$ [*Berckhemer et al.*, 1982]. *Sarker & Abers* [1998] obtained from seismological data of the Caucasus values for α ranging from 0.3 to 0.5. In contrast, *Rietbrock* [2000] could fit seismological data from Japan best with a frequency independent Q. Frequency dependence of Q may be an additional uncertainty in determining t^* from equation (4.10), but its investigation lies beyond the scope of this study.

4.2.4 The Inverse Problem

We can write relation (4.4) more conveniently in algebraic notation, bundling all residuals to the data vector $\mathbf{d}$, all Δx, $\Delta \tau$, Δu to the model correction vector $\mathbf{m}$, and the partial derivatives to the Jacobian matrix $\mathbf{G}$:

$$\mathbf{d} = \mathbf{G}\mathbf{m}. \tag{4.11}$$

A direct solution of equation (4.11) exists only if $\mathbf{G}$ is square, that is there are precisely as many observations as unknowns. This is rarely the case. Instead we formulate the solution of (4.11) as

$$\mathbf{m}^{est} = \mathbf{G}^{-g}\,\mathbf{d} \tag{4.12}$$

[e.g., *Menke*, 1989], where $\mathbf{G}^{-g}$ is called the generalized inverse. Solution of the generalized inverse depends on the position of the problem. In seismic tomography, there are usually many more data than model parameters, making the inverse problem nominally overdetermined. Under the assumption of normally distributed data errors, minimizing the squared prediction error $\mathbf{e} = \mathbf{d}^{obs} - \mathbf{d}^{pre}$, leads to the

$$\textit{least squares solution} \qquad \mathbf{m}^{est} = (\mathbf{G}^T\mathbf{G})^{-1}\,\mathbf{G}^T\mathbf{d} \tag{4.13}$$

[e.g., *Menke*, 1989], where the superscript T stands for the transposed. Because $\mathbf{G}^T\mathbf{G}$ is square, it is theoretically invertible. In practice, however, not all parts of the model are resolved, putting $\mathbf{G}^T\mathbf{G}$ close to singular, and inhibiting a stable inversion. To still obtain a meaningful solution, small or zero eigenvalues values can be *damped* by adding a *damping parameter* ε^2, modifying (4.13) to the

$$\textit{damped least squares solution} \qquad \mathbf{m}^{est} = (\mathbf{G}^T\mathbf{G} + \varepsilon^2\,\mathbf{I})^{-1}\,\mathbf{G}^T\mathbf{d}, \tag{4.14}$$

where $\mathbf{I}$ is the unity matrix. This solution is also called stochastic or Levenberg-Marquardt inverse. ε^2 can be understood as taring between prediction error and solution length. The damped least squares solution is also applied in the tomographic inversion of this study.

4.2.5 Resolution and Covariance

The strength of inverse theory compared to other modeling techniques is, that it provides formal means to quantify resolution and errors of a derived solution. One of these tools is the model resolution matrix $\mathbf{R}^m$, that relates the true[1] model parameter $\mathbf{m}^{true}$ (for which $\mathbf{G}\mathbf{m}^{true} = \mathbf{d}$ holds) to the inverted ones, $\mathbf{m}^{est}$ (4.12). We can write

$$\mathbf{m}^{est} = \mathbf{G}^{-g}\,\mathbf{d} = \mathbf{G}^{-g}\left[\mathbf{G}\mathbf{m}^{true}\right] = \left[\mathbf{G}^{-g}\mathbf{G}\right]m^{true} = \mathbf{R}^m\mathbf{m}^{true}. \tag{4.15}$$

---

[1]*true* has to be understood as *true* within the model parametrization, but not in terms of the real earth. m^{true} are the unknown model parameters that solve the forward problem (4.11).

$\mathbf{R}^m$ is a $m \times m$ matrix, and m is the number of model parameters. Each row of $\mathbf{R}^m$ describes the dependence of one model parameter to all other parameters constituting the model. Because these rows describe how information concerning one parameter is spread to other parameters, they are also called *averaging vector*. For a data set, where all model parameters are perfectly resolved, $\mathbf{R}^m$ would be the unity matrix, that is each averaging vector is perfectly peaked, containing only the diagonal element (DE) surrounded by zeroes. But because realistic data is never perfectly resolved, and the solution has to be damped, there are off-diagonal elements in the averaging vector. Figure 4.3 displays a 3-D mesh plot of an averaging vector from our tomographic model, i.e. each element is

Figure 4.3: 3-D view of an averaging vector. The central peak corresponds to the diagonal element (DE). Off-diagonal elements are significant only above and below the DE, indicating vertical smearing.
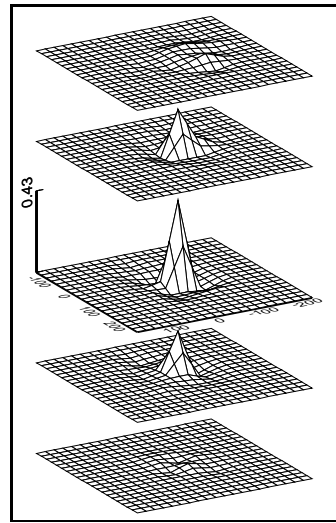
plotted at its spatial position. The central peak corresponds to the DE, but off-diagonal elements, especially in the adjoining upper and lower layers, reach a significant fraction of the size of the DE, indicating vertical smearing. Because it is impossible to plot each averaging vector, often only the scalar DE's are displayed for each model parameter. Another possibility, that accounts for the *peakedness* of the averaging vector, is the use of the spread function [*Menke*, 1989; *Michelini & McEvilly*, 1991] that compresses each row r_j in $\mathbf{R}_m$ to a single number according to

$$S_j = \log \left[\|r_j\|^{-1} \sum_{k=1}^{L} \left(\frac{r_{kj}}{\|r_j\|} \right)^2 D_{jk} \right]. \tag{4.16}$$

$\|r_j\|$ is the L_2-norm of the averaging vector, its size, and D_{jk} is the physical separation in km of r_{jj}, the DE, from r_{kj}, an off-diagonal element corresponding to another node. The *spread value S_j* incorporates two aspects of resolution: the size of the averaging vector and its peakedness. A perfectly resolved model parameter has a zero spread value, whereas large values correspond to broad shapes of the averaging vector.

Another possibility that additionally displays directions of smearing, is contouring the averaging vector in fractions of the size of the DE [*Eberhart-Phillips & Michael*, 1998] (Figure 4.4).
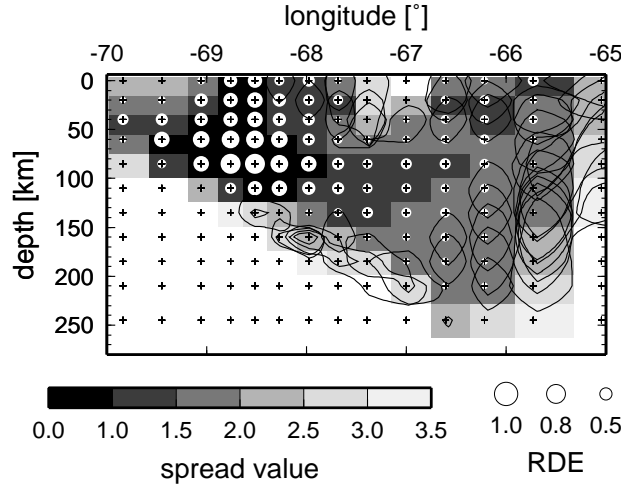

Figure 4.4: Different measures of resolution for one tomographic slice. Grey shades show the spread value, the size of the white circles is proportional to the value of the resolution diagonal element (RDE). Contour lines contour the averaging vector at 0.5 × RDE. Contours are only drawn if off-diagonal elements reach 50 per cent of the RDE. See text for further explanation.

The model covariance $\mathbf{C}_m$ describes how data errors are mapped into model space (e.g. *Menke* [1989]):

$$\mathbf{C}^m = \sigma_d^2 \, \mathbf{G}^{-g}(\mathbf{G}^{-g})^T, \tag{4.17}$$

where $\mathbf{C}^d = \mathbf{I}\,\sigma_d^2$ is assumed, that is data errors are independent and have a common variance σ_d^2, better knowledge is rare. The diagonal elements of $\mathbf{C}^m$ are the *standard errors* of the model, and the off-diagonal elements describe error correlation of the model parameters. It should be noted that the use of the standard error is limited as it often grossely underestimates the true error.

All of these measures and tools have been applied to our derived models. Additionally, tests on synthetic data have been performed to assess resolution and obtain error estimates of our final results.

The Computer Code `simulps`

`simulps` [*Evans et al.*, 1994] is a computer code for simultaneous inversion of 3-D structure and hypocentral parameter. It was originally developed by *Thurber* [1983], but experienced many modifications subsequently [e.g., *Eberhart-Phillips*, 1986, 1993; *Um & Thurber*, 1987; *Rietbrock*, 1996; *Haslinger*, 1998; *Thurber & Eberhart-Phillips*, 1999]. The structural model is defined on nodes at the intersections of a possibly unevenly spaced rectangular grid, and velocities between neighboring grid nodes are determined by linear B-spline interpolation. Parameter separation [*Pavlis & Booker*, 1980] is applied for the coupled hypocenter-velocity problem. The damped least squares solution of the velocity model equations is resolved by Cholesky Decomposition. The newest version of the code allows linking of grid nodes in the inversion to form blocks of constant velocity or gradient [*Thurber & Eberhart-Phillips*, 1999]. If desired, the code computes the full resolution and model covariance matrices. Ray tracing is done by a two step procedure using approximate ray tracing and pseudo bending [*Um & Thurber*, 1987]. In a recent version [*Haslinger*, 1998], a precise shooting ray tracer has also been implemented. Inversion for v_p, v_s, v_p/v_s, and Q is possible.

4.2.6   The Forward Problem

To evaluate the forward problem $\mathbf{d} = \mathbf{Gm}$, it is necessary to compute the path integrals (4.2), (4.5), and (4.8) for the v, v_p/v_s, and Q problems. In tomography this is done by ray tracing. Calculating ray paths and travel times through a 3-dimensional velocity field, although well established [*Červený et al.*, 1977], is still costly. The size of the forward problems kept abreast with the ever increasing computer power. To calculate 50 000 rays in a 600 km×600 km×300 km model (the size of the problem in this study) for several iterations, accurate solutions of the ray equation (such as finite-difference, shooting, or bending techniques) are still too expensive. In the computer code used in this study, `simulps`, an approximate ray tracer (ART) is implemented. In a two step procedure, the model between source and receiver is first scanned by a large number of circular arcs of different curvature and dip angles, and the fastest one is selected as the approximate ray [*Thurber*, 1983]. In a second step, this initial ray is piecewise perturbed to minimize travel time along small segments (pseudo bending, PB). This is done iteratively until the travel time of the path converges [*Um & Thurber*, 1987]. Although *Um & Thurber* [1987], and many other studies using the technique, show that in many instances ART and PB yield a minimum time ray path, convergence is not guaranteed. Because it is a perturbation method, the initial ray provided by ART has to be close to the true ray for PB to succeed. Further, PB only works in velocity gradients, but not if there are large sections of constant velocity. The latter problem becomes acute, if parts of the model

nodes are linked together [*Thurber & Eberhart-Phillips*, 1999] in the inversion. It has been pointed out [*Eberhart-Phillips*, 1986; *Haslinger*, 1998] that especially for long rays ($\geq$ 60 km) caution is appropriate.

We made two changes to the ART/PB algorithm to obtain more accurate travel times for the long rays in the subduction zone environment of this study (*Rietbrock*, personal communication 1999). First, we force the ray to have no curvature for path segments for which PB does not succeed. This is always the case, when there are sections of constant velocity. Thus rays are straight, instead of arcuate, in constant velocity regions. Tests with simple velocity models of large constant velocity blocks (slab, mantle wedge), and comparison to a finite difference (FD) [*Podvin & Lecomte*, 1991] and a shooting algorithm [*Virieux et al.*, 1988; *Haslinger*, 1998] showed that travel times are much improved, especially for rays that travel long distances in the mantle or slab.

However, if the model is inverted freely, than the above change does not help, because the model parametrization of `simulps` always has velocity gradients between nodes. Travel time errors for the long rays result mainly from the constant curvature arcs initially used in ART. This is not appropriate for the Benioff events, for which rays first travel through the slab or in the mantle with small velocity gradients before they penetrate the crust. As a modification we bisect the initial ray found by ART. For the two segments both ART and PB is performed again, refining the initial ray. Additionally, the number of segments constituting each ray is raised compared to the original code. The modifications are demonstrated in Figure 4.5a) and b), where the original ART/PB and the modified one are compared to a FD algorithm [*Podvin & Lecomte*, 1991] for two events. It is clearly demonstrated that for the long rays, the constant curvature arcs are not appropriate. The refinement of ART/PB produces rays and travel times that are close to the FD ones, only where there are very heterogeneous velocities, significant deviations occur (4.5 b, arrow). The scatter between man: and ART/PB travel times (sometimes the ART/PB rays are faster than the *correct* FD ones) is probably due to the different parameterizations and numerical limitations (the FD grid has a 2 km spacing). Travel time errors rarely exceed 0.1 sec. Although this is in the order of picking accuracy, it is less than 0.5 per cent of the total travel time for longer rays, and should affect the results only minorly.

4.3   Data

We combined local earthquake data from three temporary deployments each recording for about three months in 1994, 1996, and 1997. Although the deployments did not coincide in time, spatial overlap was achieved by re-occupying existing sites. The three experiments
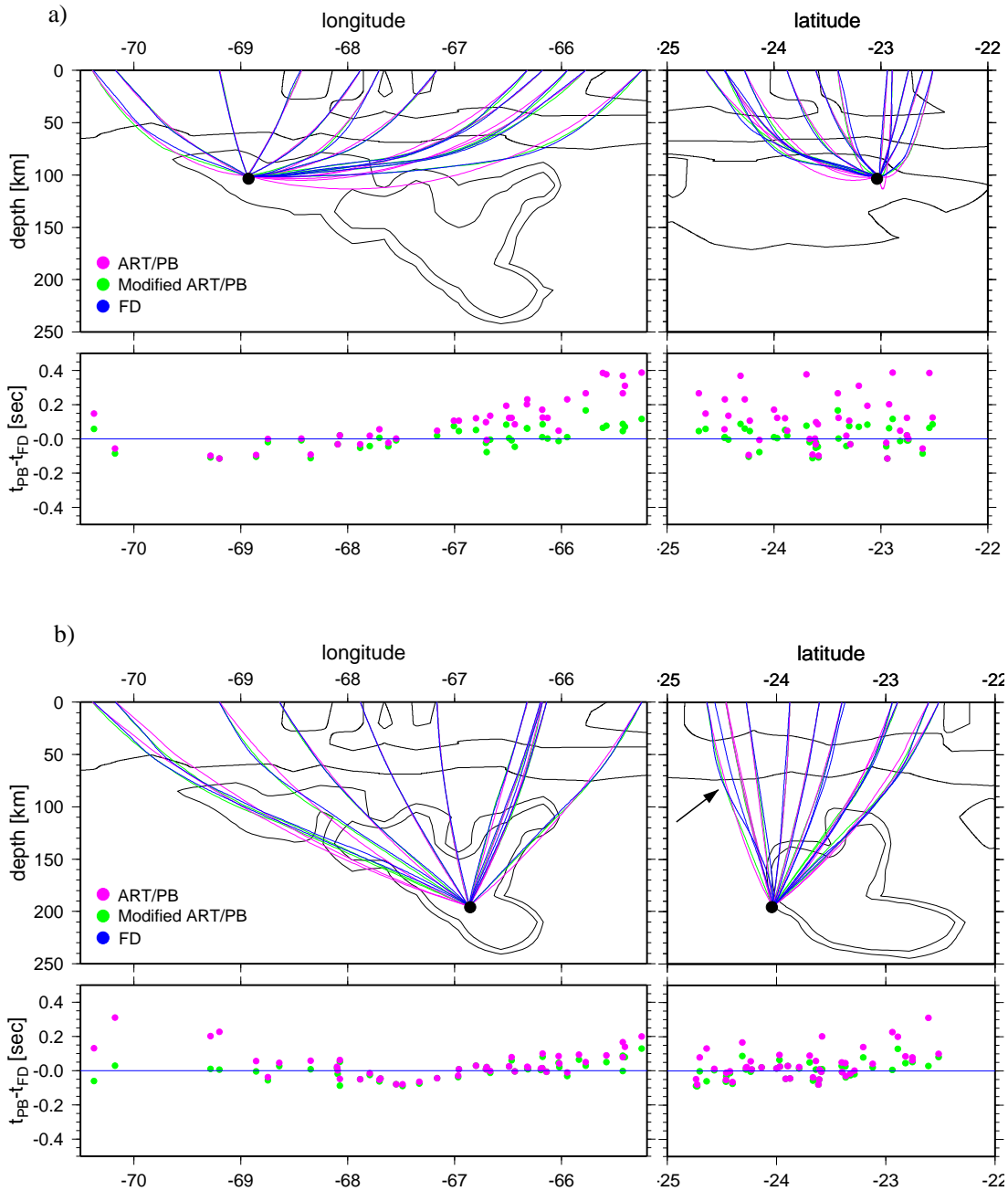
Figure 4.5: Rays and travel times for different ray tracing algorithms. Rays are traced through realistic velocity model derived from our data for two exemplary events (a and b). For clarity, only a few rays are plotted, whereas travel times for the entire network are shown. The ART/PB raytracer and its modified version are compared to a FD algorithm. The original ART/PB travel times and rays diverge considerably from the FD ones at long distances, because of its constant curvature arcs. The modified code delivers rays and travel times similar to the FD algorithm ($t_{PB}-t_{FD} \leq 0.1$). Only where there are strong velocity contrasts, there is significant discrepancy between the ray paths (e.g. arrow in b)).

covered different parts of the subduction complex between 20° and 25° South and between 65° and 70° West (Figure 4.6). The PISCO'94 seismological experiment covered the
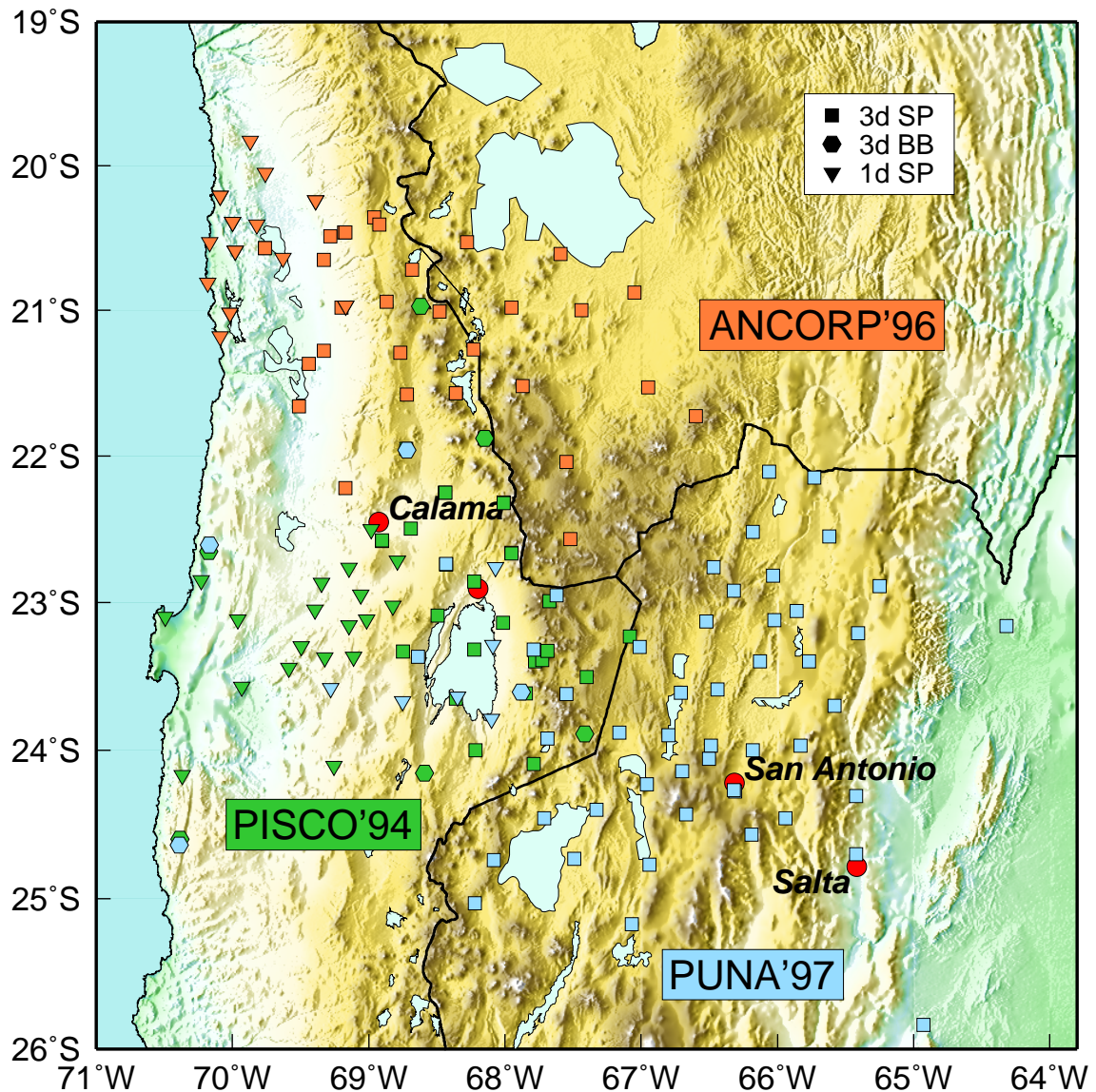

Figure 4.6: Topographic map of the station arrays used in this study. The different symbols mark seismograph locations and are coded after seismograph type (legend: SP short-period, BB broad-band) and deployment (color). Inverted triangles (1-D seismographs) are networks operated by Universidád de Chile.

eastern forearc and the volcanic arc of Chile between 22°S and 24°S [Figure 4.6, *Graeber & Asch*, 1999]. PISCO data is complemented by travel times from a temporary deployment of the Universidád de Chile, Santiago, south of Calama and a permanent network around Antofagasta. The passive part of the ANCORP'96 experiment extended PISCO coverage to 20°S in the north and additionally placed eight seismographs on the backarc of the Bolivian Altiplano; unfortunately, due to logistical difficulties and bad weather, only

few data could be recovered from these stations. For details of the deployment refer to *Haberland* [1999]. Additionally, travel times from a deployment of the Universidád de Chile near Iquique are included. The PUNA'97 array (Chapter 3) was centered on the Puna plateau in the Argentine backarc region. The forearc and Chilean arc were also covered by stations on former PISCO sites and seven one-component seismographs operated by Universidad de Chile (Figure 4.6). All three experiments were very similar in instrumentation and set-up. Most sites were equipped with *PDAS* data loggers and *MARK L4-3d* short-period (eigenfrequency 1 Hz) three component seismometer. The seismographs' internal clocks were synchronized to universal standard time using the Global Positioning System; accuracy should be within 10 ms. Most stations recorded continously 100 samples per second. Average station spacing was about 40 km.
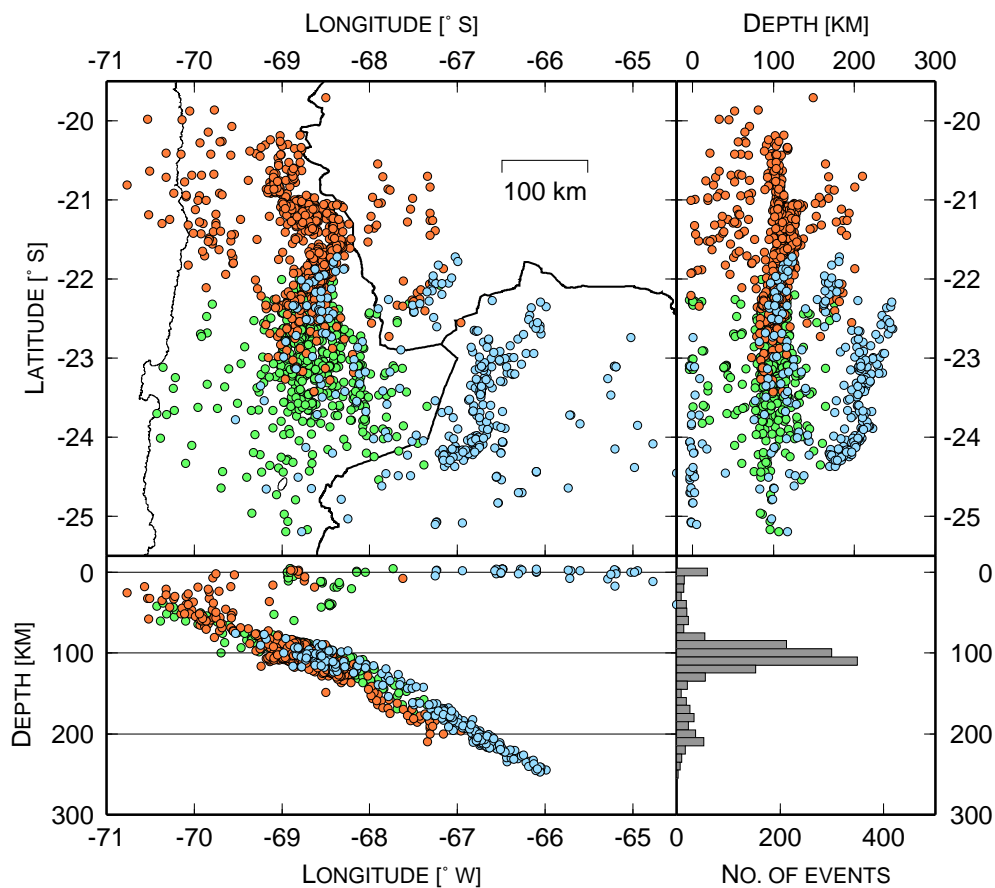

Figure 4.7: Epicenter map, E-W and N-S hypocenter projections of events used in this tomographic study. Color scheme is the same as in Figure 4.6 for the three data sets. Most events are of intermediate depth and occur around 100 km and 200 km depth.

Figure 4.6 shows locations of the earthquakes used in the travel time tomography. Earthquake epicenters overlap where the three networks join, improving resolution especially in those regions of the model that were critical for the individual data sets. Most events are of intermediate depth (100 - 250 km), originating in the Wadati Benioff Zone of the subducted Nazca plate. Crustal events are rare and mostly very shallow. Events are not evenly distributed, but occur in several elongated clusters at different depth intervals. Distribution of earthquake hypocenters is crucial for the screening of the model volume, and thus for the spatial resolution capability of the data set. Lack of events shallower than 80 km certainly hampers resolution at crustal depths, this is especially true for the eastern part of the model. These effects will be discussed more quantitatively later on (Chapter 4.4).

Data used in this study are P and $S - P$ travel-times, earthquake locations, and t^* parameters calculated by inversion of P-wave spectra. For PISCO and ANCORP, these data had already been carefully selected and picked in the previous tomographic studies [*Graeber & Asch*, 1999; *Haberland*, 1999; *Haberland & Rietbrock*, 2000; *Rietbrock & Haberland*, 1998]. The data-sets were adopted as they were, only the maximum azimuthal gap of 270°, previously allowed for the travel-times to cover parts of the model that are now better constrained by the additional data, was reduced to 230° . This same constraint was applied for the PUNA travel time data. Additionally, in the prominent cluster between 24.5°S and 23.9°S at 200 km depth only the best located events (number of picks $\geq$ 45) were kept to obtain an evenly distributed ray coverage and reduce bias from redundant data. This lead to 1558 events (571 from PISCO, 669 from ANCORP, and 318 from PUNA), 33,018 P arrival-times and 17,123 S arrival times, recorded at more than 150 stations. t^* data for PISCO and ANCORP are based on the data set of *Haberland* [1999]. Here events with a maximum azimuthal gap of 270° are accepted because the events do not have to be relocated in the Q_p inversion. The same criterion is applied for the PUNA data set. Spectral inversion of t^* for all three data sets has been done utilizing the same method [*Rietbrock*, 2000] and set of parameters. 1501 events (20,145 t^* values) constitute the merged t^* data for Q_p inversion.

Seismogram examples with their associated spectra, as well as a map displaying whole path Q_p for two events recorded at the PUNA array are shown in Figure 4.8. Most seismograms are simple with impulsive direct arrivals and little coda. Only paths in and along the slab into the forearc (e.g. station JER) show strong coda and much higher frequency content (and also high Q_p). Strong attenuation is visible in the raw short-period seismograms at many stations (note different amplitude scales in Figure 4.8). For some paths this leads to a complete lack of S energy. This is also seen in the shape of the P wave spectra, where it is exploited to determine the t^* operator.
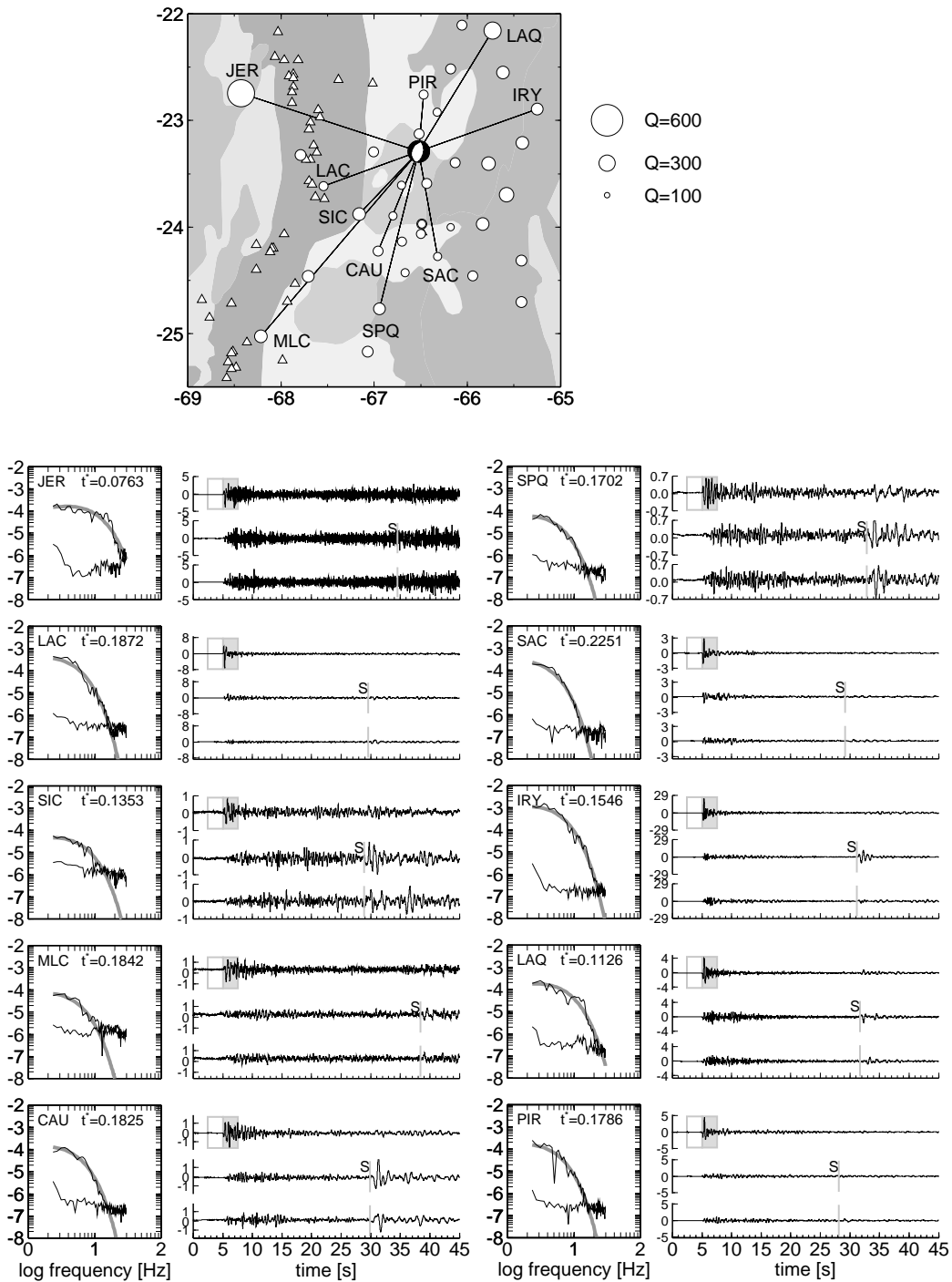
Figure 4.8: a) Velocity seismograms and *P*-wave spectra for an intermediate depth event recorded at the Puna network. Vertical (upper trace) and horizontal component seismograms are shown for the paths marked on the map. For the 2.56 second windows before and after the *P* arrival, noise and signal spectra, as well as the modeled spectra (thick grey line) are shown. On the map, the size of the white circles is scaled after whole-path-*Q* calculated from the *t** parameter and travel time. Q_p is high for paths to the west (forearc) and east (Eastern Cordillera), and low for stations in the Puna.
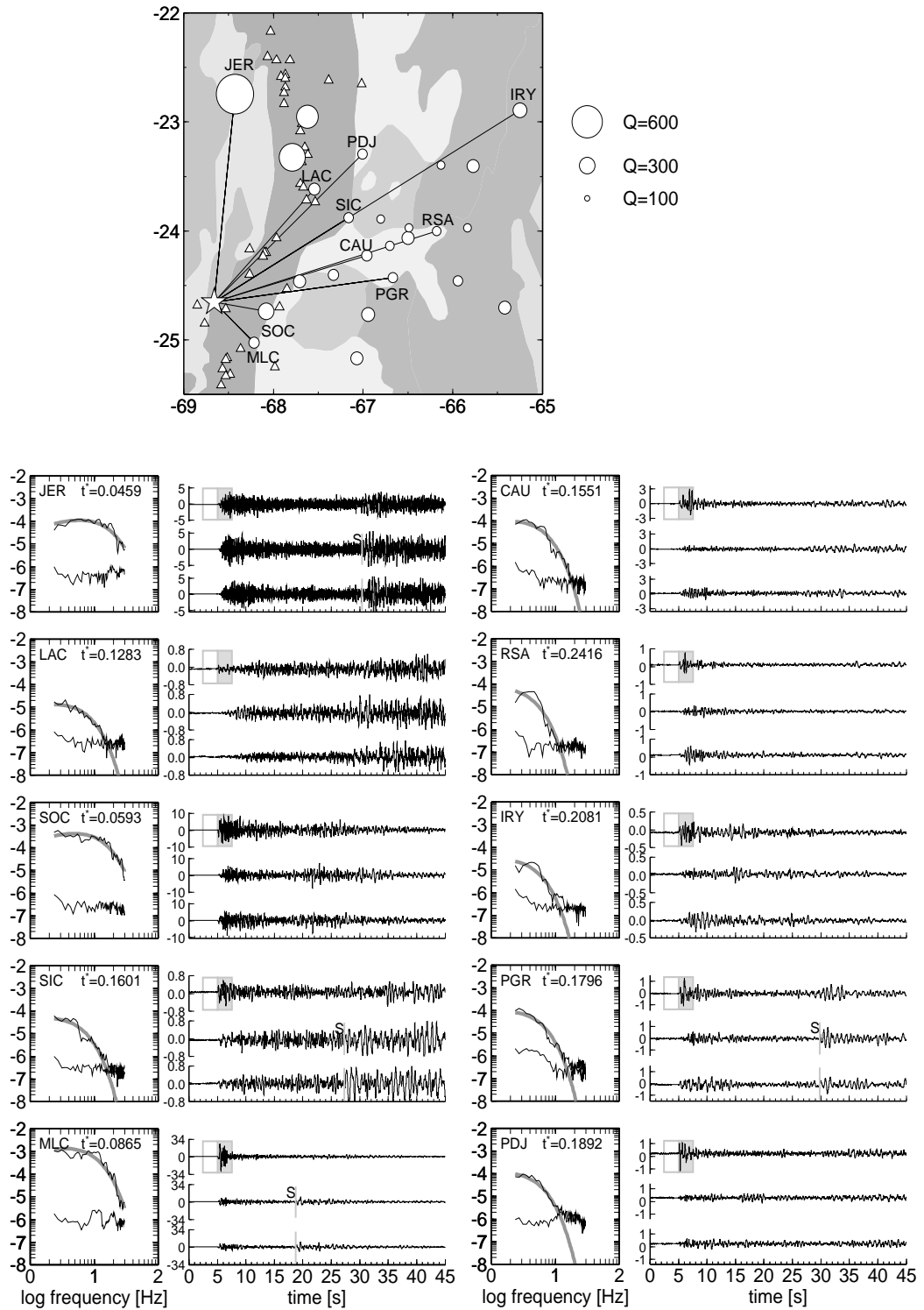
Figure 4.8: b) Velocity seismograms and *P*-wave spectra for an intermediate depth event recorded at the Puna network. See Figure 4.8a for detail.

All travel times were hand-picked and weighted after an estimated uncertainty. These weights were used later on in the inversion procedure. P picks, due to their impulsive onset, could often be determined within a few samples accuracy. S picks were made on rotated and integrated records to avoid compressional wave precursor and enhance the low frequency signal. S arrival times at stations in the Western Cordillera and on the Puna plateau are few and often inaccurate due to the very strong attenuation (Figure 4.8).

t^* operators were determined from amplitude spectra of 2.56 second time windows following the P arrival (Figure 4.8). These short time windows assure that influence from scattering is reduced in the estimation of spectral parameters. For each signal spectrum, a noise spectrum was also determined from a time window preceding the P wave. A signal to noise ratio of three in a continuous portion of the spectrum was required for t^* to enter the Q_p inversion. The high spectral decay and low signal energy of S waves at many stations prohibited a comprehensive Q_s analysis.

4.4 Resolution and Synthetic Models

To gauge resolution and errors we exploit the model resolution matrix as in chapter 4.2 and invert a synthetic data set with the identical ray geometry as the real one. Figures 4.9, 4.10, and 4.11 show spread values (grey shades) and resolution diagonal elements (white circles) for the three inverted attributes. 70% contours of the averaging vector are also drawn for those nodes for which off-diagonal elements reach 70% of the RDE. Absolute values of spread and RDE's strongly depend on damping, thus only their relative size is interpreted. For velocities and Q_p, resolution is best in the forearc above the clustered earthquakes at 100 km depth, where ray coverage is densest. Vertical smearing occurs mainly in the uppermost layers. Q_p and v_p/v_s lack data from the western vertical short-period instruments operated by the Universidad de Chile, causing diminished resolution there. North of 22.8°S, resolution in the backarc (east of 68°W, Altiplano) is low, and significant smearing is indicated by small spread values and averaging contours. South of 22.8°S, where the backarc is covered by the PUNA network, resolution is quite evenly distributed and good to fair everywhere but the margins of the model. Smearing is mostly vertical and occurs for the shallow and easternmost nodes. Smearing is more severe for Q_p and v_p/v_s, because important sub-horizontal rays from earthquakes in the forearc are fewer due to strong attenuation and low signal to noise ratios. Here anomalies may be recovered, but their geometry is probably blurred. For each attribute a threshold for the spread value has been chosen to separate high and low resolution. The choice is based on the relative size of the spread and on synthetic experiments. These spread contours are marked by the thick black lines in Figures 4.9, 4.10, and 4.11, and are also drawn into the tomographic models introduced later. As their choice is somewhat arbitrary, they should be considered with the necessary caution.

Tests with synthetic data have been conducted to reveal inherent limitations in resolution and possible artefacts due to event station geometry and chosen parameterization. We trace the same rays as in the respective real data set through a synthetic model to calculate travel times and t^* operators. Realistic, normally distributed, random noise, scaled to the individual estimated pick uncertainty for the travel times, and with a constant standard deviation of 0.008 seconds for t^* is added to the synthetic data. The synthetic models have the same geometry with positive and negative anomalies of realistic size and amplitudes, including a fast (high Q) slab to mimic subduction zone specific ray paths (Figure 4.12). The synthetic data sets have been inverted applying the same procedure as the for the real data that is outlined in Chapter 4.5. The inverted models are shown in Figures 4.13, 4.14, and 4.15. Resolution contours determined for the real data are also plotted.

For all three attributes shallow structures in the forearc and arc are recovered well. In the
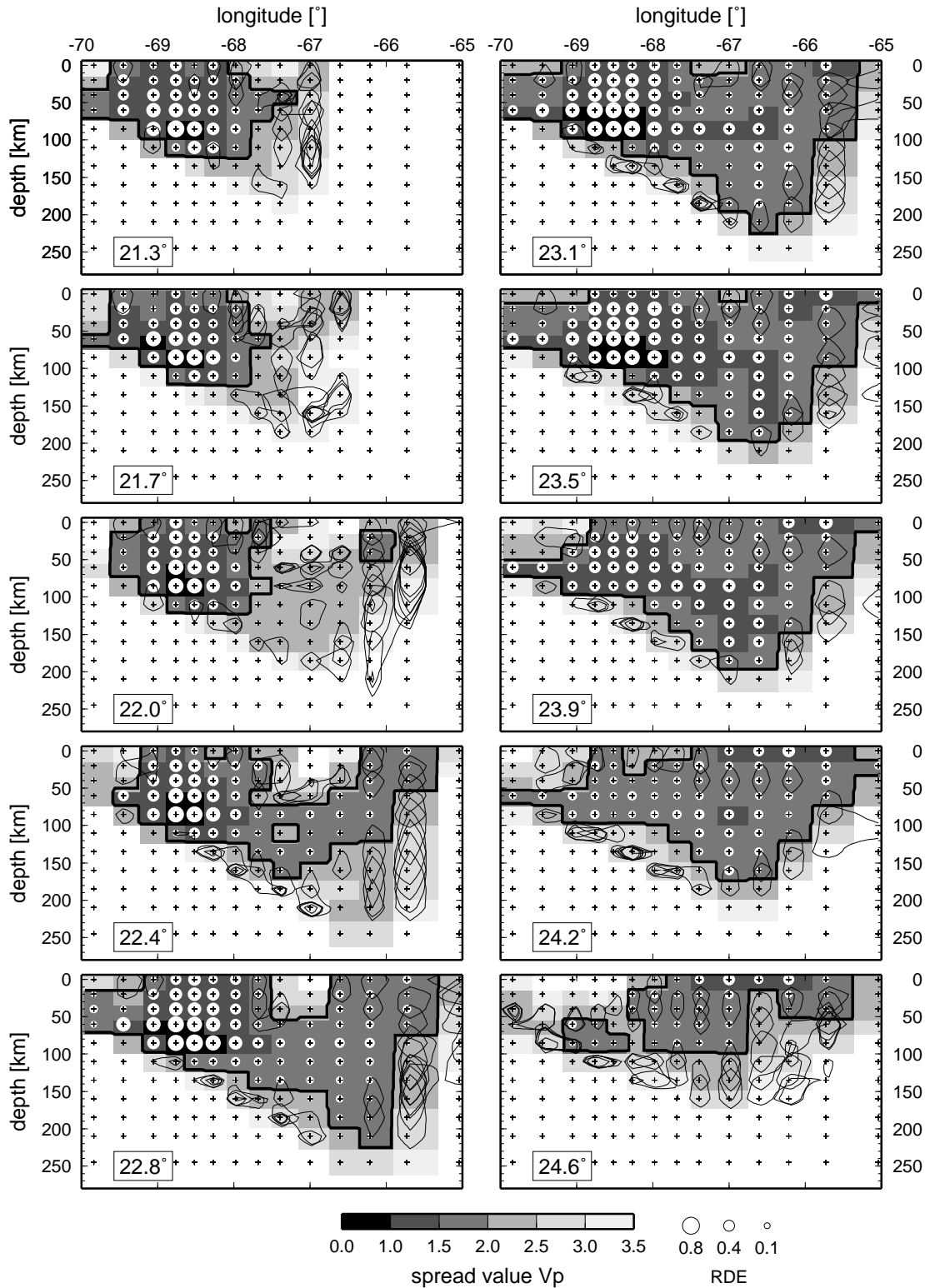
Figure 4.9: Spread values (grey shades) and resolution diagonal elements (RDE, white discs) for the v_p inversion nodes in latitudinal cross sections. Dark shades and large discs indicate good resolution. Super-imposed are 70% contour lines of the averaging vector to visualize spatial smearing (see text for further explanation). Contour lines are only drawn for nodes where off-diagonal elements reach 70% of the RDE.
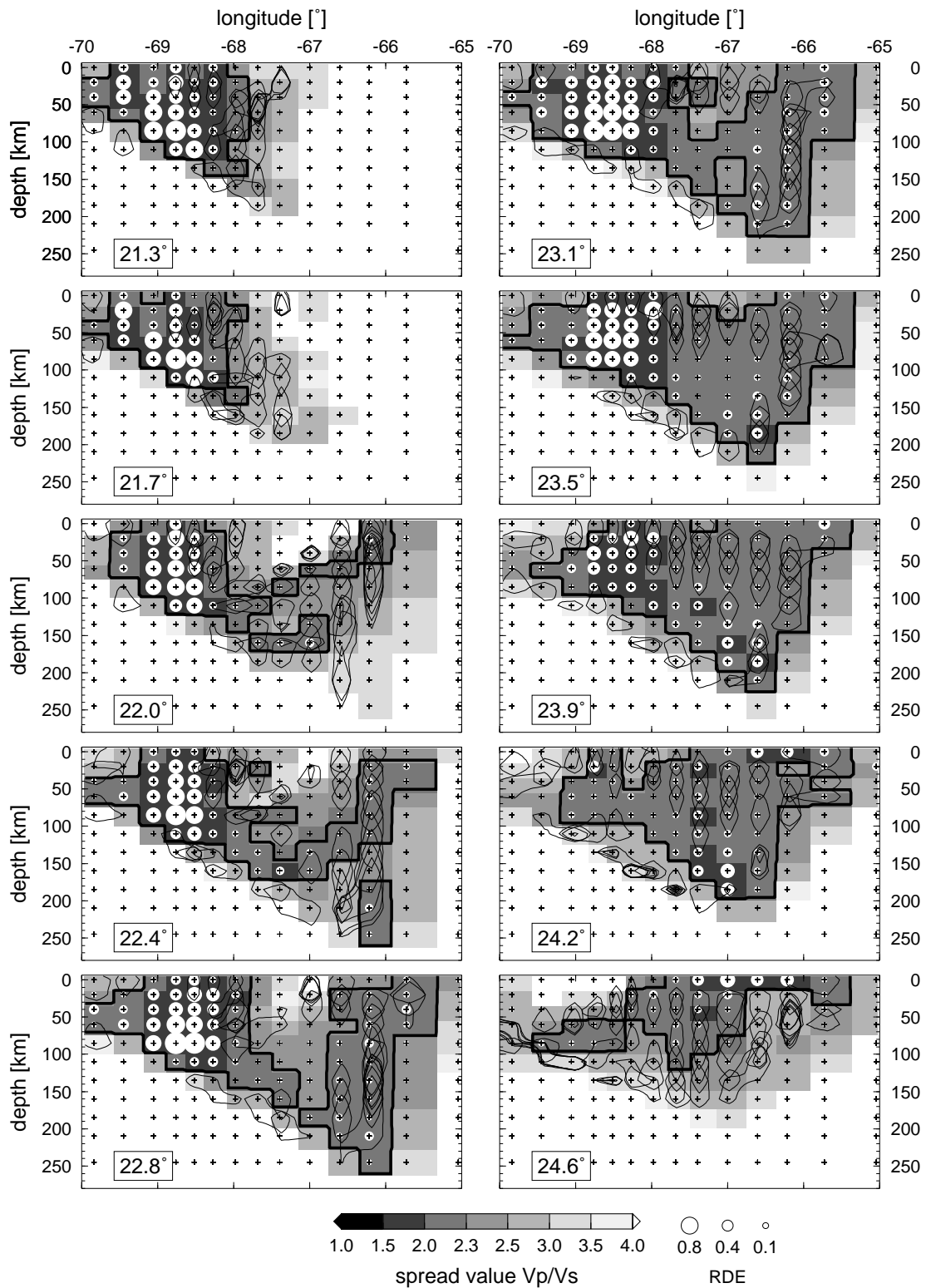
Figure 4.10: Spread values (grey shades) and resolution diagonal elements (RDE, white discs) for the v_p/v_s inversion nodes in latitudinal cross sections. See Figure 4.9 for more detail.
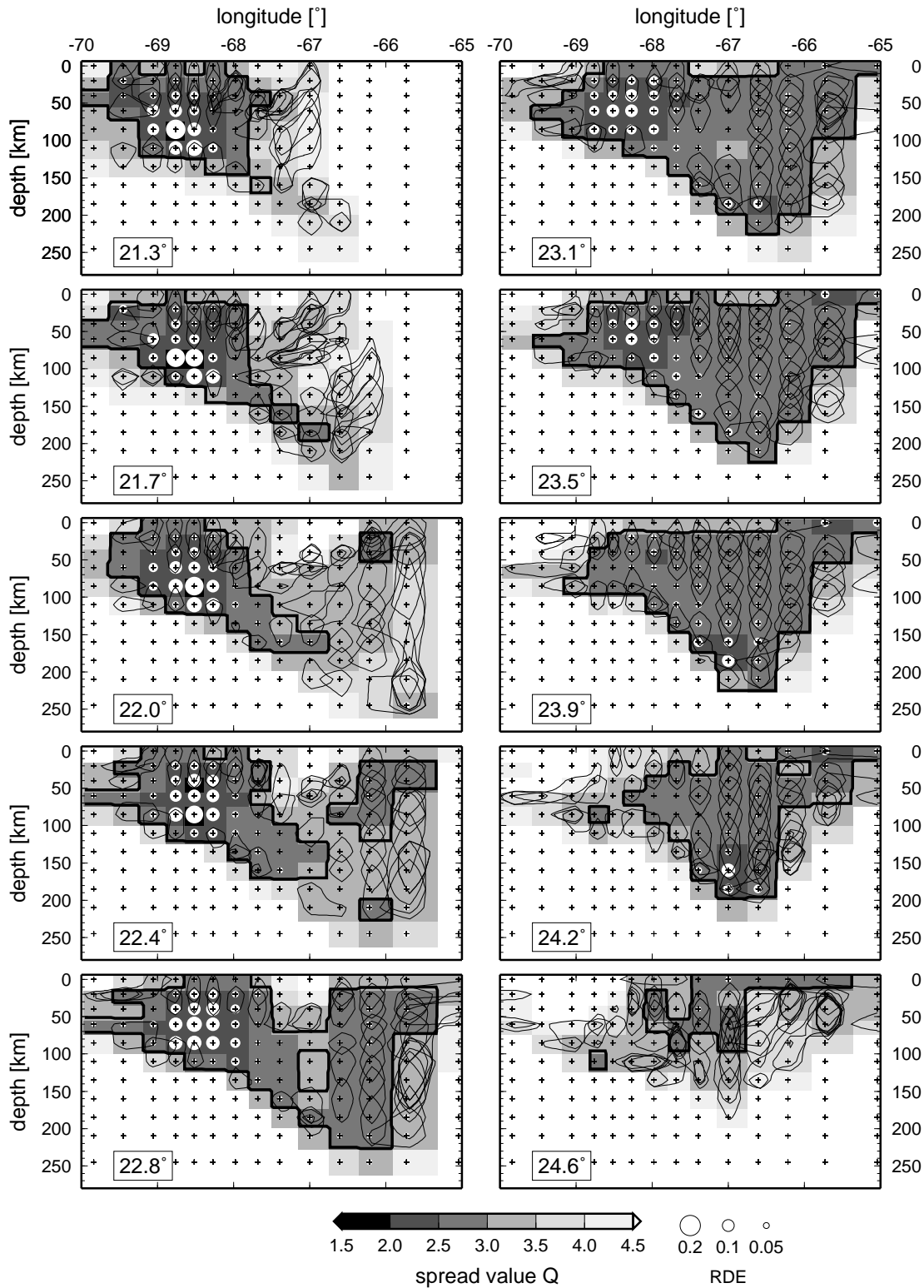
Figure 4.11: Spread values (grey shades) and resolution diagonal elements (RDE, white discs) for the Q_p inversion nodes in latitudinal cross sections. See Figure 4.9 for more detail.
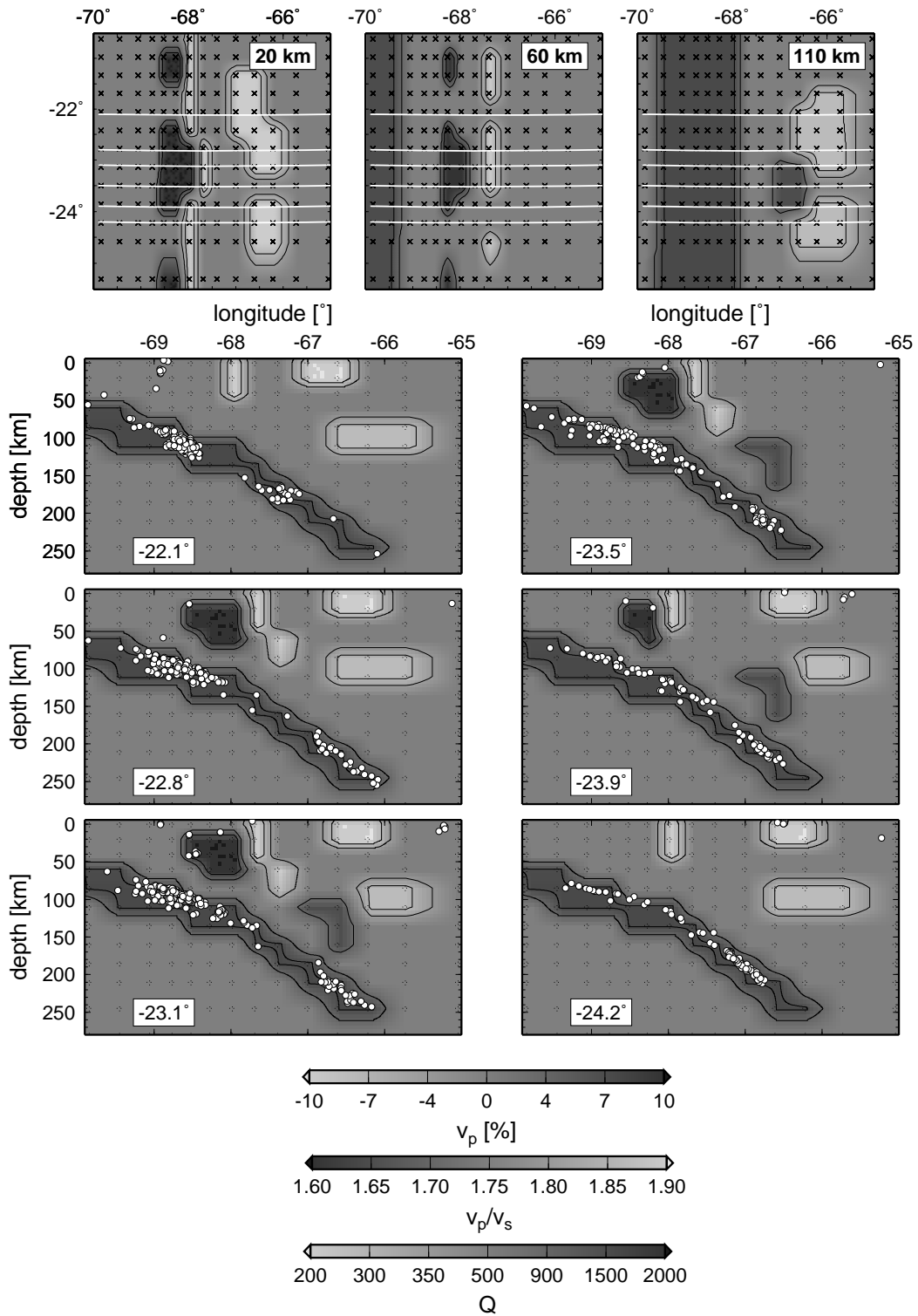
Figure 4.12: Input model for synthetic tests. Upper panel shows three depth slices in map view, lower panels show latitudinal cross sections. Locations of the cross sections are indicated by horizontal lines on maps. Geometry of the model is the same for v_p, v_p/v_s, and Q_p. Anomalies are scaled according to the three color bars. Rays were traced through this model to obtain travel times and t^* as input for test inversions.

backarc they can only be retrieved in the regions covered by the PUNA network. Low v_p and low Q_p and high v_p/v_s anomalies beneath the WC and in the backarc are recovered with the right amplitudes in regions with good resolution. For v_p/v_s vertical smearing occurs probably due to few data. In the Altiplano, anomalies are only recovered at few places, where there are stations with sufficient data.

The slab is sharply reproduced for all three data sets, but shows gaps where there is no Benioff seismicity. v_p in the slab is overestimated at the deeper clusters (up to 0.3 km/s at individual nodes), Q_p is underestimated ($\approx$1000 vs. 1500 at some nodes), v_p/v_s is correct or slightly underestimated ($\approx$0.01) at some nodes.

The positive anomaly in the mantle wedge is recovered for the three data sets, but its shape is blurred by smearing. For v_p it is recovered correctly or with a slightly underestimated amplitude (0.1 km/s in the section at 23.1°S). The Q_p amplitude is underestimated (750-950 vs. 1500), v_p/v_s is too high (by up to 0.02). The negative anomaly in the eastern part of the mantle wedge is only partly recovered and its shape is blurred. Extreme smearing occurs in the north (e.g. 22.8°S) for v_p, whereas for Q_p and v_p/v_s it is not detected because of the lack of data.

In general v_p delivers the sharpest image of the structures for the three data sets. For Q_p, the positive anomalies' amplitudes are underestimated. Shallow structures are recovered well for all three attributes. In the mantle wedge, structures are recovered in the central part. In the east and north-east of the model, severe smearing along the ray paths occurs. Magnitude of errors (up to 0.3 km/s for v_p, over 500 for high Q_p regions, and up to 0.03 for v_p/v_s) can also be expected for the real data set. Note, however, that amplitudes of inverted anomalies are strongly influenced by the chosen damping parameter for the inversion. It can be expected that the inversions of the real data sets are affected by similar smearing effects. Regions of good resolution defined by the spread value are generally confirmed by the synthetic tests.
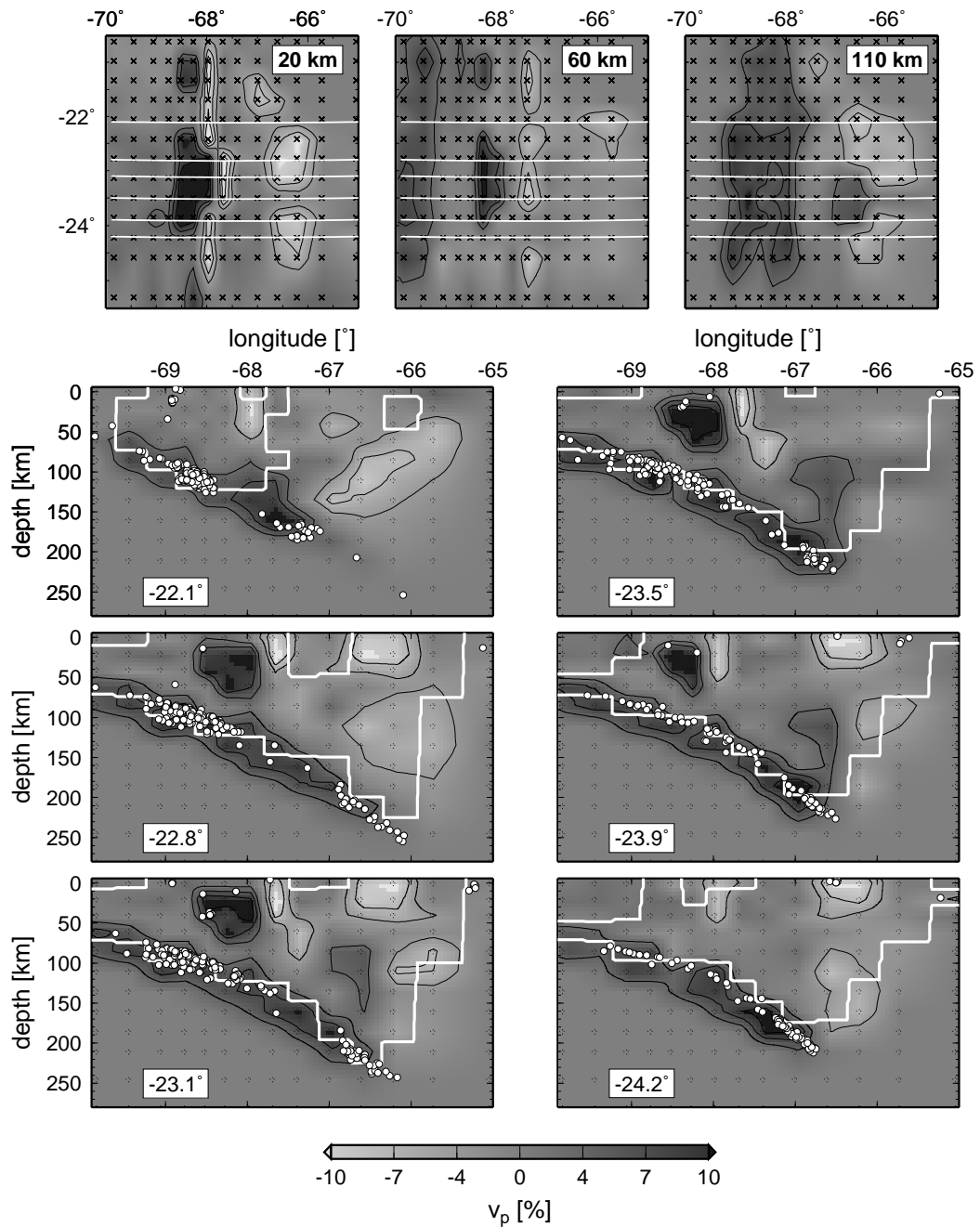
Figure 4.13: Reconstruction of synthetic v_p model. Input is shown in Figure 4.12. Superimposed is spread contour line from resolution analysis of the real data set.

Figure 4.14: Reconstruction of synthetic v_p/v_s model. Input is shown in Figure 4.12. Superimposed is spread contour line from resolution analysis of the real data set.

Figure 4.15: Reconstruction of synthetic Q_p model. Input is shown in Figure 4.12. Superimposed is spread contour line from resolution analysis of the real data set.
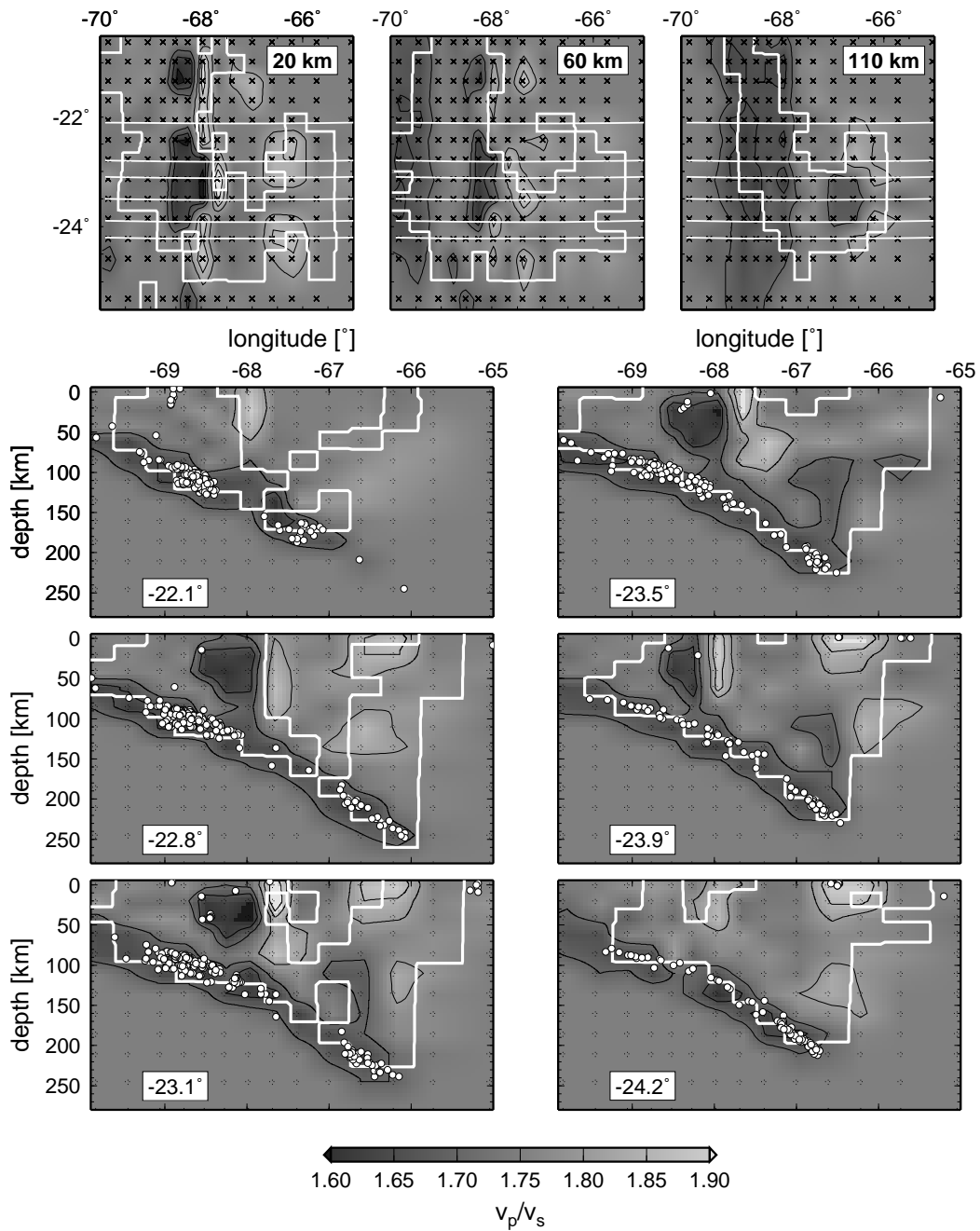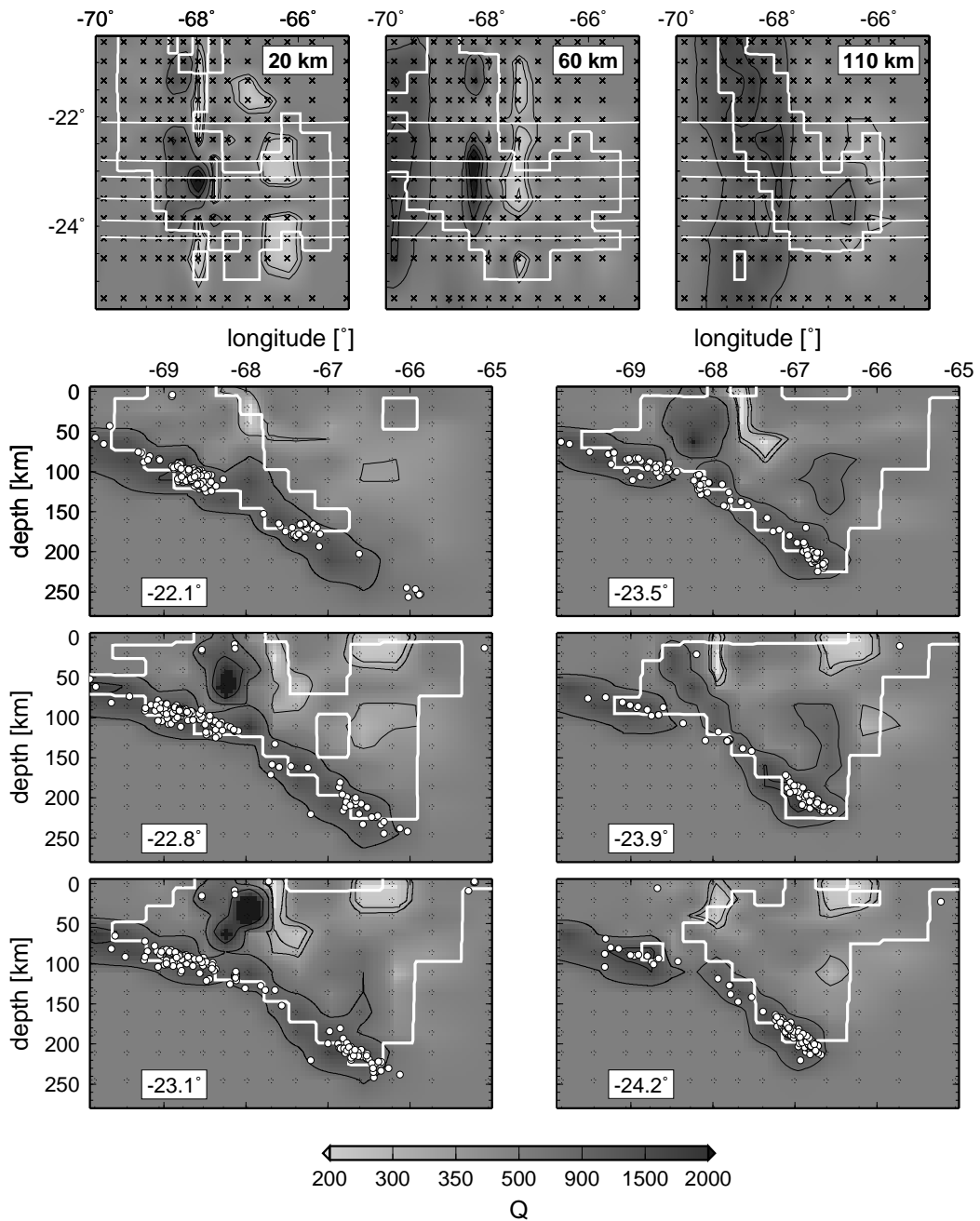
4.5 Inversion Procedure

4.5.1 Inversion Grid

The inversion grid dimensions determine the maximum spatial resolution of the model. They are chosen according to the station array at the surface, the earthquake distribution at depth, and the ray density in between. We commit to a horizontal spacing in east-west direction of 25 km in the forearc and arc, where ray coverage is densest, and $30 - 40$ km in the backarc. In north-south direction, parallel to the strike of the mountain range, nodes are 40 km apart (Figure 4.16). At depth, spacing is 20 km in the crust and 25 km in the mantle. Although resolution of small-scale heterogeneties is sacrificed for robustness, this is fine enough to resolve major tectonic structures and assures well resolved nodes over most parts of the model.

4.5.2 Starting Model

Because tomography is a linear approximation, model perturbations from a starting model are inverted. In general there is no guarantee to arrive at a global minimum, and choice of the starting model has to be reflected carefully. Different strategies can be adopted to derive a starting model for tomography. It can be pieced together from *a priori* knowledge from the literature or derived directly from the data. For an *a priori* model it is difficult to distinguish which features of the inverted model are required by the data, and which are remains of the starting model. A more objective approach is to derive a 1-D model directly from the travel time data ["minimum-1D" model, *Kissling et al.*, 1994]. The model represents ideally the average (weighted by the total ray length) of the true 3-D velocities in each layer and is not biased by a priori input other than the choice of layer depth and thickness. For our data set this seemed not quite ideal, and we deviate slightly from this approach for two reasons: (1) Our data set consists of three only partly overlapping networks that cover very different tectonic units. E.g. average crustal velocities in the forearc are fast [7 km/sec, *Graeber & Asch*, 1999] whereas backarc crust is slow [6 km/sec, Chapter 3.2, *Zandt et al.*, 1996]. Ray coverage in the forearc is much denser than in the backarc and thus an inverted 1-D model from the entire data set is biased by the fast forearc velocities. (2) The dominant structural anomaly influencing arrival times for the Benioff events is the fast subducted Nazca lithosphere. Because the longest rays in the mantle travel along the fast Nazca plate to the western network stations, 1-D velocities in the mantle are biased towards the anomalous high velocities of the slab (Chapter 3.2), and as such represent rather the anomaly than the background mantle. Because there is a strong trade off between earthquake depths and average velocities for our data
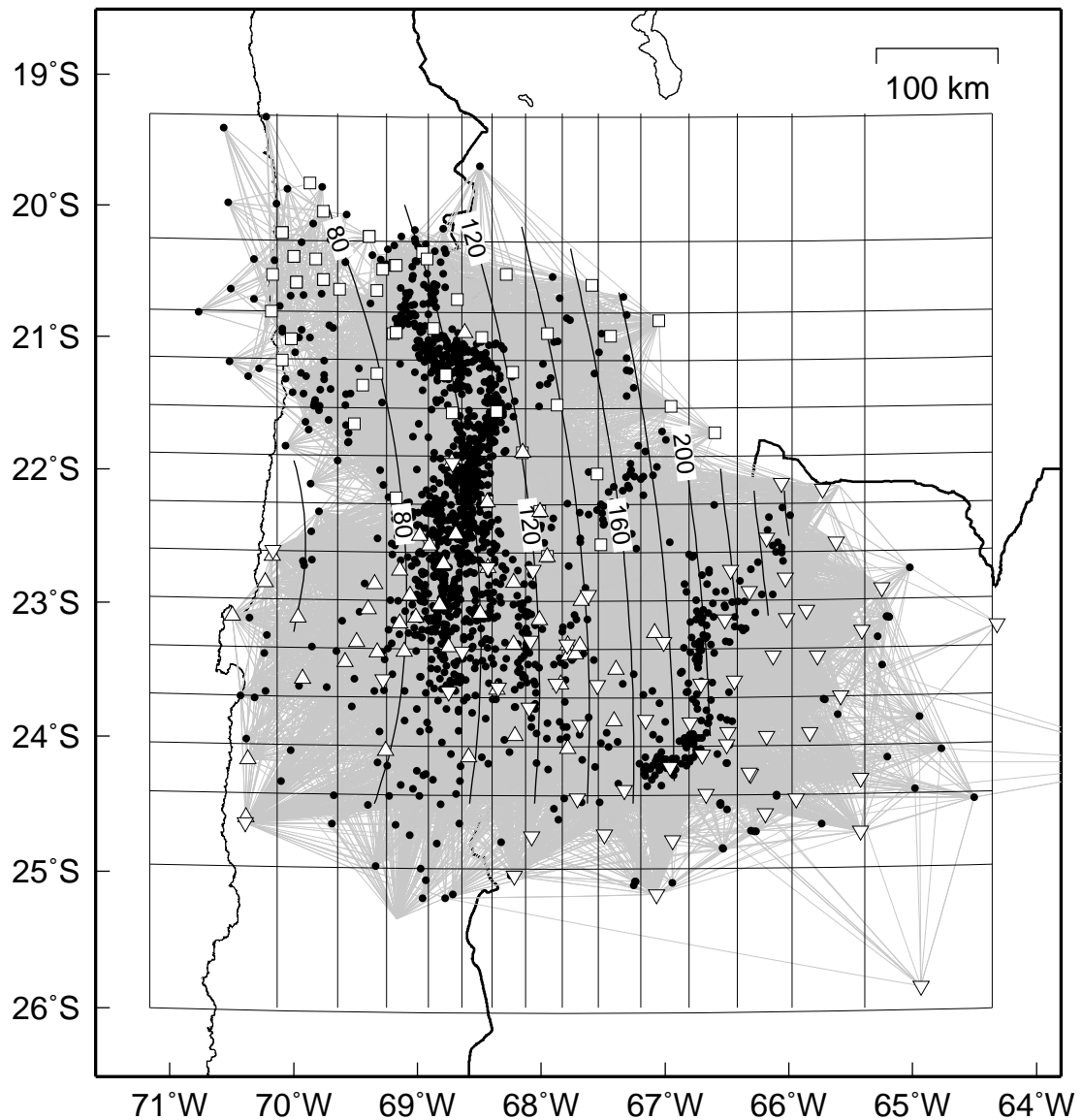
Figure 4.16: Map view of the inversion grid. Grid nodes are spaced 40 km in north-south direction, and 25–40 km in east-west direction depending on ray density. At depth, node spacing is 20 km in the crust and 25 km in the mantle. Epicenters, stations (different symbols for the three arrays), and connecting rays are also shown. Contour lines indicate earthquake depths.

set, such biases are not completely removed in the 3-D inversion. To account for these problems we parameterize the starting model differently. The crust is divided in three blocks, forearc, arc, and backarc. Crustal nodes start with 6.0 km/s in 20 km depth, and 6.5 km/s in 40 km depth in accordance with seismic data from *Wigger et al.* [1994]. At 60 km depth, nodes have a velocity of 7.5 km/s to represent a gradual transition

to mantle velocities. Within the three blocks these nodes can be adjusted to account for Moho depth variations. In the mantle we invert for a single slab and mantle wedge velocity. This is done in practice by tying inversion nodes of a 2-D grid together [*Thurber & Eberhart-Phillips*, 1999]. Starting mantle velocities are borrowed from the IASPEI model [*Kennett*, 1991]. A best homogeneous v_p/v_s ratio of 1.75 has been obtained from suite of inversions. We additionally invert for station corrections. Earthquake hypocenters input in this 2-D inversion have been located with a 1-D model having the stated starting velocities. In this way we construct a background model with little, yet well established a priori information that realistically parameterizes our specific problem yielding smooth background velocities and accurate ray paths and hypocenters.

As expected we obtain higher crustal velocities in the forearc than in the backarc (6.3 km/s vs. 6.1 km/s). The mantle wedge is with 8.2 km/s slightly faster than the global average for this depth interval [e.g., *Kennett*, 1991]. This is surprising considering that the data come from a subduction zone, where asthenospheric material and higher than average temperature are expected to reduce velocity. The subducted slab is with 8.55 km/s 4% faster than the ambient mantle. This is in accordance with other studies from subduction zones [e.g., *Zhao & Hasegawa*, 1993] and can be attributed to the low temperature of the subducted oceanic lithosphere.

Hypocenters, crustal and background mantle velocities (without the slab) of this model are used as a start for 3-D v_p inversion. For v_p/v_s, and Q_p we proceed from a homogeneous half space (v_p/v_s=1.75, Q_p=600), the 3-D v_p model and its hypocenters.
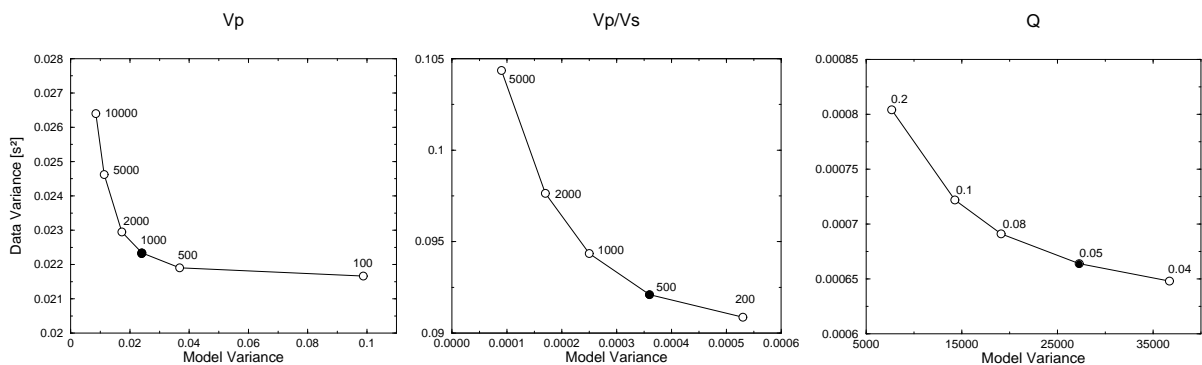
4.5.3   Damping

Figure 4.17: Trade-off curves to determine damping values for v_p, v_p/v_s, and Q_p. Model-variance is graphed against data-variance for different damping parameters. For the chosen damping values (filled symbols) low data- and moderate model- variance is achieved.

Another important parameter that strongly influences the inversion result and has to be selected carefully is the damping constant. Because damping weighs between solution length and data fit, an objective choice can be made from a trade-off-curve, graphing model-variance versus data-variance for different damping values [*Eberhart-Phillips*, 1986]. A good choice is a value that is close to the minimum data-variance yet yields only a moderate model-variance. Whereas often such curves are drawn for single iteration inversions, we calculated almost full inversions (5 iterations), comparing the variances of the final models. Trade-off curves and the chosen damping values are shown in Figure 4.17.

4.5.4 Data Fit

The 3-D models strongly reduce travel time (t^*) residuals (Figure 4.18). For the final models, the formerly broadly distributed and skewed residuals cluster symmetrically around zero, indicating successful inversions. The variance of the travel time (t^*) residuals is decreased by 77% for v_p, by 60% for v_p/v_s, and by 85% for Q_p.
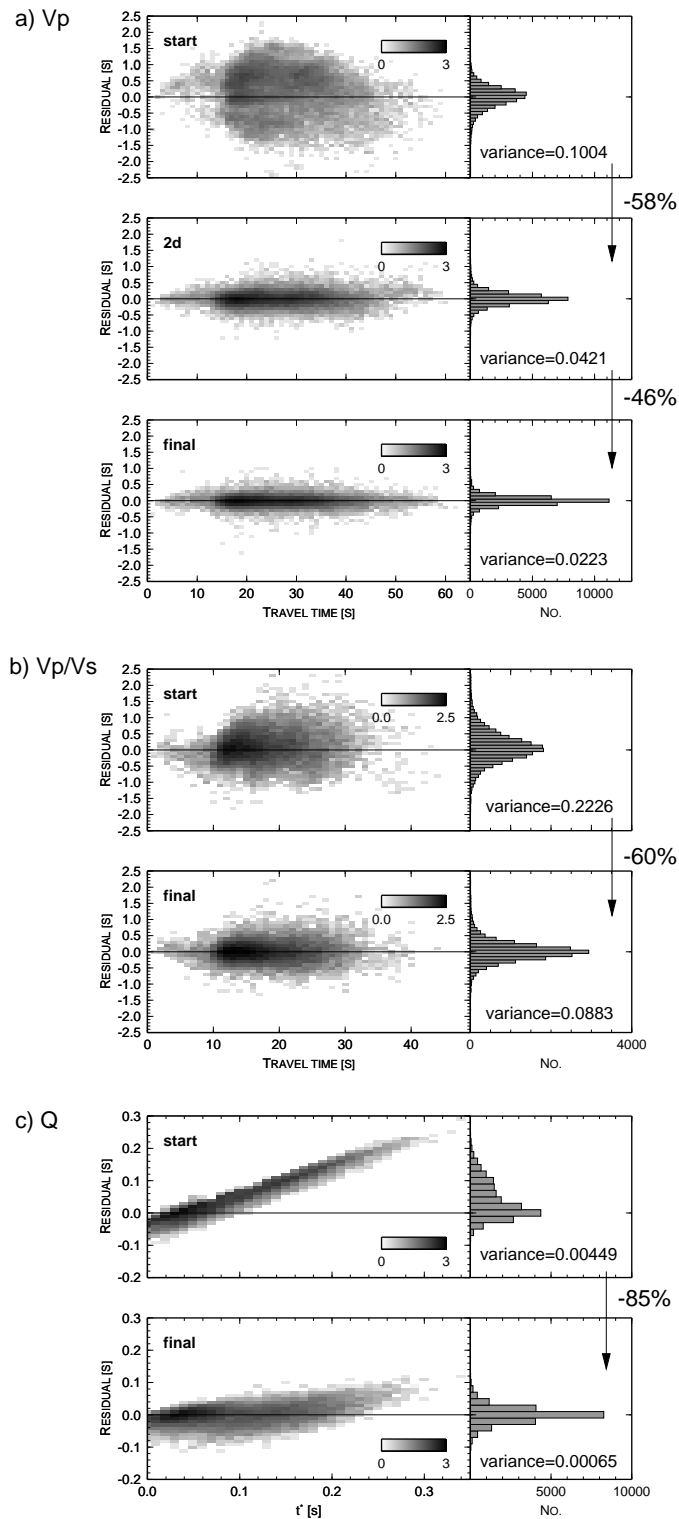
Figure 4.18: Travel time and t^* residuals are graphed against travel times and plotted as densities (logarithmic grey scale) before and after the inversions for **a)** v_p, **b)** v_p/v_s, and **c)** Q_p. Residual histograms are also shown. After the 3-D inversions residuals cluster symmetrically around zero, and data variances are drastically reduced.

4.6 Results

Results are presented on E-W cross sections and depth maps (Figures 4.19–4.24). The spread contour line enclosing regions of good resolution defined in Chapter 4.4 is superimposed, and the outside region of lower resolution appears in slightly faded color. v_p is represented as deviation of the 1-D starting model of Chapter 4.5. The relative deviations are more robust than absolute values, that have been found to be dependent on the starting model. Additionally, subtraction of lithological and pressure induced 1-D gradient reveals patterns that are depth independent and cross lithological contacts (i.e. Moho). Thus effects from variations in the state of the rocks, like temperature or the presence of water, are more easily seen, and comparison with the other two attributes is facilitated. Nonetheless, absolute values will be stated too, if necessary for the interpretation. Cross sections with absolute values for v_p are displayed in Appendix C. Based on our considerations for the background velocities (Chapter 4.5), absolute values, although less robust than deviations, should be the best estimates possible.

Because v_p/v_s and Q_p inversions start from a homogeneous half-space, and their values are not, to a first degree, pressure dependent, absolute values are plotted. We prefer to discuss attenuation in terms of Q_p instead of Q_p^{-1}, which is actually inverted for. Q_p is commonly used in the literature and absolute numbers are more familiar than Q_p^{-1} values. Actual sensitivity of the data to Q_p^{-1} is accounted for by the non linear color scale, that is equidistant in Q_p^{-1}. This means that there is much higher dynamic range for low Q_p than for higher Q_p. The seismic attributes reveal a heterogeneous crust and upper mantle system with sharp gradients and strong anomalies. Results are presented for the major tectonic units: forearc, Western Cordillera, slab, and the backarc plateau.

4.6.1 Forearc

v_p tomography reveals a relative fast forearc crust (6.5 km/s upper crust, 7 km/s lower crust), and reduced velocities (7.5 km/s–8 km/s) in the thin mantle wedge west of approximately 68°W. For v_p/v_s the forearc is the best resolved volume, containing many S picks that are not affected by strong attenuation. The forearc crust is characterized by normal v_p/v_s values (approximately 1.73–1.78) that are expected for intermediate lithology. The mantle wedge has clearly elevated v_p/v_s ratios (≥ 1.8, see 85 km depth map Figure 4.22). The anomaly is strongest in the northern sections, above the vigorous earthquake cluster in 100 km depth. To the south, with decreasing seismic activity, the anomaly appears to retreat to the east, beneath the Western Cordillera. Q_p shows a rather undifferentiated forearc with continuously high Q_p (600 – 2000). There are no differences between crust
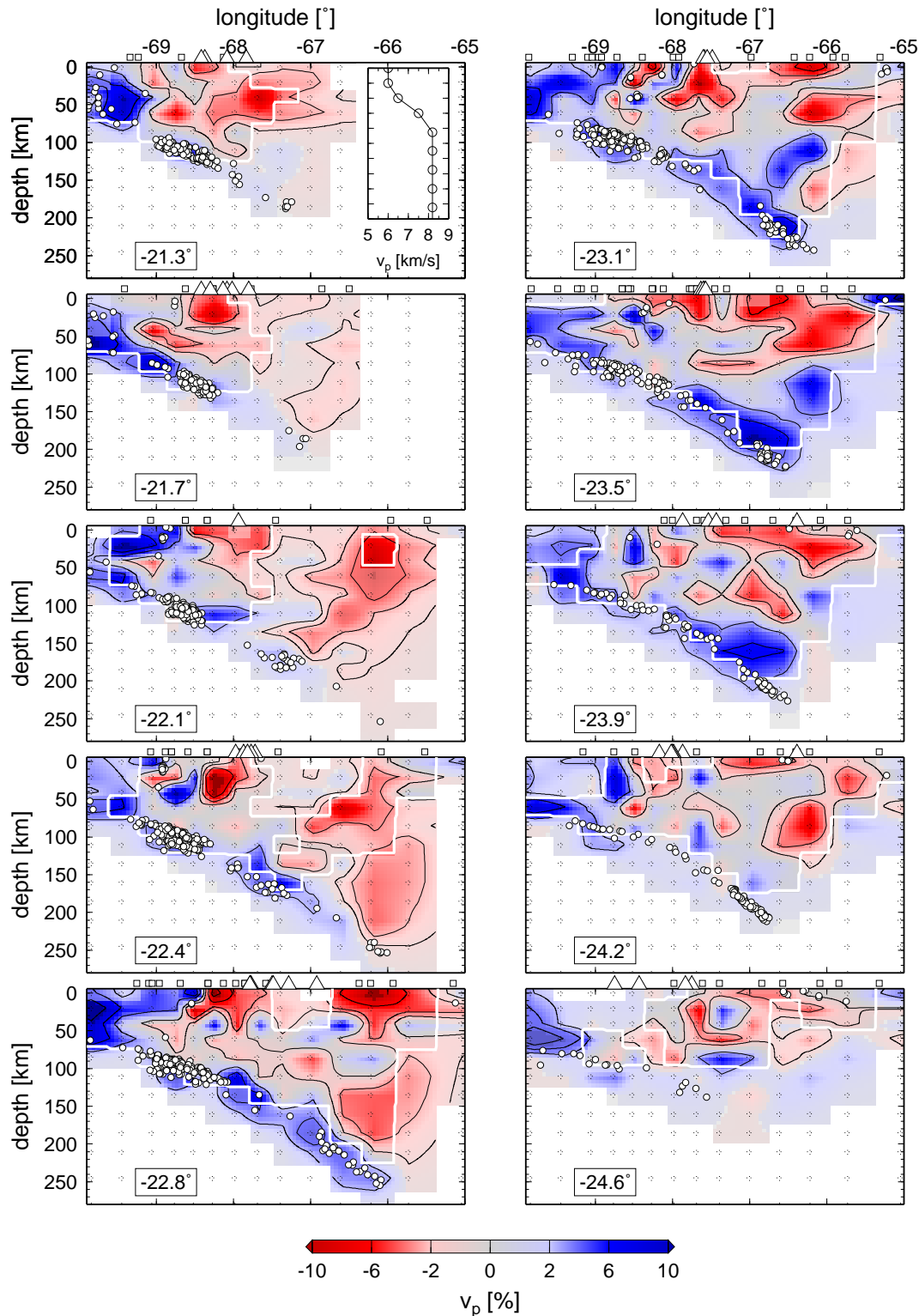
Figure 4.19: West-east depth sections through the 3-D v_p model. Shown are deviations from the 1-D background velocity model that is shown as inset in the first section. Latitude of sections is indicated in the lower left corner. Earthquakes, stations, and volcanoes within 20 km of the section are also plotted. The thick white contour encloses regions of good resolution defined by the spread value. Regions of poor resolution are displayed in slightly faded color.

Figure 4.20: Depth maps of v_p deviations from a background model. Depth is indicated in the upper right corner. The thick white contour encloses regions of good resolution defined by the spread value. Regions of poor resolution are displayed in slightly faded color. The upper left map shows the major morpho-tectonic units (see Figure 2.3 for keys to the units), young volcanoes (white triangles), salt lakes, and seismograph locations (grey squares).

Figure 4.21: West-east depth sections through the 3-D v_p/v_s model. Latitude of sections is indicated in the lower left corner. Earthquakes, stations, and volcanoes within 20 km of the section are also plotted. The thick white contour encloses regions of good resolution defined by the spread value. Regions of poor resolution are displayed in slightly faded color.
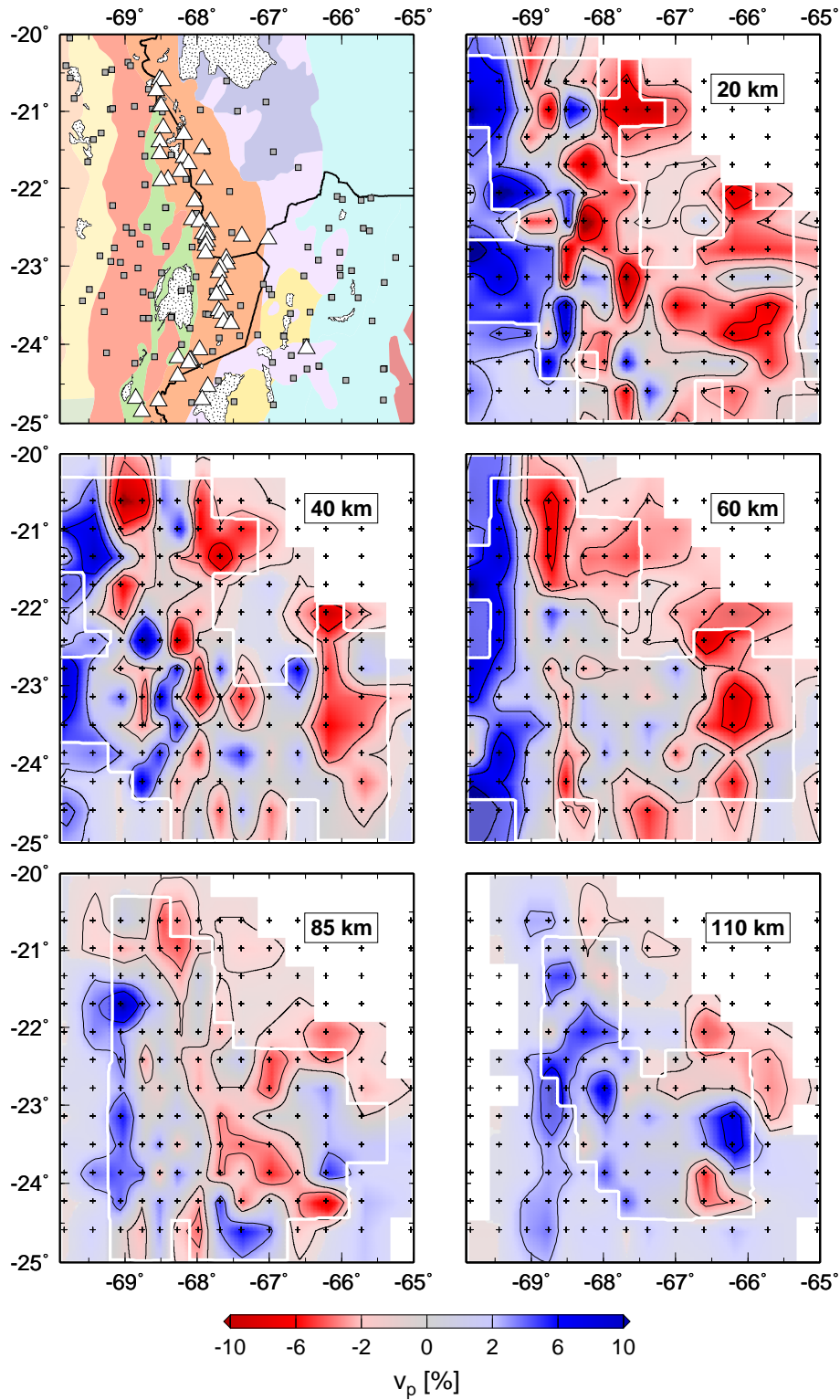
Figure 4.22: Depth maps of v_p/v_s ratio. Depth is indicated in the upper right corner. The thick white contour encloses regions of good resolution defined by the spread value. Regions of poor resolution are displayed in slightly faded color. The upper left map shows the major morpho-tectonic units (see Figure 2.3 for keys to the units), young volcanoes (white triangles), salt lakes, and seismograph locations (grey squares).
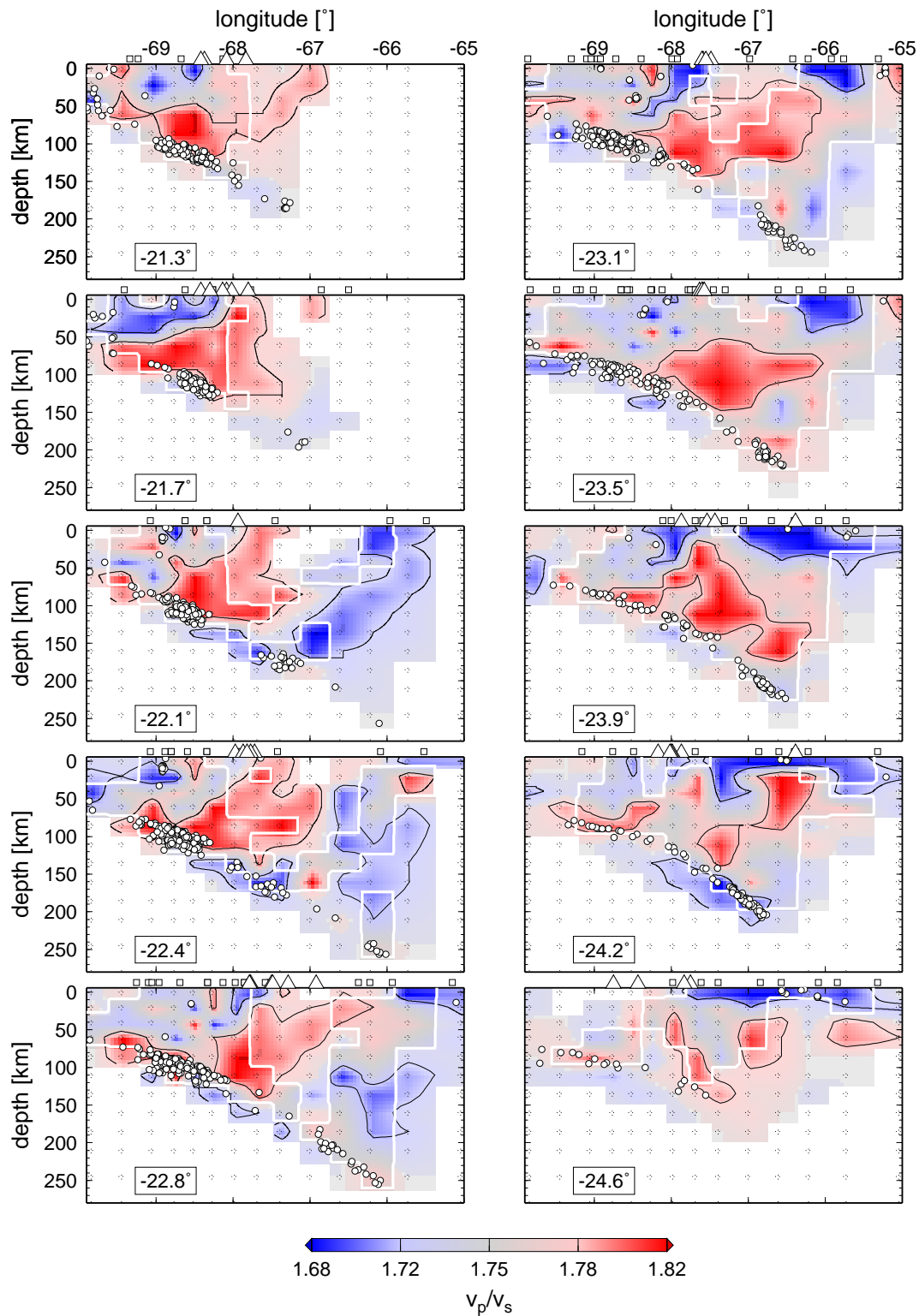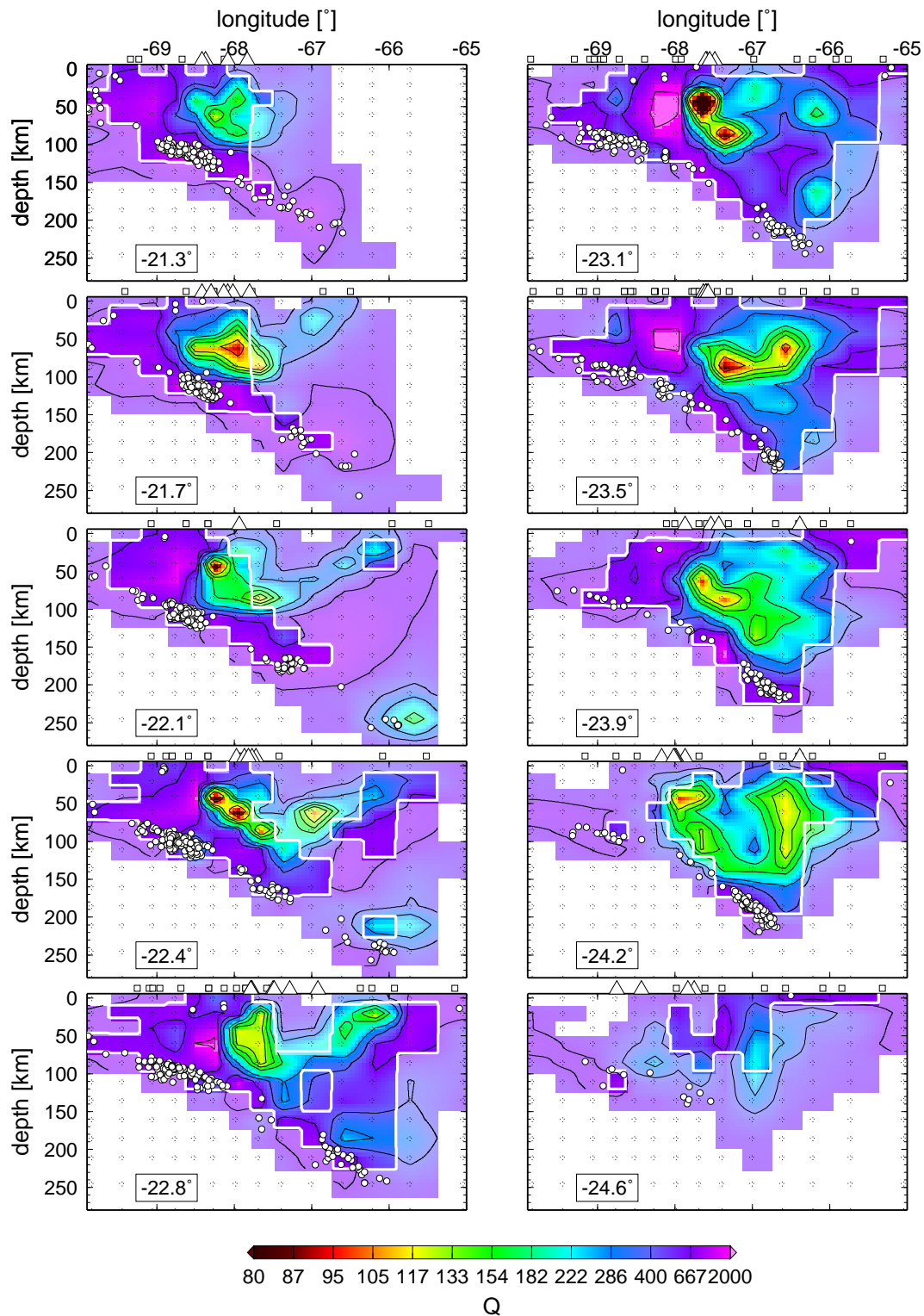
Figure 4.23: West-east depth sections through the 3-D Q_p. Latitude of sections is indicated in the lower left corner. Earthquakes, stations, and volcanoes within 20 km of the section are also plotted. The thick white contour encloses regions of good resolution defined by the spread value. Regions of poor resolution are displayed in slightly faded color.
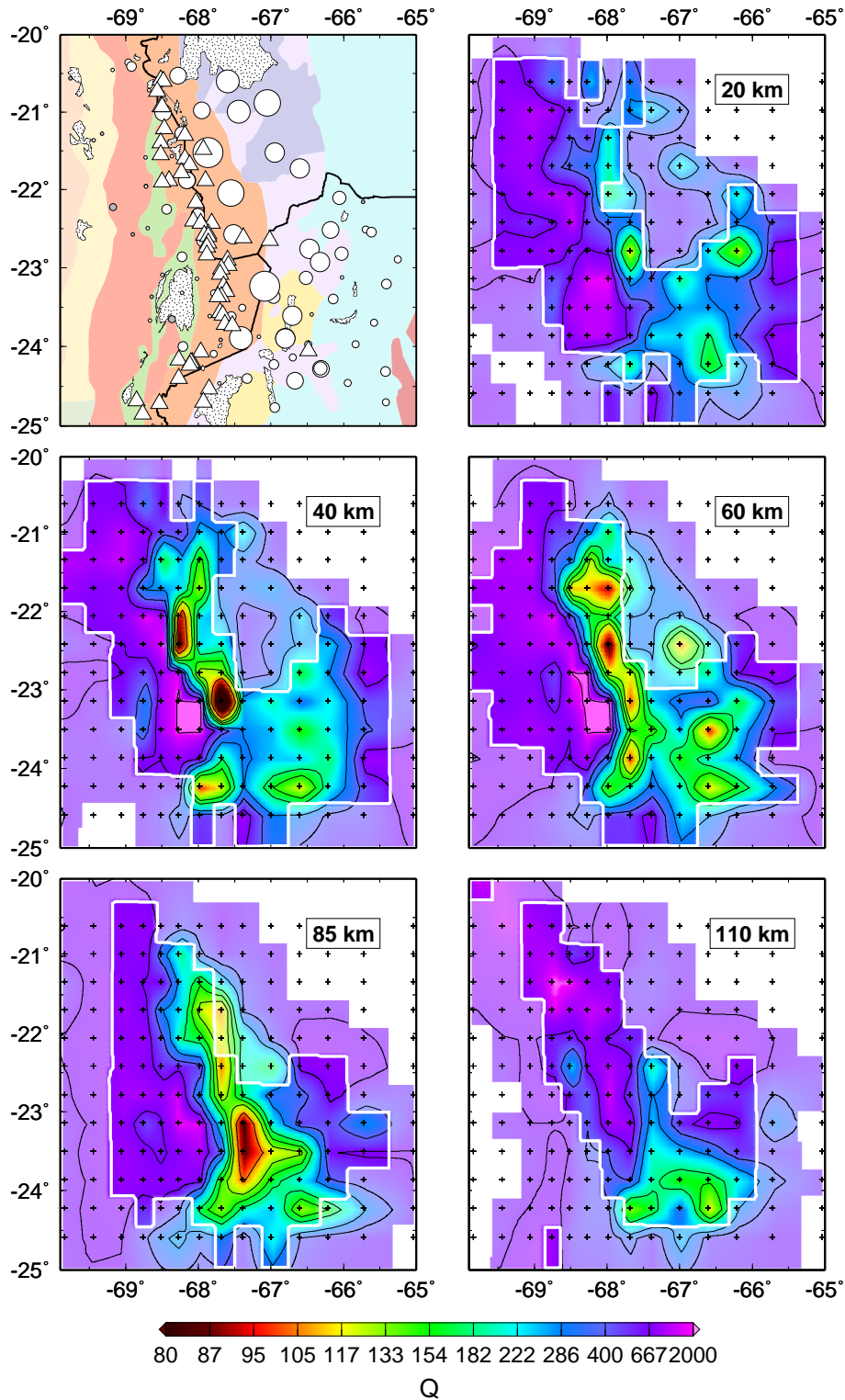
Figure 4.24: Depth maps of Q_p. Depth is indicated in the upper right corner. The thick white contour encloses regions of good resolution defined by the spread value. Regions of poor resolution 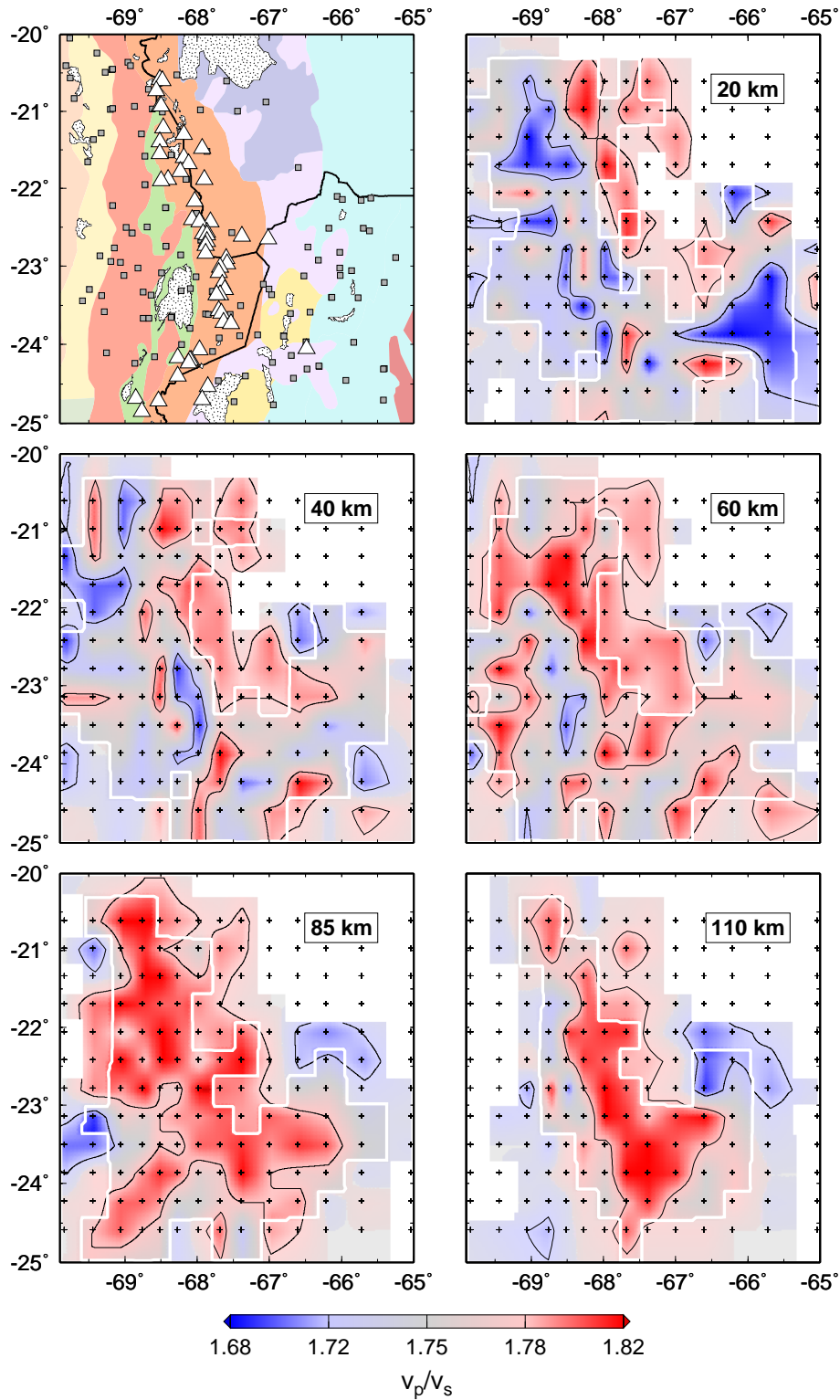are displayed in slightly faded color. The upper left map shows the major morpho-tectonic units (see Figure 2.3 for keys to the units), young volcanoes (white triangles), and salt lakes. The discs show station corrections (white for positive, grey for negative corrections. The large positive station corrections in the backarc (mostly in the regions covered by Holocene volcanics) indicate strong shallow low Q_p anomalies.

and mantle perceptible. A first order morphological anomaly in the study area is the Preandean Depression with the intra-montane basin of the Salar de Atacama, and an eastward shift of the magmatic arc by about 100 km (Figure 2.2). The Atacama basin is underlaid by a block of very high Q_p ($\geq$ 2000), that reaches from the upper crust into the mantle atop the subducted plate. This block is bordered to the west by the Precordilleran fault system, a major north-south striking fault zone, that is imaged by reduced Q_p ($\approx$ 400) and reduced velocity (Figures 4.20 and 4.24) down to more than 50 km depth, and to the east by the Western Cordillera. The transition to the Western Cordillera is very sharp, and occurs essentially from one inversion node to the next (Figures 4.23 and 4.24).

4.6.2   Western Cordillera

The recent magmatic arc forms a prominent anomaly for all three attributes. A crustal low velocity, low Q_p, and elevated v_p/v_s zone closely follows the belt of active volcanoes forming the current magmatic arc (Figures 4.20, 4.24, and 4.22). Q_p appears to be affected strongest by the volcanic processes. The crustal Q_p anomaly is most pronounced in the center of the study area, and dies out to the north and south. Q_p is everywhere below 200, with isolated pockets of 80 and less. The Q_p anomaly correlates with a continuous low v_p zone. v_p is lowest in the upper 20 km (first two rows of nodes). Strongest Q_p anomalies are at 40 km depth, but probably reach the surface, based on the large station corrections. Stronger damping of the station corrections in the inversion places strong Q_p anomalies in the uppermost layers beneath the discrete station locations. The eastern boundary of the magmatic arc is not well defined on the tomographic maps, and low velocities and Q_p reach well into the backarc crust. The strong crustal Q_p anomalies are always connected to the mantle wedge. In the sections north of 22.5°S, low Q_p zones appear to originate directly above the earthquake clusters in 100 km depth. To the south, where the magmatic arc is displaced eastward, mantle anomalies loose connection to the 100 km depth earthquakes. Instead, they reach deeper and eastwards to the 200 km deep seismicity. The high v_p/v_s anomaly described for the forearc also reaches well beneath the magmatic arc. Strongest anomalies are found in the mantle wedge and lower crust. Diminished resolution for v_p/v_s in the shallow crust beneath the Western Cordillera may be responsible for a lack of shallow anomalies.

4.6.3   Slab

The subducted oceanic Nazca lithosphere is imaged as a continuous, fast, high Q_p body dipping eastwards, and enveloping the Wadati-Benioff zone. Velocities are fastest around

23°S near the earthquake cluster in 200 km depth. There, 8.7 km/s are reached but might be overestimated according to the synthetic resolution tests (Chapter 4.4). Q_p in the slab is around 1000, but might be underestimated according to the synthetic tests. v_p/v_s is slightly reduced. Between 23.5°S and 24°S and 150 km and 200 km depth, the slab thickens considerably, and a zone of high velocity material sits above the sharply defined Benioff zone. This section is well resolved and inversion of a synthetic slab does not suggest any artefacts (Chapter 4.4).

4.6.4 Backarc

The backarc crust is characterized by generally reduced crustal velocities (6 km/s – 6.5 km/s) and low Q_p (200 – 300) with isolated stronger anomalies. v_p/v_s is close to normal for felsic rocks ($\approx$1.7) in the uppermost crust (first 20 km). At this depth, additional constraint in some areas (around and south of 24°S) comes from shallow crustal earthquakes. Increased v_p/v_s values are found in the lower crust with a strong anomaly around 24°S, beneath the active backarc volcano Tuzgle. This anomaly extends into the upper mantle and coincides with low Q_p and low v_p. P velocities are extremely low in the upper crust beneath the north-western part of the PUNA network. There, Q_p is also reduced and large station corrections indicate a strong anomaly at shallow depth. Receiver functions show strong negative conversions indicating a LVZ in 20 km depth at these stations [*Yuan et al.*, 2000]. In the lower crust, low v_p and Q_p values are also found beneath the Puna and bordering Eastern Cordillera around 66.5°W in the sections at 23.1°S and 23.5°S. These anomalies extend into the upper mantle and have similar geometries for both parameters. A prominent high-velocity, high-Q_p body, clearly seen in the same sections, dips from the uppermost mantle down to the slab at $\approx$150 km depth. The body is well resolved (Figures 4.9 and 4.11). In the synthetic model, a similar anomaly could be reliably reconstructed (Figures 4.13 and 4.15). Both velocity and Q_p for this anomaly are similar to values found in the subducted slab. All around this high v_p and high Q_p, regions of low velocity and Q_p zone are crouched (Figures 4.19, 4.20, 4.23, and 4.24). There is a pronounced separation in the mantle wedge attenuation structure at around 23°S (see 110 km depth map in Figure 4.24), where to the north mantle Q_p values are normal to high, and to the south, they are low.

North of 22.5°S and east of 68°W, below the Bolivian Altiplano, resolution is too poor to determine reliable velocity and Q_p structure. Synthetic tests and resolution analysis reveal strong smearing along the unevenly distributed ray paths (Chapter 4.4). Additionally, strong trade-off effects between earthquake locations, v_p, and v_p/v_s are expected due to insufficient criss-crossing ray paths. Nonetheless, information about the seismic structure

beneath the Altiplano would be very desirable.

Most data on the Bolivian Altiplano stations come from the energetic earthquake cluster beneath the Chilenian forearc, whereas events directly beneath the Altiplano are rare. To obtain a more balanced ray set for this part of the model, a subset of only the best located forearc events (having ≥ 38 picks) has been selected. In addition, events beneath the Bolivian Altiplano from both the ANCORP and the PUNA experiments, and beneath the northern most PUNA network were included. This yields to a subset of 104 earthquakes that evenly screen the north-eastern part of the model volume (Figure 4.25). The same strategy has been applied for the t^* data; because of a less restrictive azimuthal gap requirement (no necessity for relocation), 276 events are found. These data are used to invert the north-eastern part of the model (north of 23°S and east of 68°W) along an east-west line in two dimensions (Figure 4.25). For the rest of the nodes the 3-D model is kept fixed. The events are also relocated and station corrections are inverted for. The Altiplano nodes to be inverted, were assigned to the previously used starting velocities and starting Q_p values (Chapter 4.5), and earthquakes were relocated within this starting model.

The inversion results are shown in Figure 4.26. The extended low-velocity anomalies seen in the original 3-D model, are now restricted to the crust, whereas mantle velocities are normal. The LVZ at 66°W belongs to the northern most PUNA stations. Beneath the Altiplano (between 68°W and 67°W) there are very low P velocities located in the upper crust. At the same location, high v_p/v_s ratios are found at marginally greater depth, however, S–P times are few for the Bolivian stations, leading to poor depth resolution. Q_p is low for the entire Altiplano crust. Receiver functions from the same area indicate a marked LVZ in 20 km depth [*Chmielowski et al.*, 1999; *Yuan et al.*, 2000], and a magneto-telluric profile across the Altiplano at 21°S is characterized by a prominent high conductivity anomaly between 68.2°S and 66.5°S. Our low v_p, high v_p/v_s, and low Q_p values for the Altiplano crust are in good agreement with these findings.
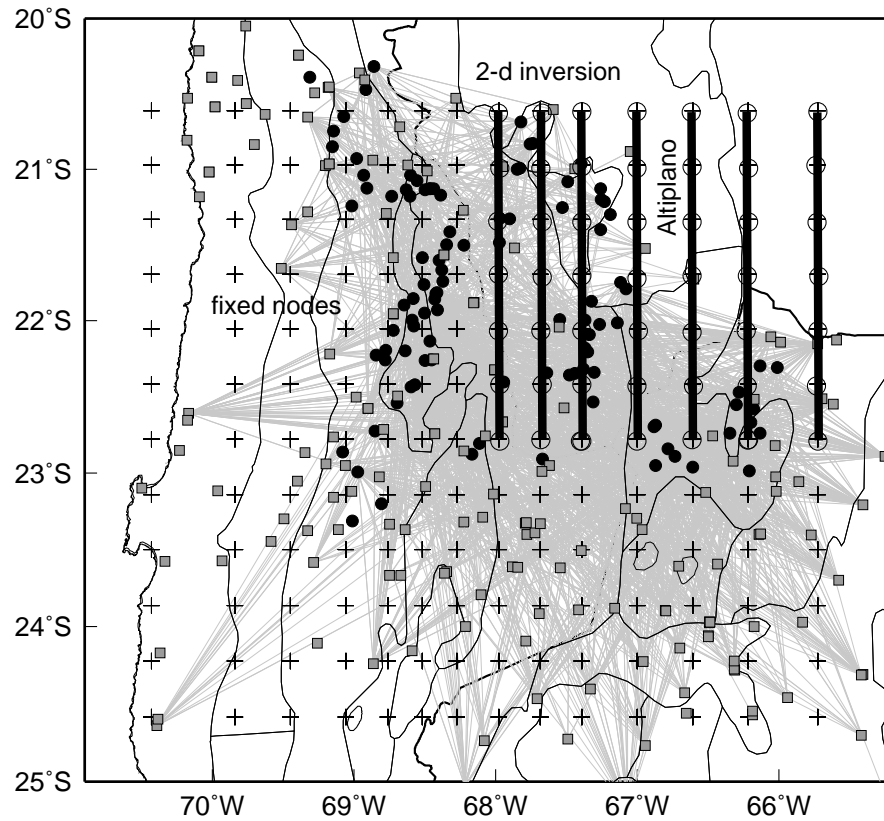
Figure 4.25: Inversion for 2-D structure beneath the Altiplano with a reduced data set. A sub-set of events (black circles) has been selected to produce a balanced ray-set for the northeastern part of the model. There, nodes are linked together in north-south direction to form a 2-D model in east-west direction. Outside this volume, the nodes defining the 3-D model are kept fixed in the inversion.
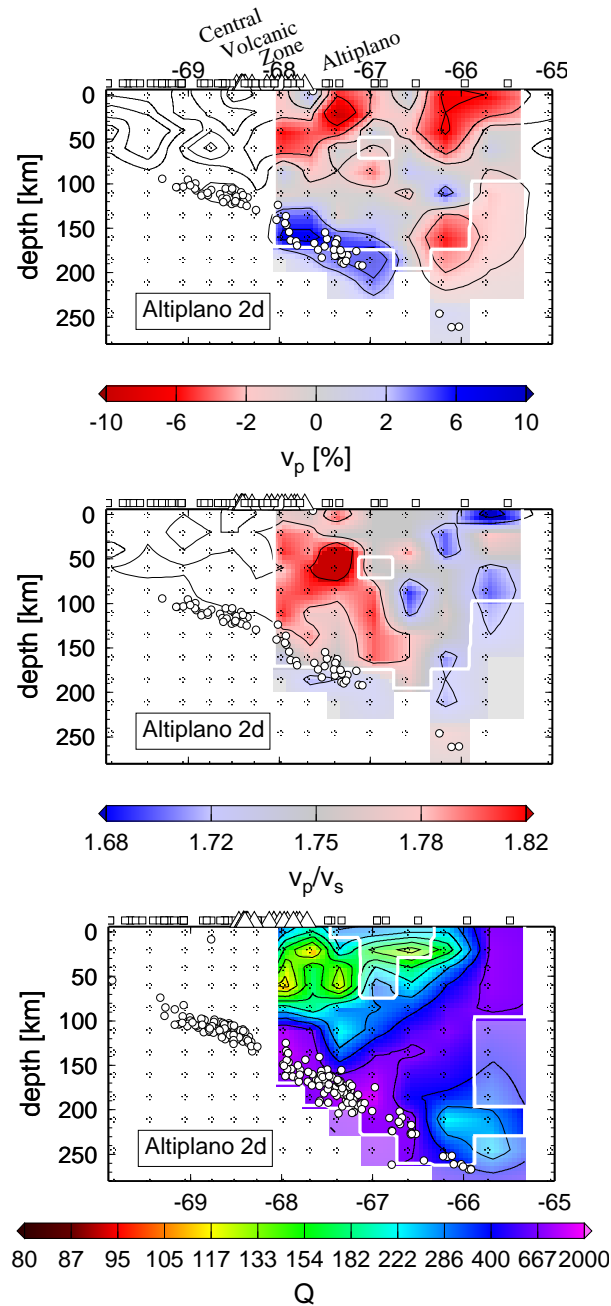
Figure 4.26: 2-D model for the poorly resolved north-eastern part of the 3-D volume. The low v_p zone at 66°W belongs to the northernmost PUNA stations. Beneath the Bolivian Altiplano (68°W–67°W), the crust shows low v_p, high v_p/v_s, and low Q_p values. The mantle shows normal to reduced v_p and Q_p, and elevated v_p/v_s ratios.

4.7   Discussion

The tomographic images of the Andean subduction system and its related orogenic belt reveal a consistent but complex lithosphere-asthenosphere system that is controlled by both, tectonic (e.g. lithospheric shortening) and specific subduction related (e.g. dehydration of the slab and melting in the mantle wedge) processes. On a large scale, elastic and anelastic properties correlate quite well with expectations from simple thermal models of subduction zones [e.g., *Peacock*, 1996], suggesting that homologous temperature[2] is the governing factor for the observed first order patterns.

Subduction zones are cool. Oceanic lithosphere that has been cooled and thickened since the time of its formation [*Parsons & Sclater*, 1977], is subducted with a surface temperature of approximately $0°C$ at rates much faster than thermal diffusion times. Accordingly, it is much cooler than the ambient mantle during most or all of its descent. This temperature difference can be seen as a 6 to 10% positive v_p anomaly that engulfs the Wadati Benioff zone to a depth of 250 km, where resolution allows. The amplitude of the anomaly corresponds quite well with a thermal contrast of 600–800° [*Sobolev et al.*, 1996], as it is expected between a 400–600°C cold slab and a 1000–1200°C hot mantle wedge (see for example the thermal model in *Peacock* [1996], Figure 2A, for a 50 Ma old slab subducted at 10 cm/yr, a situation comparable to the Andes). The low temperatures also cause the low attenuation that is measured for the slab (Q_p=1000–2000). A significant thickening of the slab above the Benioff zone is visible in the v_p sections at -23.5° and -23.9°. Its possible cause will be discussed in Chapter 4.7.3.

Due to continuous subduction of cold oceanic lithosphere, forearcs are also cold. This is manifested, for example, in surface heat flow values that are among the lowest on earth (see *Springer & Förster* [1998] for the Central Andean case). The low temperature forearc is best exemplified by the quite high Q_p values obtained trench-ward of the volcanic front. Intrinsic Q_p is a particularly good gauge for temperature, because it is less sensitive to lithology than v_p and v_p/v_s. The generally high P velocities that also characterize the forearc, might rather indicate a mafic lithology due to its history of migrating volcanic arcs (Chapter 1), although temperature might play an additional role. The mantle wedge beneath the forearc has very high v_p/v_s values ($\geq$1.8, see the 85 km layer in Figure 4.22). These high values have already been noticed by *Graeber & Asch* [1999] and were interpreted as serpentinites that are produced by hydration of peridotite at relatively low temperatures and pressures. Note, however, that there is a region of low v_p/v_s beneath the Atacama depression that will be discussed in Chapter 4.7.1.

---

[2]that is the temperature relative to the solidus. Lowering the solidus temperature, i.e. by adding water, has the same effect on seismic parameters, as raising the absolute temperature.

In the easternmost part of the model, between 65°W and 66°W, the crust, where it is resolved, again shows low attenuation. This, together with relatively low values for v_p/v_s, might indicate the cold, felsic foreland crust that forms the backstop for the Andean orogeny.

Between the seismically strong forearc and foreland, the Andean arc and high plateau is characterized by low Q_p, low v_p, and high v_p/v_s values in crust and mantle. These seismic properties are certainly an expression of subduction related magmatism and crustal shortening that is exemplified at the surface by an active volcanic arc, high heat flow, widespread felsic and mafic volcanism in the backarc, as well as plateau formation. Subduction related anomalies will be discussed in more detail in Chapter 4.7.2, and structures that are associated with lithospheric shortening in Chapter 4.7.3.

Temperature and the presence of water, apart from lithology, are the dominant agents affecting the three seismic attributes v_p, v_p/v_s, and Q_p, investigated in this study. Their effect can be predicted based on experimental data: Raising temperature or adding water reduces v_p and Q_p and raises v_p/v_s. Thus, for the upper mantle, which has a homogeneous mineralogy, there should be correlation or anti-correlation respectively, between the three parameter. In general, this is observed. High and low velocities correlate quite well with high and low Q_p zones, respectively. Regions of low Q_p also correlate with increased v_p/v_s ratios in the hot mantle wedge. However, there are also areas where correlation is not as good. Such discrepancies may be caused by different ray distributions and consequently, different resolution of the three parameters. This certainly affects v_p/v_s, that is based on fewer measurements. Additionally, v_p/v_s estimates are less accurate, because S waves are more difficult to pick, especially if they are strongly attenuated.

Physical effects, like seismic anisotropy, that are not accounted for in the calculations, can also be responsible for deviations from petrologic predictions. In the section at -24.2° , there is a prominent low-Q_p anomaly that extends from slab top towards the base of the arc volcanoes (Figure 4.23). For v_p (Figure 4.19), only the shallow anomaly beneath the Western Cordillera can be seen, whereas values above the slab are neutral or even slightly higher than the background. This can be understood, considering that the mantle above the slab is dragged down due to viscous coupling along with the slab. Such localization of shear induces strong anisotropy in the coupled high viscosity layer. This has recently been evaluated by numerical modeling [*Fisher et al.*, 2000]. Anisotropy affects velocity, but not attenuation. Because of the clustered seismicity at 200 km depth, many of the rays sampling the region above the slab, run sub-parallel in the anisotropic layer along the fast direction. This might explain the absence of a low velocity layer congruent to the observed low-Q_p layer.

Like in a picture-puzzle, deepening into the images reveals countless interesting details,

nonetheless further discussion will be focused on three topics that are relevant to both, the specific evolution and structure of the Central Andes, but also to the understanding of more general processes inside subduction zones.

4.7.1 The Deep Seismic Structure of the Atacama Depression

The Atacama basin constitutes a first order anomaly in the morphology of the western Andes. The depression can be clearly seen as an embayment in the otherwise straight, north-south trending topographic slope and as an eastward deflection of the present volcanic front by some 100 km (Figures 2.2 and 4.27). The Salar de Atacama basin is situated within the Pre-Andean Depression, bounded to the east by the current magmatic arc and to the west by the Cordillera de Domeyko, that is a part of the north-south trending Precordillera (PC).

Some 10 km sediments have been accumulated in the basin since the Permian. The youngest sequence consists mainly of evaporites and claystones, deposited during a marked increase in subsidence (0.7 mm/yr) since Miocene time [*Flint et al.*, 1993]. According to *Flint et al.* [1993], the sedimentary sequence was acquired mainly due to extensional tectonics over the last 250 Ma, while the basin evolved from continental rifting, over an extensional backarc setting, to the present forearc basin setting.

Seismic data from a variety of sources (refraction seismics, tomography, and tele-seismic receiver functions) indicate thick crust ($\geq$60 km) beneath the depression [*Wigger et al.*, 1994; *Graeber & Asch*, 1999; *Yuan et al.*, 2000, this study]. The Atacama region is also characterized by a conspicuous high in the residual gravity field (Figure 4.27). This is unexpected considering the light evaporites and thick sedimentary section comprising the upper 10 km of the crust, as well as the overall crustal thickness [*Götze et al.*, 1994]. The anomaly has been modeled by a high density body between 10 and 20 km depth. The meaning and origin of this body, however, remains elusive. The gravity anomaly can be followed south of the basin crossing the magmatic arc eastwards beneath the Salar de Arizaro in the Argentine Puna.

In the tomographic models of this study, the Atacama basin shows as a prominent anomaly to great depth for the three attributes investigated. Horizontal cross sections at 40 km and 85 km depth from the region are shown in Figure 4.27. For v_p, the sub-basin crust is characterized by a band of fast (6.5–7 km/s) velocities contrasted by the low velocity region underlying the Western Cordillera (WC) to the east and a north-south trending line of low velocities, that might be associated with the Precordilleran fault system, to the west. For v_p/v_s the basin is separated from the elevated ratios underlying the WC by a band of very low v_p/v_s ratios in the crust (Figure 4.27). Latter anomaly can be traced
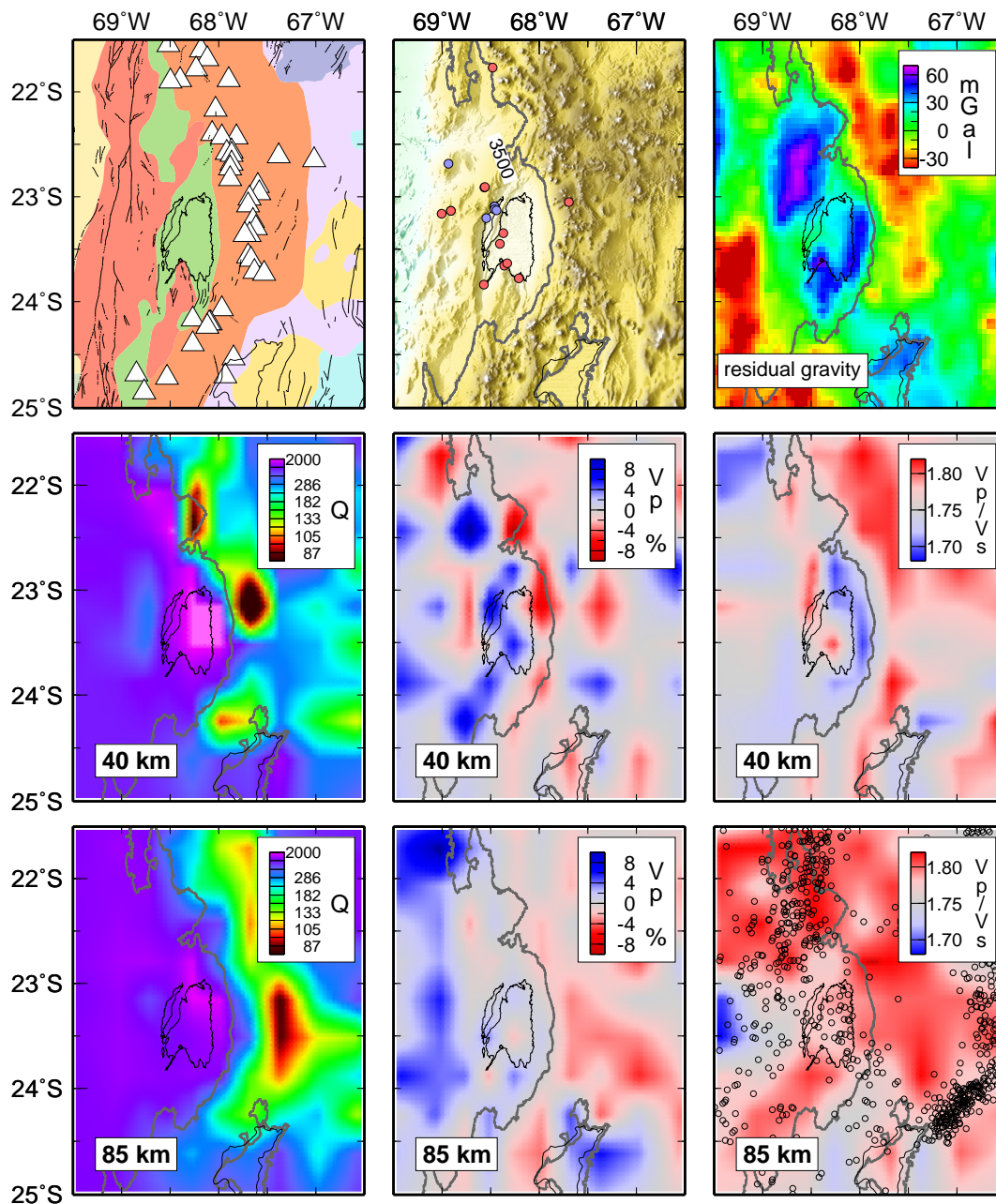
Figure 4.27: Upper row. Left: Morpho-tectonic units and fault data after *Reutter & Götze* [1994]. See Figure 2.3 for key. White triangles mark active volcanoes. Middle: Topography. Salar de Atacama (in the center) and Salar de Arizaro (in the south east), as well as the 3500 m elevation contour line is drawn here and on all subsequent maps for orientation. Circles mark crustal earthquakes from the local catalog of this study, red: depth $\leq$ 20 km, blue $\geq$ 20 km. Right: Isostatic residual gravity from *Götze et al.* [1994]. Note the prominent high around Salar de Atacama and the gap in the low beneath the WC between the Salar de Atacama and Salar de Arizaro. **Middle Row**: Horizontal sections at 40 km depth through the tomographic model for Q_p, v_p, and v_p/v_s. **Lower row**: Same as above at a depth of 85 km (uppermost mantle). For v_p/v_s, historic Benioff seismicity from a global catalog [*Engdahl et al.*, 1998] is plotted. Note the diminished seismicity in the forearc part of the slab south of 23°S .

all the way into the mantle (see 85 km layer in Figure 4.27), where the very high ratios measured north of the basin, probably indicating serpentinites [*Graeber & Asch*, 1999], diminish towards normal values below the Atacama basin (Figure 4.27). The lithosphere underlying the Atacama depression also shows the highest Q_p values measured (≥ 2000). The high Q_p zone reaches all the way down to the subducted slab. It is sharply bounded by the extreme low values outlining the WC and by moderately reduced values beneath the PC, that are probably also associated with Precordilleran fault system. We also note, that where the gravity high crosses the WC, at around 24°S , there is a gap in the otherwise continuous low Q_p and high v_p/v_s ratios beneath the WC, probably indicating absence of partial melts in the crust. High Q_p values and low v_p/v_s are also found beneath the Salar de Arizaro, although this is at the fringe of the resolved area.

All of this characterizes the lithosphere underlying the Atacama basin as a cold, very strong block, from here on termed Atacama block, that is clearly discriminated from neighboring rocks by its state or lithology. The strong rheology is supported by unusually deep crustal seismicity (up to 40 km deep) beneath the north-western edge of Salar de Atacama (Figures 4.27 and 4.28).

The Q_p images also suggest that this block significantly influences the asthenospheric flow and feeding of the arc volcanoes (see Chapter 4.7.2). It appears to displace hot isotherms eastward and to keep asthenospheric mantle from penetrating deeper into the wedge corner. This is why arc volcanoes were not emplaced along the same trend as to the north and south of the basin, but displaced to the east, just off the cold Atacama block. Consequently, the Atacama basin did not evolve inside an embayment of the Cordillera, but in contrary, the formation of the arc was pushed eastward by the presence of the Atacama block. It is also interesting that the magmas for the displaced arc volcanoes come from the backarc side out of a source region at 200 km depth, whereas to the north, the magma source is at 100 km depth on the forearc side. This is a consequence of the presumably very low temperatures in the mantle sliver beneath the Atacama depression. Although there is seismicity, and thus metamorphic fluid expulsion from the slab on the forearc side at 100 km depth, no melting and magmatism is produced because temperatures are too low.

It is interesting to note that in the early Miocene, just when the arc was build on its present location, a magmatic gap occurred between 22°S and 24°S, the exact extent of the Atacama depression [*Allmendinger et al.*, 1997]. This was interpreted as a spatially and temporarily limited section of flat subduction, that, however, had some important consequences in the development of geodynamic models [*Isacks*, 1988] (e.g. it was assumed that the subsequent steepening of this section may have caused the ignimbrite flare up on the plateau). An alternative explanation of the magmatic gap in the early stage of the

magmatic activity of the WC in view of this results might simply be, that, because the generic magma ascent ways were barred by the Atacama block, it took additional time to establish alternative ways in the backarc further east.

It can be expected that the presence of the Atacama block also influences the thermal structure of the slab, because it serves as a insulating lid and delays contact to hot asthenosphere. As metamorphic reactions inside the oceanic lithosphere strongly depend on temperature, this could explain why the band of extremely high seismicity observed at around 100 km depth, diminishes south of 23°S[3] (Figure 4.27). Nevertheless, we add the caveat that it is not known if the presently observed seismicity patterns are persistent in time. It would explain, however, that v_p/v_s ratios in the mantle wedge are much lower beneath the Atacama block than north of it, because if metamorphism would be delayed, less H_2O would be released into the mantle, and consequently, peridotites would be less hydrated.

The origin of the Atacama block is unclear. It was stationary during at least the Andean orogeny, and considering the sedimentary record probably since upper Paleozoic time. *Götze et al.* [1994] speculate that large amounts of basic intrusives from an Ordovician subduction zone might be responsible for the gravity anomaly. Our seismic data characterizes the crustal rocks as relatively fast, but with low v_p/v_s ratios. This requires rocks of intermediate composition at low temperature and high pressure [*Sobolev & Babeyko*, 1994]. *Lucassen et al.* [1999] investigated high-pressure, low-temperature rocks that crop out in the Sierra de Limón Verde, at the north-western boundary of the depression. They were metamorphized at 45 km depth in the Permian and uplifted during the Triassic. The authors suggest that these lower crustal rocks at a shallow level could cause the measured gravity high. The rocks are dominantly quartz-rich gneiss with fewer metabasites interlaced. We calculated v_p and v_p/v_s ratios for the published mineral assemblages at the pressure and temperature of their equilibration [*Sobolev & Babeyko*, 1994]. Either of the rocks alone cannot explain our observations. The gneisses would have too low velocities and too low densities. The metabasites are too fast and have too high v_p/v_s ratios. An even mixture of both, however, would be in accordance with the seismic data.

The high pressure rocks from the nearby Sierra de Limón Verde indicate that in Permian time the crust was already at least 45 km thick and it definitely has thickened since then. The seismic attributes characterize the Atacama block as cold and strong. These features are hard to reconcile with a long history of crustal extension that should be accompanied by crustal thinning. Yet the basin definitely has been subsiding. How can

---

[3]This is best observed on global catalogs, because the catalog used in tomographic inversion, was specifically selected for an even distribution of earthquakes, and as such does not necessarily represent the real spatial distribution of seismicity.

it be subsiding without extending the crust? The Atacama block is surrounded by zones of weakness: The, on a crustal scale, soft volcanic arc to the north, south, and east, and the Precordilleran fault system to the west. It could be speculated that the block rests on top of the subducted slab and subsides as a whole, like a piston in a cylinder, due to basal erosion by the subducting slab (Figure 4.28). This would be in accordance with the accelerated subsidence since the last 10 Ma, the time frame in which the present-day subduction geometry is in place.
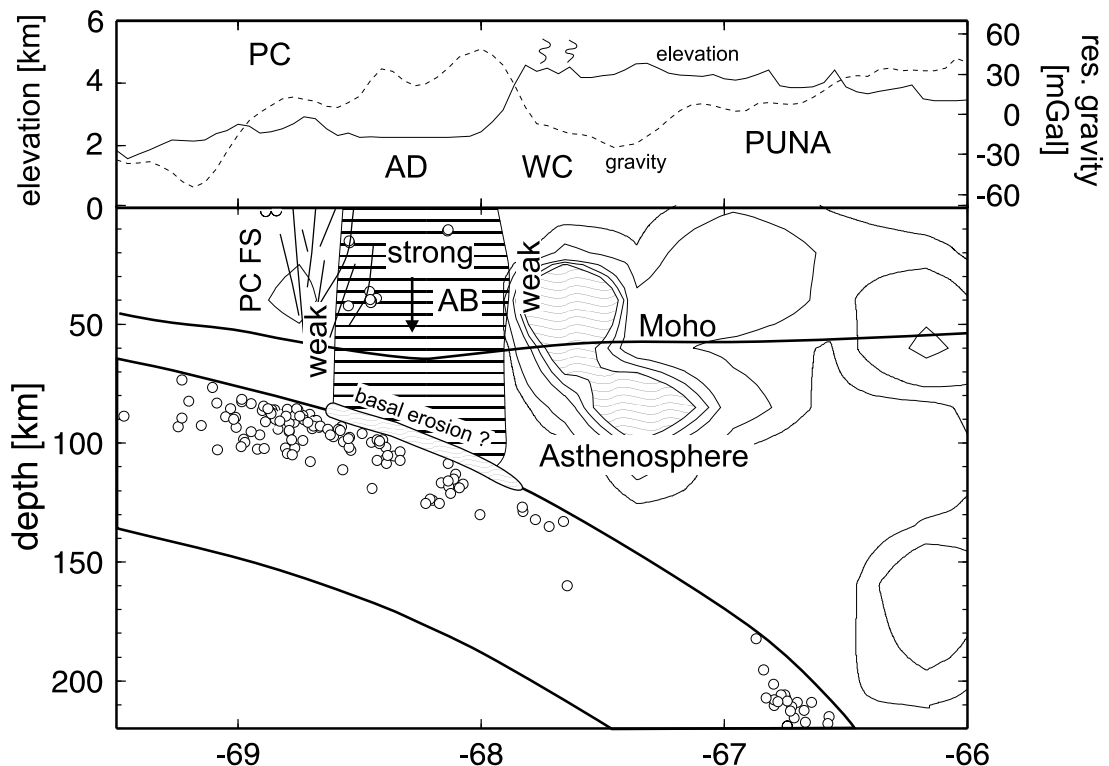

Figure 4.28: Topography, residual gravity, and interpretational cross section through the Atacama region at 23.2°S. Abbreviations are as follows: PC – Precordillera, PCFS – Precordilleran fault system, AD – Atacama depression, AB – Atacama block, WC – Western Cordillera. Thin isolines are taken from the Q_p model. Shaded part has very low Q_p values probably indicating partial melts. Moho depths are taken from a 3-D map from receiver functions (*Yuan*, personal communication). Circles are earthquakes. Fault line for the PCFS are not mapped, but sketched into a region of relatively low velocities and low Q_p. The Atacama block is seismically strong, that is high Q_p, high v_p, and low v_p/v_s. It is surrounded by relatively weak zones (low Q_p, low velocities): the PCFS to the west, and asthenosphere and probably hot or partially molten crust beneath the WC to the east. The AB obstructs asthenosphere from penetrating trench-wards into the mantle wedge and thus displaces the volcanic front to the east. There is no indication of extension and crustal thinning inside the AB, in contrary, despite its low elevation, crust is very thick. It is proposed that the AB subsides as whole along the surrounding zones of weakness. Subsidence may be caused by lithospheric erosion at the slab-mantle interface.

4.7.2 Source Regions and Ascent Paths of Fluids in the Subduction Zone of the Central Andes

It is now widely agreed, that water released from the subducting oceanic lithosphere triggers partial melting in the overlying mantle wedge, providing the source for andesitic volcanism that is ubiquitous in almost all subduction zones [*Gill*, 1981]. Yet, the questions of where dehydration occurs, where and how fluids leave the slab, and how they are transported through the mantle wedge are still debated. In almost all sketches of subduction zones in present-day tectonic text books, the sources of lavas erupting at the volcanic arc, are assumed to originate atop the subducted slab directly beneath the volcanoes. Transport is either drawn as ascending blobs of magma or simple, thin, vertical channels. Both of these assumptions are made because better knowledge is lacking. Geochemical tracers are not sensitive enough to precisely locate the source of aqueous volatiles and magmas in the mantle wedge. Seismic tomography has the potential to do so, because fluids (aqueous fluids as well as melts) significantly alter the elastic and anelastic properties of rocks, yet resolution of existing models has not been sufficient.

As sediments, oceanic crust, and oceanic mantle are subducted to greater pressure and temperature, they undergo various metamorphic transformations which release substantial amounts of H_2O [*Peacock*, 1996]. At shallow depths (≤ 20 km) pore water is expelled by compaction. Bound water is released during breakdown of hydrous minerals at greater depths. The most important H_2O liberating reaction in oceanic crust is the transformation of blueschist to eclogite. Dehydration rates are highest until the breakdown of amphibole that occurs almost isobaric at pressures of 2.3–2.5 GPa (70–80 km depth). This major fluid pulse at constant depth, together with some lateral transport mechanism in the mantle, has been employed to explain the globally similar vertical separation of the volcanic front from the Wadati-Benioff zone of approximately 120 km [*Gill*, 1981; *Davies & Stevenson*, 1992]. Alternatively, *Tatsumi* [1989] suggested that a hydrated peridotitic layer above the slab is dragged down by viscous coupling along with the slab to higher PT regions. Here, amphibole and chlorite decompose and release water at ≈ 110 km and phlogopite at ≈ 200 km depth, in accordance with depths of the Benioff zones beneath volcanic fronts and the existence of secondary volcanic chains in some backarcs.

More recent work, however, showed that discrete pulses of water at certain depths are unrealistic. The amphibole-out reaction does not completely dehydrate the slab, and the retaining 2 wt% of H_2O are released in continuous reactions to depths greater than 200 km [*Poli & Schmidt*, 1995; *Schmidt & Poli*, 1998]. Hydrous phases in the oceanic mantle may constitute an additional source of H_2O, as they have been shown to be stable to depths greatly exceeding the amphibole-out reaction [*Ulmer & Trommsdorff*, 1995;

Schmidt & Poli, 1998]. There is seismic evidence from dispersed body wave phases that a low velocity waveguide, interpreted as hydrated oceanic crust, persists to depths greater than 200 km in many subduction zones [*Abers*, 2000]. Such guided and dispersed waves, although not investigated in detail here, are also observed from many of the intermediate depth (100–250 km) earthquakes of this data set. All of this suggests that there could be a continuous supply of aqueous fluids from the subducted slab from beneath the forearc, across the arc, and into the backarc to depths greater than 200 km.

Intermediate depth seismicity is also considered a phenomena related to dehydration processes in the slab. Water released by metamorphic reactions is thought to reduce the effective stress, thus allowing brittle failure at pressures and temperatures where rocks would otherwise be subject only to ductile deformation (dehydration embrittlement) [*Raleigh*, 1967; *Green & Houston*, 1995; *Kirby et al.*, 1996]. *Kirby et al.* [1996] recognize a peak in intermediate depth seismicity at a similar depth as the global average of Benioff zones beneath volcanic fronts (approximately 110 km depth). From this coincidence they suggest that the focus of crustal metamorphism, that is expressed in seismicity, is at the roots of arc volcanism. *Wiemer & Benoit* [1996] investigated the frequency-magnitude relation (b-value) as a function of depth in the Alaskan and New Zealand subduction zones. Anomalously high b-values were found around 100 km depth, roughly beneath arc volcanoes. The anomalies were also interpreted as due to high pore pressures caused by dehydration reactions. In our study area, the vertical separation of the volcanic front from the Benioff zone is between 120 and 140 km (Figure 2.2), whereas distinct clusters of seismicity occur at 90–110 km depth and 190–250 km depth, defying such a simple connection.

Several reasons make us believe that low Q_p anomalies are mainly due to intrinsic anelasticity of rocks, rather than scattering. Q_p anomalies correlate quite well with v_p and v_p/v_s anomalies, as it is expected for intrinsic Q. Seismograms from stations above the highly attenuating WC and Puna plateau show simple low-frequency P pulses with very little coda and S waves that are extremely attenuated or even absent (see Figure 4.8). This would not be expected if scattering was the dominating reason for energy loss. Instead energy would displaced into the P and S coda, which is not observed.

At sub-solidus, intrinsic Q is a linear function of homologous temperature, that is the temperature relative to the solidus. Water substantially reduces the melting temperature of peridotite [*Kawamoto & Holloway*, 1997] and thus greatly amplifies seismic attenuation (Q^{-1}). Thus adding water to rock has the same effect on seismic Q as raising the absolute temperature.

The intriguing feature in many of the presented cross sections for Q_p (Figure 4.23) is that the strong low-Q_p anomalies that cross the mantle wedge and penetrate the crust

at the base of arc volcanoes, appear to originate at the distinct earthquake clusters in 100 or 200 km depth. It is very suggestive that these anomalies are due to H_2O fluxed into the mantle wedge by earthquakes, reducing the solidus, and probably subsequently inducing partial melting. The only alternative explanation would be that shear heating generated by the ruptures would raise mantle temperature and cause partial melting in the overlying rocks. Considering the small seismic moments of the events, this seems not a viable option.

This has several important consequences. *Bock et al.* [2000], using converted phases from this same data set, showed that the intermediate depth earthquakes are located in the subducted oceanic crust or underlying oceanic mantle. This rules out *Tatsumi* [1989]'s model, in which fluids are released from a hydrated peridotitic layer above the subducted slab. It further implicates, that either dehydration is accompanied by seismicity, that is, if there is no seismicity, there is no fluid production, or, that, although fluid production in the subducted slab may be a continuous process, fluid transfer from the slab to the mantle occurs at discrete locations due to earthquakes.

It is not understood by what transport mechanism hydrous fluids leave the slab. It has been suggested that porous flow is unlikely because dihedral angles are probably $\geq 60°$ for minerals in the oceanic crust [*Watson & Lupulescu*, 1993], although the experiments were not done at high enough pressures. Thus water may not interconnect along grain boundaries, but might be trapped in isolated pores, unable to percolate. *Davies* [1999] proposed that hydro-fracturing triggered by intermediate depth earthquakes transports water into the mantle wedge. Non-percolating water freed by metamorphism provides the high pore pressure necessary for faulting. Rupture will temporarily interconnect pore space, and when a sufficiently high water column is interconnected, a hydro-fracture is produced on the upper end of the fault, conveying water into the mantle. Such a model would be in accordance with our observations.

Once water enters the mantle wedge, it will ascent and flux melting where the wet solidus of peridotite is exceeded. The low Q_p anomalies probably represent the ascent paths and source regions of fluids and partial melts. It should be kept in mind however, that the anomalies due to volatiles and melts are overprinted by possible variations of absolute temperature due to a heterogeneous lithosphere/asthenosphere structure and asthenospheric flow.

In the sections north of 22.5°S, the low Q_p anomalies appear to originate at the prominent earthquake cluster in 100 km depth [*Haberland & Rietbrock*, 2000]. From there the ascent is straight up, or with a considerable lateral westward component in some sections, to the base of the arc volcanoes (Figure 4.23). Further south, the volcanic arc is displaced about 100 km to the east by the Atacama depression. The lithosphere underlying the Atacama

basin is characterized by a prominent high Q_p, reduced v_p/v_s, high v_p anomaly to great depth (Figures 4.23, 4.21, and 4.19). The origin of this anomaly has been discussed in Chapter 4.7.1 in more detail. Its seismic properties make it a deep reaching, very cold and strong block that obstructs the advancement of asthenospheric mantle into the wedge corner and also appears to significantly deviate transportation patterns of volatiles and melts. Q_p anomalies emerge where volatiles meet hot mantle. The arc volcanoes east of this block (south of 22.5°S) lose connection to the 100 km cluster beneath the forearc, but instead appear to be fed from the deeper cluster to the east. These images clearly demonstrate that the often implicitly assumed transport paths of magmas straight up to the base of the volcanic front are not adequate. Our results indicate that the ways volatiles and magmas move through the mantle wedge can be quite complicated, and that large lateral distances are covered. An especially good example is the section at 24.2°S (Figures 4.23 and 4.29). Here the arc volcanoes and the backarc volcano Cerro Tuzgle, located 200 km east of the volcanic front appear to have the same source in 200 km depth. For Cerro Tuzgle the ascent is straight up, whereas magmas feeding the arc volcanoes appear to be transported backward along the slab to the base of the crust and then up to a crustal magma chamber.

Different mechanisms for transport of aqueous fluids and melts in the mantle wedge have been proposed: porous flow along grain boundaries, buoyancy driven crack propagation, and diapiric ascent. It has been argued against large diapirs rising in the mantle wedge because ascent is so slow that batches of melt would solidify before reaching the crust [*Clemens & Mawer*, 1992]. There is also geochemical evidence from U-series disequilibria of young lavas, indicating rapid transport of aqueous fluids to the source region (≤40,000 yr), and rapid transport of melts to the surface (≤8000 yr) [*Elliott et al.*, 1997]. These short time-scales argue for the faster permeable flow or crack propagation as modes of fluid transport.

It has been shown that wetting of mantle-mineral grain boundaries might be complete (dihedral angles ≤60°) at pressures and temperatures of the mantle wedge [*Mibe et al.*, 1999], thus principally allowing porous flow of H_2O in the mantle. *Iwamori* [1998] developed a numerical model for permeable flow and melt generation in the mantle wedge. In his results H_2O released from a down-dragged serpentine and chlorite layer (similar to *Tatsumi* [1989]'s model) rises straight up to the melt source. Melts are then transported horizontally trench-ward by the corner flow to the base of the volcanic arc. Such a geometry does not agree with our images. Yet, models of permeable flow that include deformation of the matrix may produce more complex flow fields [*Spiegelman*, 1993], better matching our results.

Propagation of isolated fluid-filled fractures is the third proposed mode of transport for

aqueous fluids and magmas. There is evidence from Alpine eclogite facies rocks for fracturing and flow through fractures to depths of 70 km [e.g., *Hoogerduijn & Vissers*, 1992]. Propagation of fluid-filled fractures is controlled by apparent buoyancy forces, directions of principal stresses, and tectonic stress gradients. *Dahm* [2000] modeled propagation of fluid-filled fractures in a subduction environment. The stress field was calculated for a stationary corner flow model, thus depending on slab dip, subduction velocity and mantle viscosity. Due to the deviatoric stresses, fractures propagate significant horizontal distances away from the wedge corner, similar to the paths found in the northern sections of our model. For steeper dips ($\geq 45°$), ascent paths can be upwards or towards and along the slab, resembling the ones we observe for the deeper cluster. It should be noted, however, that although the slab beneath the Andes steepens with depth, subduction angle is only about 35° at 200 km depth. The real stress field in the mantle wedge is probably more complex than simulated by the corner flow model, this is especially true for the compressive environment of the Andes. Additionally, variations in viscosity and interaction of the fluids with mantle material may render things more complicated in the real earth. It is also debatable if arrays of isolated fluid filled cracks can cause the large continuous anomalies we observe.

Certainly, more data from high pressure experiments and numerical modeling are required for a better understanding and interpretation of these observations.

Last, it is pointed out that strong low Q_p, low v_p anomalies are found in the uppermost mantle layer (85 km depth). This indicates that ponding and transitional storage of magma takes place at the base of the crust as has been suggested by equilibrium pressures of arc magmas and numerical model calculations [*Laube & Springer*, 1998]. Further ascent of magmas may be hindered by viscous, density, or lithologic contrasts. Mantle derived magmas at the base of the crust might also induce melting of crustal rocks responsible for the felsic volcanism widespread on the Andean Plateau.
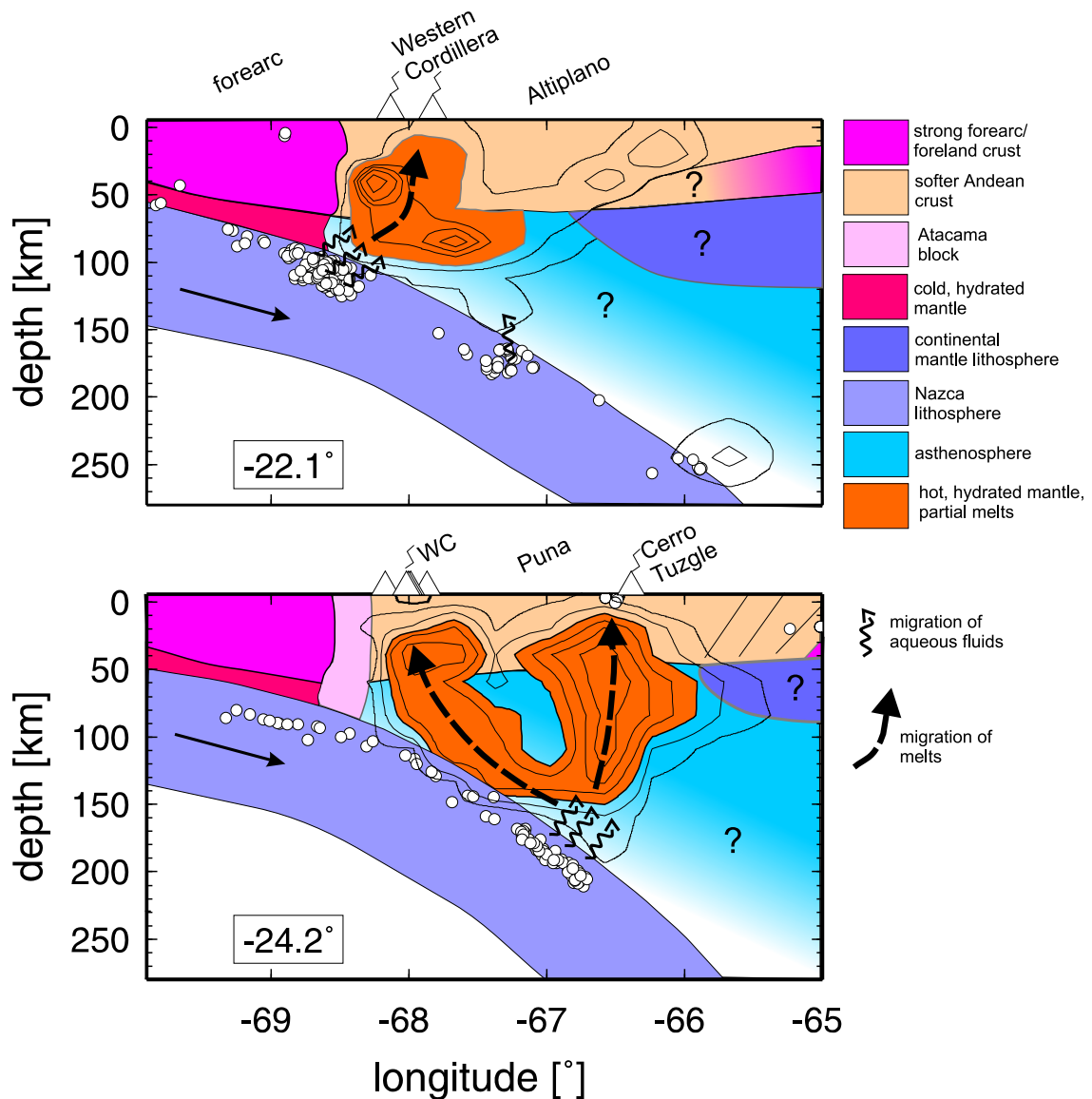
Figure 4.29: Interpretations of the cross sections for Q_p at 22.1°S and 24.2°S (Figure 4.23). H_2O is released from the slab at the discrete earthquake clusters, maybe through hydrofracturing triggered by faulting (see text for more details). H_2O causes flux melting in the overlying hot mantle wedge. Regions of $Q_p \leq 200$ are colored in orange. Here, mantle and crustal rocks probably contain significant amounts of partial melt. Melt ascent ways are not straight up as is often implicitly assumed, but have a significant horizontal component. The paths of magmas vary probably due to their source locations, deviatoric tectonic stresses, and asthenospheric flow. The mechanism responsible for transport of magmas through the mantle wedge is not well understood. See text for discussion.

4.7.3   Lithospheric Delamination beneath the northern Puna

One of the most intriguing questions in geodynamics is the role of the mantle lithosphere in collisional mountain building. Crustal shortening has been found the dominant mechanism in formation of thick crust and uplift of continental high plateaus. It is obvious that if crustal shortening occurs, the underlying mantle lithosphere must deform and thicken too. Surprisingly, unusually thin lithosphere is often found beneath plateaus (e.g. beneath northern Tibet and the southern Puna). The concept of lithospheric delamination has been introduced in the eighties to explain the absence of a thick mantle lid beneath elevated plateaus [e.g., *Bird*, 1979; *Houseman et al.*, 1981] and rapid uplift and mafic magmatism often accompanying the late stage of the orogenic process [*Kay & Kay*, 1993]. In this model thickened, cold lithosphere becomes gravitationally unstable, delaminates from the lower crust, and sinks into the underlying mantle. The missing lithosphere is replaced by an influx of hot asthenosphere causing uplift of the crust and volcanism. Although lithospheric delamination has been proposed in many locations (the Himalayas, Andes, Alps, the Basin and Range province of the Western United States, the European Variscides) based on its symptoms, the process has only been observed geophysically in Tibet [*Kosarev et al.*, 1999]. This may be due to its ephemeral nature: numerical modeling indicates that lithospheric delamination and detachment is a catastrophic event that lasts only a few million years [*Houseman et al.*, 1981; *Schott & Schmeling*, 1998].

Between 23°S and 24°S in the northern Puna of the Central Andes, we image a fast, high Q_p body that dips from the base of the easternmost Puna crust 100 km down to the subducted Nazca plate (Figure 4.30). South of this body the mantle wedge has low velocity and Q, and the Nazca plate thickens by several tens of kilometer above the sharply defined Benioff zone. This region of mantle wedge and slab is well resolved, and synthetic tests show that both the slab and structures in the mantle wedge can be retrieved quite accurately (Chapter 4.4). Anomalies in velocity and attenuation have to a first degree the same physical cause: variations in homologous temperature, that is the temperature relative to the solidus temperature [*Berckhemer et al.*, 1982; *Jackson et al.*, 1992]. Because velocity and Q_p images are based on independent measurements (travel times and spectral shapes), their congruence gives additional confidence in the results. The fast, high-Q_p region appears sharper in the velocity image. This may be caused by the non-linear resolution of Q_p, making variations in high-Q_p regions more difficult to resolve than variations for low Q_p. Above the high-v_p, high-Q_p region in the mantle, high attenuation and low velocities are found in the uppermost mantle and lower crust. Adjacent highs and lows in tomographic models have to be considered carefully because they could be an artefact. We verified that the structures in crust and mantle are decoupled by inverting only for mantle structure while fixing a homogeneous crustal
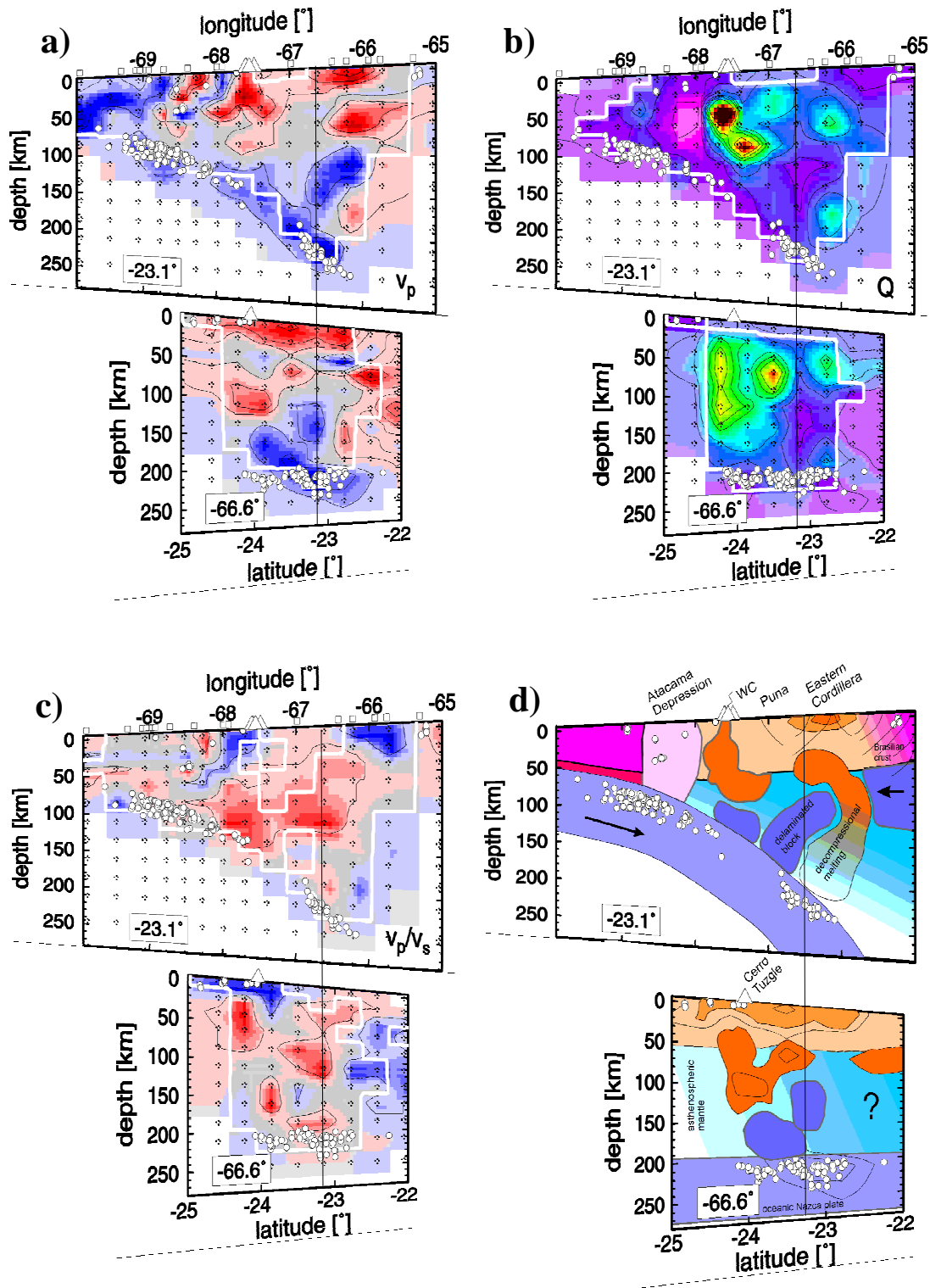
Figure 4.30: Latitudinal (23.1°S) and longitudinal (66.6°W) cross sections for a) v_p, b) Q_p, and c) v_p/v_s through the model volume. d) Interpretational sketch for the same sections. The fast, high Q_p region is interpreted as detached South American lithosphere. The apparent thickening of the Nazca plate is due to detached lithospheric mantle lying atop the oceanic slab. See text for more details.

structure and vice versa. Both, the anomalies in the mantle wedge, and in the crust could this way be imaged independently.

We interpret this fast, high-Q_p body as delaminating and probably detaching South American lithosphere that has been shortened and thickened beneath the Eastern Cordillera and parts of the Puna plateau. The cold, sub-crustal mantle sinks much faster than thermal diffusion times into the underlying hotter asthenosphere, causing the strong velocity and Q_p contrasts. Further south, at 24°S, where the mantle wedge is characterized by low v_p and low Q_p, and the slab appears to thicken above the Benioff zone, we suggest that detachment has already been completed with the cold continental lithosphere resting atop the subducted Nazca plate. The positive velocity anomaly of 6% to 8% can be explained by 500° to 700° difference in temperature [*Sobolev et al.*, 1996]. This is the difference between the cold lithosphere (800°) and hot asthenosphere (1300°). The contrast can be enhanced by chemical differences (e.g higher Mg content in the lithosphere) or due to partial melts in the asthenospheric mantle wedge, which is supported by high v_p/v_s ratios found there (Figure 4.30).

In contrast to pure thermal models [e.g., *Houseman et al.*, 1981], cold lithosphere is not gravitationally unstable per sé. In particular, the density of depleted lithosphere is lower than that for primitive mantle. This compositional variation may exceed the effect of thermal expansion and make lithosphere generally buoyant [*Kay & Kay*, 1993]. Yet, the underlying asthenosphere is likely to contain significant amounts of partial melts, because H_2O from the slab causes flux melting. This is supported by high v_p/v_s ratios and large low Q_p regions observed in the mantle wedge in this study. Presence of melts reduces density and viscosity, and thus probably allowing for the observed gravitational instability.

We interpret the low v_p and Q_p anomalies engulfing the detached lithosphere as expressions of viscous heating and decompressional melting due to rapid influx and ascent of hot asthenospheric mantle [*Schott et al.*, 2000]. Hot, fresh mantle at the base of the crust probably causes partial melting in the lower crust, responsible for the penetrating "hot" anomalies observed there. We also see very low P velocities in the upper-most crust and large positive station corrections for Q_p, pointing to a shallow low Q_p anomaly. Extensive shallow low velocity zones in the backarc crust have also been detected with tele-seismic receiver-functions [*Chmielowski et al.*, 1999; *Yuan et al.*, 2000]. They were interpreted as large regions of melt accumulation that may serve as sources for the large ignimbrite fields that have erupted in the backarc since the Miocene. Lithospheric delamination might be the ultimate heat source in the mantle that triggers large-scale crustal melting and widely observed felsic volcanism.

Kay & Kay [1993] and *Kay et al.* [1994] proposed loss of the lithospheric lid at around 26°S, just south of our study area, based on low Q_p mantle [*Whitman et al.*, 1992] and

eruptions of ocean-island-type basalts and calc-alkaline lavas 1 to 2 m.y. ago. Shoshonitic lavas, thought to have a lithospheric mantle source, are found up to 24°S , the southern limit of our delamination event. At 24°S, above a zone of low velocity and high attenuation in crust and mantle (Figure 4.30) stands the Quarternary strato-volcano Cerro Tuzgle. In its vicinity shoshonites as well as ocean-island-type basalts and ignimbrites occur [*Coira & Kay*, 1993]. We believe that this volcanism is the result of a recent detachment of lithosphere, of which the remains are now lying on top of the Nazca plate. The shoshonitic, ocean-island-type, and ignimbrite lavas probably accompanied delamination. The youngest, andesitic lavas could be subduction related, due to fluids released into the now hot asthenospheric mantle, from the vigorous earthquake cluster in 200 km depth. Because there is no mantle lid left, magmas can reach the surface, as they do 200 km to the west, in the volcanoes of the present volcanic arc.

There are further arguments for loss of lithosphere beneath the Puna. The Puna plateau has an average elevation of 4.5 km, almost 1 km higher than the Altiplano to the north. Yet new estimates for Moho depth from receiver-functions [*Yuan et al.*, 2000] indicate significantly thinner crust for the Puna (55–60 km vs. $\approx$70 km for the Altiplano). In addition, shortening estimates from cross-sectional balancing for the Puna are consistently lower than they are to the north for the Altiplano [*Kley & Monaldi*, 1998, Chapter 1,]. *Grier et al.* [1991] can explain only 30% of the crustal cross-sectional area due to tectonic shortening in the Puna. Even if shortening is underestimated, other mechanisms lifting the plateau are certainly required. A missing lithospheric root could explain the discrepancy.

Considering that the magnitude of lithospheric shortening across the Altiplano is much greater than that across the Puna, the Altiplano seems a likelier place for delamination to occur. Nonetheless, under the Altiplano a lithospheric lid appears to be still present[4] [*Whitman et al.*, 1992; *Myers et al.*, 1998], whereas beneath the Puna, lithosphere is, or is in the process of being completely removed. These two provinces are also distinguished by different styles of upper crustal foreland deformation [*Whitman et al.*, 1996, Chapter 1,]. *Allmendinger & Gubbels* [1996] interpret the thin-skinned deformation of the Altiplano foreland as indicative of a simple-shear mode of lithospheric shortening, and the thick-skinned deformation of the Puna and its foreland as an expression of pure-shear shortening. This means that beneath the Altiplano, strong Brazilian lithosphere may be underthrust as a whole, intact plate. In contrast, beneath the Puna shortening of the lithosphere is distributed. *Whitman et al.* [1996] suggest that segmentation of the plateau

---

[4]Yet, lithosphere beneath the Altiplano must have thinned, to some degree, too, considering the very high surface heat flow measured across the plateau. Additionally, simple geometrical considerations require also some loss of mantle lithosphere, because the amount of shortening would produce a lithospheric thickness that would not fit into the limited space provided by the mantle wedge.

and foreland reflect pre-Andean differences in the structure of crust and mantle lithosphere. Restriction of thick Paleozoic sedimentary sections and tin mineralization to the regions north of 23.5°S may constrain the limit of old cratonic basement [*Allmendinger & Gubbels*, 1996; *Whitman et al.*, 1996]. In contrast, crustal xenoliths from the Cretaceous Salta Rift east of the Puna point to high temperature in the crust and lithosphere at 90 Ma [*Lucassen et al.*, 1998]. The inherited different state of the Altiplano and Puna lithospheres and their different modes of deformation result in two fundamentally different lithospheric rheologies that might explain why large-scale detachment of mantle lithosphere takes place beneath the Puna but not beneath the Altiplano. Numerical modeling shows that a normal olivine rheology is too strong to allow for delamination [*Buck & Toksöz*, 1983; *Schott & Schmeling*, 1998]. The lithosphere has to be weakened (e.g. by faulting) to deform, detach and sink into the underlying mantle. Beneath the Altiplano, viscosity of the underthrust lithospheric plate may be too high to delaminate, although it may be eroded due to convection or subduction related volatiles.

We suggest that the present difference in lithospheric thickness between the Altiplano and Puna plateaus are not inherited, but due to loss of lithosphere beneath the Puna, which in turn is sanctioned by pre-Andean weak rheology and weakening due to pure shear deformation.

Chapter 5

Conclusions and Outlook

In this thesis earthquake data from local networks in the Central Andes have been analyzed. High precision locations from the PUNA network sharply define a Benioff zone where seismicity is not evenly distributed but released in energetic clusters and along lineaments. Strikes of nodal planes from focal mechanisms generally align along elongated structures defined by earthquake locations, suggesting that earthquakes occur on zones of weakness or along aligned faults or cracks inside the slab.

Crustal earthquakes occur along the fold and thrust belts of the foreland and Eastern Cordillera, and along and south of the El Toro-Olacapato-Calama (TOCL) lineament in the Puna. The activity along the TOCL suggests that this major shear zone is still active.

Travel time and spectral data of three temporary seismic arrays were inverted for v_p, v_p/v_s, and Q_p. The tomographic images reveal a seismically strong and cold forearc that is characterized by relatively high crustal velocities, normal v_p/v_s ratios in the crust and high Q_p values. High v_p/v_s ratios and relatively low P velocities, characteristic for hydrated peridotites, are found in the mantle wedge beneath the forearc. The eastern foreland crust, although only partly resolved, also shows relatively high Q_p values, indicative of low temperature. In between, crust and mantle beneath the Western Cordillera and Puna plateau, have generally low velocities, high v_p/v_s ratios, and low Q_p values. Especially strong anomalies for all three parameters are found beneath the Western Cordillera, probably expressions of active volcanism. Based on its seismic properties, the crust beneath the plateau appears hot and weak.

The lithosphere beneath the Atacama depression was found to be seismically very strong. It is believed to be an old, cold structure, that obstructs asthenospheric mantle to penetrate deeper into the wedge corner, and thus displaced the emplacement of the volcanic arc a hundred kilometer to the east. Although the block has clearly subsided, its seismic properties are hard to reconcile with extension and crustal thinning as has been suggested

in previous studies from shallow observations. Instead, it is proposed that the block subsides as a whole along weak zones, characterized by low velocities and low Q_p values, surrounding it. The mechanism of removing material from its base is speculative, but might be some sort of basal erosion due to the subducting plate.

Low Q_p anomalies appear to originate at the prominent earthquake clusters in 100 and 200 km depth. It is suggested that water is conveyed into the mantle wedge due to earthquake ruptures that may trigger hydro-fracturing. Water then fluxes melting in the hot mantle wedge. Melt ascent ways, as imaged by seismic Q_p, are not straight up to the base of volcanoes as is often implicitly assumed. Instead, melt sources are located on significantly different depth levels, and ascent ways follow different patterns and significant horizontal distances are covered.

Between 23°S and 24°S a high velocity, high Q_p structure beneath the Eastern Cordillera and eastern Puna is interpreted as delaminating and detaching continental lithosphere that has been thickened in the orogenic process. South of this structure, the mantle is characterized by low velocities, high v_p/v_s ratios, and low Q_p values. It is believed that here lithosphere originally underlying Andean crust has already been removed. This is supported by new estimates of crustal thickness and volcanic activity. It is proposed that lithospheric delamination beneath the Puna is sanctioned by inherited weak lithospheric rheology and weakening due to pure shear deformation.

From theoretical and experimental petro-physical relationships, it should be possible to derive the temperature field, distribution of melts and water content from the distribution of v_p, v_p/v_s, and Q_p and additional data like surface heat flow, gravity field, and mineral composition of xenoliths. This would be desirable and would allow more detailed and quantitative interpretations. Yet, resolution for absolute values of v_p, v_p/v_s, and Q_p from independent inversions might not be sufficient because of trade-offs and erroneous data. A joint inversion, in which the parameters are coupled by petro-physical relationships could provide a more consistent and correlated model, but could also disclose where petro-physical models are not in accordance with seismological data, and consequently should be modified.

The Q_p images suggest that the depth of source regions of arc magmas varies considerably along strike of the volcanic front (i.e. magmas at 22°S appear to originate in 100 km depth, at 24°S in 200 km depth). It should be possible to verify this based on geochemical tracers in primitive arc magmas. Such an independent validation would greatly endorse confidence in the tomographic results.

Bibliography

Abers, G., Hydrated subducted crust at 100 - 250 km depth, *Earth and Planetary Science Letters*, *176*, 323–330, 2000.

Aki, K., A. Christofferson, & E. Husebye, Determination of three-dimensional seismic structure of the lithosphere, *J. Geophys. Res.*, *82*, 277–296, 1977.

Allmendinger, R., & T. Gubbels, Pure and simple shear plateau uplift, Altiplano-Puna, Argentina and Bolivia, *Tectonophysics*, *259*, 1–13, 1996.

Allmendinger, R., V. A. Ramos, T. E. Jordan, M. Palma, & B. L. Isacks, Paleogeography and Andean structural geometry, northwest Argentina, *Tectonics*, *2*, 1–16, 1983.

Allmendinger, R., M. Strecker, J. Eremchuk, & P. Francis, Neotectonic deformation of the southern Puna Plateau, northwestern Argentina, *Journal of South American Earth Sciences*, *2*, 111–130, 1989.

Allmendinger, R., T. E. Jordan, S. M. Kay, & B. L. Isacks, The evolution of the Altiplano-Puna plateau of the central Andes, *Annu. Rev. Earth Planet. Sci.*, *25*, 139–174, 1997.

ANCORP Working Group, Seismic reflections image revealing offset of Andean subduction-zone earthquake locations into oceanic mantle, *Nature*, *397*, 341–344, 1999.

Barazangi, M., & B. Isacks, Spatial distribution of earthquakes and subduction of the Nazca plate beneath South America, *Geology*, *4*, 686–692, 1976.

Berckhemer, H., W. Kampfmann, E. Aulbach, & H. Schmeling, Shear modulus and Q of forsterite and dunite near partial melting from forced-oscillation experiments, *Phys. Earth and Plan. Int.*, *29*, 30–41, 1982.

Bird, P., Continental delamination and the Colorado plateau, *J. Geophys. Res.*, *84*, 7561–7571, 1979.

Bock, G., R. Kind, A. Rudloff, & G. Asch, Shear wave anisotropy in the upper mantle beneath the Nazca plate in northern Chile, *J. Geophys. Res.*, *103*, 24.333–23.345, 1998.

Bock, G., B. Schurr, & G. Asch, High-resolution receiver function image of the oceanic Moho in the subducting Nazca plate from converted waves, *Geophys. Res. Lett.*, *20*, 3929–3932, 2000.

Brune, J. N., Tectonic stress and the spectra of seismic shear waves from earthquakes, *J. Geophys. Res.*, *75*, 4.997–5.009, 1970.

Brune, J. N., Correction, *J. Geophys. Res.*, *76*, 5002, 1971.

Buck, W., & M. Toksöz, Thermal effects of continental collision: thickening a variable viscosity lithosphere, *Tectonophysics*, *100*, 53–69, 1983.

Cahill, T., & B. L. Isacks, Seismicity and shape of the subducted Nazca plate, *J. Geophys. Res.*, *97*, 17.503–17.529, 1992.

Cahill, T., B. Isacks, D. Whitman, J. Chatelain, A. Perez, & J. Chiu, Seismicity and tectonics in the Jujuy province northwestern Argentina, *Tectonics*, *11*, 944–959, 1992.

Chinn, D., & B. Isacks, Accurate source depths and focal mechanisms of shallow earthquakes in western South America and in the New Hebrides island arc, *Tectonics*, *2*, 529–563, 1983.

Chmielowski, J., G. Zandt, & C. Haberland, The central Andean Altiplano-Puna magma body, *Geophys. Res. Lett.*, *26*, 783–786, 1999.

Clemens, J., & C. Mawer, Granitic magma transport by fracture propagation, *Tectonophysics*, *204*, 339–360, 1992.

Coira, B., & S. M. Kay, Implications of Quaternary volcanism at Cerro Tuzgle for crustal and mantle evolution of the Puna Plateau, Central Andes, *Contrib. Mineral. Petrol.*, *113*, 40–58, 1993.

Coira, B., J. Davidson, C. Mpodozis, & V. Ramos, Tectonic and magmatic evolution of the Andes of northern Argentina and Chile, *Earth-Sciences Reviews*, *18*, 303–332, 1982.

Comte, D., M. Pardo, L. Dorbath, H. Haessler, L. Rivera, A. Cisternas, & L. Ponce, Crustal seismicity and subduction morphology around Antofagasta, Chile: preliminary results from a microearthquake survey, *Tectonophysics*, *205*, 13–22, 1992.

Comte, D., L. Dorbath, M. P. T. Monfret, H. Haessler, L. Rivera, M. Frogneux, B. Glass, & C. Meneses, A double-planed seismic zone in Arica, northern Chile using local seismic data: first approach, *Geophys. Res. Lett.*, *26*, 1965–1968, 1999.

Crosson, R. S., Crustal structure modeling of earthquake data 1, simultaneous least square estimation of hypocenter and velocity parameter, *J. Geophys. Res.*, *81*, 3036–3046, 1976.

Dahm, T., Numerical simulations of the propagation path and the arrest of fluid-filled fractures in the earth, *Geophys. J. Int.*, *141*, 623–638, 2000.

Davies, J. H., The role of hydraulic fractures and intermediate-depth earthquakes in generating subduction-zone magmatism, *Nature*, *398*, 142–145, 1999.

Davies, J. H., & D. Stevenson, Physical model of source region of subduction zone volcanics, *J. Geophys. Res.*, *97*, 2.037–2.070, 1992.

de Silva, S., Altiplano-Puna volcanic complex of the Central Andes, *Geology*, *17*, 1102–1106, 1989.

Delouis, B., et al., The $M_w = 8.0$ Antofagasta (northern Chile) earthquake of 30 July 1995: A precursor to the end of the large 1877 gap, *Bull. Seism. Soc. Am.*, *87*, 427–445, 1997.

DeMets, C., R. Gordon, D. Argus, & S. Stein, Current plate motions, *Geophys. J. Int.*, *101*, 425–478, 1990.

Dorbath, C., M. Granet, G. Poupinet, & C. Martinez, A teleseismic study of the Altiplano and the Eastern Cordillera in northern Bolivia: New constraints on a lithospheric model, *J. Geophys. Res.*, *98*, 9825–9844, 1993.

Eberhart-Phillips, D., Three-dimensional structure in northern California coast ranges from inversion of local earthquake arrival times, *Bull. Seism. Soc. Am.*, *76*, 1.025–1.052, 1986.

Eberhart-Phillips, D., Local earthquake tomography: earthquake source regions, in *Seismic Tomography: Theory and Practice*, edited by H. Iyer & K. Hirahara, pp. 613–643, Chapman and Hall, London, 1993.

Eberhart-Phillips, D., & A. J. Michael, Seismotectonics of the Loma Prieta, California, region determined from three-dimensional v_p, v_p/v_s, and seismicity, *J. Geophys. Res.*, *103*, 21.099–21.120, 1998.

Elliott, T., T. Plank, A. Zindler, W. White, & B. Bourbon, Element transport from slab to volcanic front at the mariana arc, *J. Geophys. Res.*, *102*, 14,991–15,019, 1997.

Engdahl, E., R. van der Hilst, & R. Buland, Global teleseismic earthquake relocation with improved travel times and procedures for depth determination, *Bull. Seism. Soc. Am.*, *88*, 722–743, 1998.

Evans, J., D. Eberhard-Phillips, & C. H. Thurber, User's manual for *simulps12* for imaging v_p and v_p/v_s: A derivative of the "Thurber" tomographic inversion *simul3* for local earthquakes and explosions, *Open File Report 94-431*, U.S. Geological Survey, 1994.

Fisher, K. M., E. M. Parmentier, A. R. Stine, & E. R. Wolf, Modeling anisotropy and plate-driven flow in the Tonga subduction zone back arc, *J. Geophys. Res., 105*, 16,181–16,191, 2000.

Flint, S., P. Turner, E. J. Jolley, & A. J. Hartley, Extensional tectonics in convergent margin basins: An example from the Salar de Atacama, Chilenian Andes, *GSA bulletin, 105*, 603–617, 1993.

Giese, P., E. Scheuber, F. Schilling, M. Schmitz, & P. Wigger, Crustal thickening processes in the Central Andes and the different natures of the Moho-discontinuity, *Journal of South American Earth Sciences, 12*, 201–220, 1999.

Gill, J. B., *Orogenic Andesites and Plate Tectonics*, Springer Verlag, Berlin, 1981.

Götze, H.-J., B. Lahmeyer, S. Schmidt, & S. Strunk, The lithospheric structure of the Central Andes (20-26°S) as inferred from interpretation of regional gravity, in *Tectonics of the Southern Central Andes - Structure and Evolution of an Active Continental Margin*, edited by K.-J. Reutter, E. Scheuber, & P.-J. Wigger, Springer, Berlin Heidelberg New York, 1994.

Graeber, F., Seismische Geschwindigkeiten und Hypozentren in den südlichen zentralen Anden aus der simultanen Inversion von Laufzeitdaten des seismologischen Experiments PISCO '94 in Nordchile, *Scientific Technical Report STR97/17*, GeoForschungsZentrum Potsdam, 1997.

Graeber, F., & G. Asch, Three-dimensional models of P-wave velocity and P-to-S-velocity ratio in the southern central Andes by simultaneous inversion of local earthquake data, *J. Geophys. Res., 104*, 20,237–20,256, 1999.

Grange, F., D. Hatzfeld, P. Cunningham, P. Molnar, S. Roecker, G. Suarez, A. Rodriguez, & L. Ocola, Tectonic implications of the microearthquake seismicity and fault plane solutions in southern Peru, *J. Geophys. Res., 89*, 6.139–6.152, 1984.

Green, H., & H. Houston, The mechanics of deep earthquakes, *Ann. Rev. Earth Sci., 23*, 169–213, 1995.

Gregory-Wodzicki, K. M., Uplift history of the Central and Northern Andes, *GSA Bulletin, 112*, 1091–1105, 2000.

Grier, M. E., J. A. Salfity, & R. Allmendinger, Andean reactivation of Cretaceous Salta rift northwestern Argentina, *Journal of South American Earth Sciences*, *4*, 351–372, 1991.

Gubbels, T. L., B. L. Isacks, & E. Farrar, High-level surfaces, plateau uplift, and foreland development, Bolivian central Andes, *Geology*, *21*, 695–698, 1993.

Haberland, C., Die Verteilung seismischer Absorption in den Zentralen Anden, Ph.D. thesis, Freie Universität Berlin, 1999.

Haberland, C., & A. Rietbrock, Attenuation tomography in the western central Andes: A detailed insight into the structure of a magmatic arc, *J. Geophys. Res.*, 2000, in press.

Haslinger, F., Velocity structure, seismicity, and seismotectonics of northwestern Greece between the Gulf of Arta and Zakynthos, Ph.D. thesis, ETH Zürich, 1998.

Hoke, L., D. Hilton, S. Lamb, K. Hammerschmidt, & H. Friedrichson, He^3 evidence for a wide zone of active mantle melting beneath the central Andes, *Earth and Planetary Science Letters*, *128*, 341–355, 1994.

Hoogerduijn, E. H. S., & R. L. M. Vissers, Dehydration-induced fracturing of eclogite-facies peridotites: implications for the mechanical behaviour of subducting oceanic lithosphere, *Tectonophysics*, *200*, 187–198, 1992.

Houseman, G. A., D. P. McKenzie, & P. Molnar, Convective instability of a thickened boundary layer and its relevance for thermal evolution of continental convergent belts, *J. Geophys. Res.*, *86*, 6115–6132, 1981.

Husen, S., E. Kissling, E. Flueh, & G. Asch, Accurate hypocentre determination in the seismogenic zone of the subducting Nazca plate in northern Chile using a combined on-/offshore network, *Geophys. J. Int.*, *138*, 687–701, 1999.

Isacks, B., Uplift of the central Andean plateau and bending of the Bolivian orocline, *J. Geophys. Res.*, *93*, 3.211–3.231, 1988.

Iwamori, H., Transportation of H_2O and melting in subduction zones, *Earth and Planetary Science Letters*, *160*, 65–80, 1998.

Jackson, I., M. S. Paterson, & J. D. Fitzgerald, Seismic wave dispersion and attenuation in Aheim dunite: an experimental study, *Geophys. J. Int.*, *108*, 517–534, 1992.

James, D. E., Andean crustal and upper mantle structure, *J. Geophys. Res.*, *76*, 3.246–3.271, 1971.

Kawamoto, T., & J. Holloway, Melting temperature and partial melt chemistry of H_2O-saturated mantle peridotite to 11 gigapascals, *Science*, *276*, 240–243, 1997.

Kay, R. W., & S. M. Kay, Delamination and delamination magmatism, *Tectonophysics*, *219*, 177–189, 1993.

Kay, S., B. Coira, & C. Mpodozis, Neogene magmatic evolution and the shape of the subducting oceanic slab beneath the central Andeab arc, in *IUGG 21th General assembly*, p. pp. A440, Int. Union Geod. Geophys., Boulder, Co., 1995.

Kay, S. M., B. Coira, & J. Viramonte, Young mafic back arc volcanic rocks as indicators of continental lithospheric delamination beneath the Argentine Puna plateau, central Andes, *J. Geophys. Res.*, *99*, 24.323–24.339, 1994.

Kennett, B. L. N., *IASPEI 1991 Seismological tables*, Bibliotech, Canberra, Australia, 1991.

Kirby, S., E. R. Engdahl, & R. Denlinger, Intermediate-depth intraslab earthquakes and arc volcanism as physical expression of crustal and uppermost mantle metamorphism in subducting slabs, in *Subduction: Top to Bottom*, edited by G. Bebout, D. Scholl, S. Kirby, & J. Platt, vol. 96, pp. 195–214, American Geophysical Union, 1996.

Kissling, E., Geotomography with local earthquakes, *Rev. Geophys.*, *26*, 659–698, 1988.

Kissling, E., & J. C. Lahr, Tomographic image of the Pacific slab under southern Alaska, *Eclogae geol. Helv.*, *84*, 297–315, 1991.

Kissling, E., W. Ellsworth, D. Eberhart-Phillips, & U. Kradolfer, Initial reference models in local earthquake tomography, *J. Geophys. Res.*, *99*, 19.635–19.646, 1994.

Kley, J., & C. Monaldi, Tectonic shortening and crustal thickness in the Central Andes: How good is correlation?, *Geology*, *26*, 723–726, 1998.

Kosarev, G., R. Kind, S. Sobolev, X. Yuan, W. Hanka, & S. Oreshin, Seismic evidence for detached lithospheric mantle beneath Tibet, *Science*, *283*, 1306–1309, 1999.

Kraemer, B., D. Adelmann, M. Alten, W. Schnurr, K. Erpenstein, E. Kiefer, P. van den Bogaard, & K. Goerler, Incorporation of the Paleogene foreland into the Neogene Puna plateau: The Salar de Antofalla area, NW Argentina, *Journal of South American Earth Sciences*, *12*, 157–182, 1999.

Lamb, S., L. Hoke, L. Kennan, & J. Dewey, Cenozoic evolution of the Central Andes in Bolivia and northern Chile, in *Orogeny Through Time*, edited by J.-P. Burg & M. Ford, The Geological Society, London, 1997.

Laube, N., & J. Springer, Crustal melting by ponding of mafic magmas: A numerical model, *J. Volcanol. Geotherm. Res.*, *81*, 19–35, 1998.

Lee, W., & J. Lahr, HYPO71 (revised): A computer program for determining hypocenter, magnitude, and first motion pattern of local earthquakes, *Open File Report 311*, U.S. Geological Survey, 1975.

Lucassen, F., S. Leverenz, G. Franz, J. Viramonte, & K. Mezger, Metamorphism, isotopic ages and composition of lower crustal granulite xenoliths from the Cretaceous Salta Rift, Argentina, *Contrib. Mineral. Petrol.*, *134*, 325–341, 1998.

Lucassen, F., G. Franz, & A. Laber, Permian high pressure rocks-the basement of the Sierra de Limón Verde in northern Chile, *Journal of South American Earth Sciences*, *12*, 183–199, 1999.

Marrett, R., & S. Emerman, The relations between faulting and mafic magmatism in the Altiplano-Puna plateau (central Andes), *Earth Plan. Sci. Lett.*, *112*, 53–59, 1992.

Marrett, R., R. Allmendinger, R. Alonso, & R. Drake, Late Cenocoic tectonic evolution of the Puna Plateau and adjacent foreland, northwestern Argentine Andes, *Journal of South American Earth Sciences*, *7*, 179–207, 1994.

Maurer, H., & U. Kradolfer, Hypocentral parameters and velocity estimation in the western Swiss Alps by simultaneous inversion of P- and S- wave data, *Bull. Seism. Soc. Am.*, *86*, 32–42, 1996.

Menke, W., *Geophysical Data Analysis: Discrete Inverse Theory*, Academic Press, San Diego, 1989.

Mibe, K., T. Fuji, & A. Yasuda, Control of the location of the volcanic front in island arcs by aqueous fluid connectivity in the mantle wedge, *Nature*, *401*, 259–262, 1999.

Michelini, A., & T. McEvilly, Seismological studies at Parkfield. I. Simultaneous inversion for velocity structure and hypocenters using cubic B-splines parameterization, *Bull. Seism. Soc. Am.*, *81*, 524–552, 1991.

Müller, R., W. Roest, J. Royer, L. Gahagan, & J. Sclater, Digital isochrons of the world's ocean floor, *J. Geophys. Res.*, *102*, 3.211–3.214, 1997.

Myers, S. C., S. Beck, G. Zandt, & T. Wallace, Lithospheric-scale structure across the Bolivian Andes from tomographic images of velocity and attenuation for P and S waves, *J. Geophys. Res.*, *103*, 21.233–21.252, 1998.

Park, J., C. R. Lindberg, & F. L. Vernon, Multitaper spectral analysis of high-frequency seismograms, *J. Geophys. Res.*, *92*, 12.675–12.684, 1987.

Parsons, B., & J. G. Sclater, Analysis of the variation of ocean floor bathymetry and heat flow with age, *J. Geophys. Res.*, *82*, 803–827, 1977.

Patzig, R., *Lokalbeben-Tomographie der Umgebung von Antofagasta (Nordchile)*, vol. 36 of *B*, Berliner Geowissenschaftliche Abhandlungen, 2000.

Patzwahl, R., J. Mechie, A. Schulze, & P. Giese, 2d-velocity models of the Nazca plate subduction zone between 20 and 25 degrees S from wide-angle seismic measurements during the CINCA95 project, *J. Geophys. Res.*, *104*, 7293–7317, 1999.

Pavlis, G., & J. R. Booker, The mixed discrete-continuous inverse problem: application to the simultaneous determination of earthquake hypocenters and velocity structure, *J. Geophys. Res.*, *85*, 4801–4810, 1980.

Peacock, S. M., Thermal and petrologic structure of subduction zones, in *Subduction: Top to Bottom*, edited by G. Bebout, D. Scholl, S. Kirby, & J. Platt, no. 96 in A, pp. 119–133, American Geophysical Union, 1996.

Podvin, P., & I. Lecomte, Finite difference computation of traveltimes in very contrasted velocity models; a massively parallel approach and its associated tools, *Geophys. J. Int.*, *105*, 271–284, 1991.

Poli, S., & M. W. Schmidt, H_2O transport and release in subduction zones: Experimental constraints on basaltic and andesitic systems, *J. Geophys. Res.*, *100*, 22.299–22.314, 1995.

Raleigh, C. B., Tectonic implications of serpentinite weakening, *Geophys. J. R. astr. Soc.*, *14*, 113–118, 1967.

Reasenberg, P. A., & D. Oppenheimer, FPFIT, FPLOT, and FPAGE - Fortran computer programs for calculating and displaying fault-plane solutions, *Open File Report 739*, U.S. Geological Survey, 1985.

Reutter, K.-J., & H.-J. Götze, Comments on the geological and geophysical maps, in *Tectonics of the Southern Central Andes - Structure and Evolution of an Active Continental Margin*, edited by K.-J. Reutter, E. Scheuber, & P.-J. Wigger, pp. 329–333, Springer, Berlin Heidelberg New York, 1994.

Reutter, K.-J., E. Scheuber, & G. Chong, The Precordilleran fault system of Chuquica-
mata, Northern Chile: evidence for reversals along arc-parallel strike-slip faults,
Tectonophysics, *259*, 213–228, 1996.

Rietbrock, A., Entwicklung eines Programmsystems zur konsistenten Auswertung großer
seismologischer Datensätze mit Anwendung auf die Untersuchung der Absorptionsstruk-
tur der Loma-Prieta-Region, Kalifornien, Ph.D. thesis, LMU München, 1996.

Rietbrock, A., *P*-wave attenuation structure in the fault area of the 1995 Kobe earthquake,
J. Geophys. Res., 2000, in press.

Rietbrock, A., & C. Haberland, ANCORP'96: Das passive seismologische Experiment,
in *Berichtsband für die Jahre 1996 - 1998*, pp. 470–479, Sonderforschungbereich 267:
Deformationsprozesse in den Anden, 1998.

Rietbrock, A., & F. Scherbaum, The GIANT analysis system, *Seismol. Res. Lett.*, *69*,
40–45, 1998.

Riller, U., I. Petrinovic, J. Ramelow, M. Strecker, & O. Oncken, Late Cenocoic tecton-
ism, caldera and plateau formation in the central Andes, *Earth and Planetary Science
Letters*, 2000, in press.

Roeder, D., Andean-age structure of Eastern Cordillera (province of La Paz, Bolivia),
Tectonics, *7*, 23–39, 1988.

Rudnick, R. L., & D. M. Fountain, Nature and composition of the continental crust: a
lower crustal perspective, *Rev. Geophys.*, *33*, 267–309, 1995.

Sarker, G., & G. A. Abers, Deep structure along the boundary of a collisional belt:
attenuation tomography of P and S waves in the Greater Caucasus, *Geophys. J. Int.*,
133, 326–340, 1998.

Scherbaum, F., Combined inversion for the three-dimensional Q structure and source
parameters using microearthquake spectra, *J. Geophys. Res.*, *90*, 12.423–12.438, 1990.

Scheuber, E., T. Bogdanic, A. Jensen, & K.-J. Reutter, Tectonic development of the north
Chilean Andes in relation to plate convergence and magmatism since the Jurassic,
in *Tectonics of the Southern Central Andes - Structure and Evolution of an Active
Continental Margin*, edited by K.-J. Reutter, E. Scheuber, & P.-J. Wigger, Springer,
Berlin Heidelberg New York, 1994.

Schmidt, M., & S. Poli, Experimentally based water budgets for dehydrating slabs and consequences for arc magma generation, *Earth and Planetary Science Letters*, *163*, 361–379, 1998.

Schmitz, M., A balanced model of the southern Central Andes, *Tectonics*, *13*, 484–492, 1994.

Schmitz, M., et al., The crustal structure beneath the Central Andean forearc and magmatic arc as derived from seismic studies – the PISCO 94 experiment in northern Chile (21°-23°S), *Journal of South American Earth Sciences*, *12*, 237–260, 1999.

Schott, B., & H. Schmeling, Delamination and detachment of a lithospheric root, *Tectonophysics*, *296*, 225–247, 1998.

Schott, B., D. Yuen, & H. Schmeling, The significance of shear heating in continetal delamination, *Phys. Earth and Plan. Int.*, *118*, 273–290, 2000.

Schreiber, U., & K. Schwab, Geochemistry of Quaternary shoshonitic lavas related to the Calama-Olacapato-El Toro Lineament, NW Argentina, *Journal of South American Earth Sciences*, *4*, 73–85, 1991.

Schurr, B., & J. Nàbĕlek, New techniques for analysis of earthquake sources from local array data with an application to the 1993 Scotts Mills, Oregon aftershock sequence, *Geophys. J. Int.*, *137*, 585–600, 1999.

Schurr, B., G. Asch, A. Rietbrock, R. Kind, M. Pardo, B. Heit, & T. Monfret, Seismicity and average velocity beneath the Argentine Puna, *Geophys. Res. Lett.*, *26*, 3025–3028, 1999.

Sebrier, M., J. Mercier, F. Megard, G. Laubacher, & E. Carey-Gailhardis, Quaternary normal and reverse faulting and the state of stress in the central Andes of south Peru, *Tectonics*, *4*, 739–780, 1985.

SFB-Berichtsband, *Berichtsband für die Jahre 1996 - 1998*, Sonderforschungbereich 267: Deformationsprozesse in den Anden, Berlin, 1998.

Sobiesiak, M., Fault plane structure of the Antofagasta, Chile earthquake of 1995, *Geophys. Res. Lett.*, *27*, 577–600, 2000.

Sobolev, S., & A. Babeyko, Modeling of mineralogical composition and elastic wave velocities in anhydrous magmatic rocks, *Surveys in Geophysics*, *15*, 515–544, 1994.

Sobolev, S., H. Zeyen, G. Stoll, F. Werling, R. Altherr, & K. Fuchs, Upper mantle temperatures from tomography of French Massiv Central including effects of composition, mineral reactions, anharmonicity, anelasticity, and partial melt, *Earth and Planetary Science Letters*, *139*, 147–163, 1996.

Spiegelman, M., Flow in deformable porous media. Part 1. Simple analysis., *J. Fluid Mech.*, *247*, 17–38, 1993.

Springer, M., & A. Förster, Heat-flow density across the Central Andean subduction zone, *Tectonophysics*, *291*, 123–139, 1998.

Tatsumi, Y., Migration of fluid phases and genesis of basalt magmas in subduction zones, *J. Geophys. Res.*, *94*, 4.697–4.707, 1989.

Thurber, C., Earthquake locations and three-dimensional crustal structure in the Coyote Lake area, central California, *J. Geophys. Res.*, *88*, 8.226–8.236, 1983.

Thurber, C., Local earthquake tomography: Velocities and v_p/v_s-theory, in *Seismic Tomography: Theory and Practice*, edited by H. Iyer & K. Hirahara, pp. 563–583, Chapman and Hall, London, 1993.

Thurber, C., & D. Eberhart-Phillips, Local earthquake tomography with flexible gridding, *Computers and Geosciences*, *25*, 809–818, 1999.

Ulmer, P., & V. Trommsdorff, Serpentine stability to mantle depths and subduction-related magmatism, *Science*, *268*, 858–861, 1995.

Um, J., & C. Thurber, A fast algorithm for two-point seismic ray tracing, *Bull. Seism. Soc. Am.*, *77*, 972–986, 1987.

Červený, V., I. Molotkov, & I. Psencĭk, *Ray method in seismology*, University of Karlova Press, Prague, Czechoslovakia, 1977.

Virieux, J., V. Farra, & R. Madariaga, Ray tracing for earthquake location in laterally heterogeneous media, *J. Geophys. Res.*, *93*, 6585–6599, 1988.

von Huene, R., & D. W. Scholl, Observations at convergent margins concerning sediment subduction, subduction erosion and the growth of continental crust, *Rev. Geophysics*, *29*, 279–316, 1991.

Watson, E. B., & A. Lupulescu, Aqueous fluid connectivity and chemical transport in clinopyroxene-rich rocks, *Earth and Planetary Science Letters*, *117*, 279–294, 1993.

Whitman, D., Moho geometry beneath the eastern margin of the Andes, northwest Argentina, and its implications to the effective elastic thickness of the Andean foreland, *J. Geophys. Res.*, *99*, 15.277–15.289, 1994.

Whitman, D., B. Isacks, J.-L. Chatelain, J.-M. Chiu, & A. Perez, Attenuation of high-frequency seismic waves beneath the central Andean plateau, *J. Geophys. Res.*, *97*, 19.929–19.947, 1992.

Whitman, D., B. L. Isacks, & S. M. Kay, Lithospheric structure and along-strike segmentation of the central Andean plateau: seismic Q, magmatism, flexure, topography and tectonics, *Tectonophysics*, *259*, 29–40, 1996.

Wiemer, S., & J. P. Benoit, Mapping the b-value at 100 km depth in the Alaska and New Zealand subduction zones, *Geophys. Res. Lett.*, *23*, 1557–1560, 1996.

Wigger, P. J., M. Araneda, P. Giese, W.-D. Heinsohn, P. Röwer, M. Schmitz, & J. Viramonte, The crustal structure along the Central Andean transect derived from seismic refraction investigations, in *Global Geoscience Transect 6*, edited by R. H. Omarini & H.-J. Götze, pp. 13–19, AGU Publication No. 192, 1991.

Wigger, P. J., et al., Variation of the crustal structure of the southern central Andes deduced from seismic refraction investigations, in *Tectonics of the Southern Central Andes*, edited by K.-J. Reutter, E. Scheuber, & P.-J. Wigger, pp. 23–48, Springer, Berlin Heidelberg New York, 1994.

Yuan, X., S. Sobolev, R. Kind, O. Oncken, & ANDES Research Group, Subduction and collision processes in the Central Andes constrained by converted seismic phases, *Nature*, *408*, 958–961, 2000.

Zandt, G., S. Beck, S. Ruppert, C. Ammon, D. Rock, E. Minerva, T. Wallace, & P. Silver, Anomalous crust of the Altiplano central Andes: constraints from broadband regional seismic waveforms, *Geophys. Res. Lett.*, *23*, 1.159–1.162, 1996.

Zhao, D., & A. Hasegawa, P wave tomographic imaging of the crust and upper mantle beneath the Japan islands, *J. Geophys. Res.*, *98*, 4333–4353, 1993.

List of Figures

List of Tables

Appendix A

Station corrections for PUNA stations

station name	P corr. [s]	S corr. [s]	station name	P corr. [s]	S corr. [s]	station name	P corr. [s]	S corr. [s]
ADG	0.24	1.0	LAQ	0.34	-0.10	RSA	0.34	0.52
ARI	-0.30	-0.48	LAS	0.03	0.04	SAC*	0.00	0.51
BUS	0.30	0.58	LIT	-0.53	-0.25	SAL	-0.08	-0.37
CAM	-0.01	0.22	MAR	0.09	0.20	SAT	-0.19	0.11
CAU	0.12	0.32	MIC	-2.08	-4.09	SDC	0.32	0.27
CHA	-0.08	n/a	MIR	-0.16	-0.27	SEY	-0.04	-0.15
COL	-0.88	-1.60	MLC	-0.28	0.22	SGR	0.38	0.28
CON	-0.93	-1.74	OLA	0.47	1.11	SHM	0.05	0.22
COR	0.05	-0.04	OR1	-0.35	-0.74	SIC	0.00	0.13
EIN	0.35	0.74	OR3	-0.93	-0.48	SMA	-0.66	-0.30
ELM	0.31	0.49	OR4	-1.83	-0.07	SOC	-0.30	-0.15
ESC	0.27	0.85	ORA	0.46	0.22	SOE	0.10	0.11
FUN	0.19	0.57	PAR	-2.19	-4.74	SON	0.30	0.49
GOR	-0.70	n/a	PDJ	0.24	1.21	SPQ	0.05	-0.01
GUA	0.19	n/a	PDM	0.02	-0.12	SRO	0.13	0.11
HUA	0.14	0.35	PGR	0.13	0.26	TAC	-0.13	-0.06
IRY	0.00	-0.28	PIR	0.08	0.68	TAN	0.11	0.76
JAR	-0.74	n/a	PUR	0.19	-0.04	TIL	-0.42	-0.02
JER	-0.34	-0.33	QUI	0.23	0.96	TOG	-0.11	-0.43
JUY	-0.01	-0.32	RAC	0.49	1.06	TUG	0.25	0.75
LAC	-0.10	0.42	ROS	0.27	0.00	WSA	-0.60	-0.84

Table A.1: Station corrections for PUNA stations from joint inversion of 1-D velocity, hypocenters, and station delays. P delay of station SAC* was constrained to zero.

Appendix B

Focal Parameter

origin time			latitude	longitude	depth	M_l	focal mechanism			P axis		T axis	
yymmdd	hhmm	ss.ss	[°]	[°]	[km]		strike	dip	rake	az	dip	az	dip
970917	0009	48.48	-24.2284	-67.1607	171.66	1.80	180.00	15.00	-60.00	229.12	57.3	65.46	31.64
970914	0055	54.83	-23.9637	-66.8473	200.98	2.10	195.00	25.00	-85.00	274.71	69.81	101.24	20.07
970917	0132	31.74	-24.0526	-66.8751	198.89	2.57	15.00	70.00	-100.00	268.93	63.66	112.75	24.36
970916	0202	36.65	-23.9477	-66.8232	200.96	2.75	170.00	25.00	-110.00	298.56	67.17	95.02	21.1
970914	0312	37.40	-23.1132	-66.5861	215.55	2.08	75.00	55.00	-170.00	291.15	30.41	31.99	17.76
970914	0417	13.30	-23.9537	-66.7822	199.78	1.82	200.00	25.00	-60.00	235.92	64.11	87.51	22.46
970919	0427	27.64	-24.1444	-67.1052	181.04	2.70	0.00	80.00	-100.00	257.95	53.96	98.54	34.26
970917	0441	48.06	-24.3101	-67.1537	178.24	3.12	125.00	20.00	-120.00	261.66	60.92	58.39	27.07
970919	0456	57.52	-21.9906	-65.9109	263.56	2.55	115.00	25.00	-150.00	292.98	52.21	69.68	29.44
970922	0502	31.76	-24.2623	-67.1978	169.86	1.72	10.00	80.00	-100.00	267.95	53.96	108.54	34.26
970912	0515	13.84	-24.1433	-67.0442	188.82	2.72	165.00	10.00	-150.00	324.79	49.27	127.44	39.42
970919	0519	21.57	-23.9411	-66.8265	199.13	2.26	140.00	20.00	-150.00	311.6	51.76	96.85	32.92
970918	0526	15.62	-23.4255	-66.7758	204.89	2.38	45.00	10.00	150.00	262.56	39.42	65.21	49.27
970919	0543	38.98	-23.9705	-67.1320	173.14	2.57	155.00	10.00	-90.00	245.00	55.00	65.00	35.00
970912	0601	46.76	-23.1629	-66.7971	203.17	2.09	10.00	65.00	-80.00	299.51	68.43	92.52	19.41
970916	0647	24.18	-23.9791	-66.8884	195.92	2.59	5.00	70.00	-100.00	258.93	63.66	102.75	24.36
970919	0657	21.06	-22.9279	-67.6577	134.52	2.05	155.00	75.00	-40.00	108.77	38.47	210.92	14.83
970917	0733	47.00	-23.8975	-66.7667	207.29	1.81	140.00	80.00	100.00	221.46	34.26	62.05	53.96
970916	0755	01.93	-24.1671	-67.1522	170.98	1.72	5.00	85.00	-100.00	264.2	49.06	104.12	39.2
970921	0817	00.50	-24.1858	-67.0612	182.34	2.15	10.00	35.00	-80.00	63.32	78.14	272.83	10.36
970922	0950	48.04	-24.1657	-67.1138	179.47	2.75	10.00	5.00	120.00	252.24	40.62	67.19	49.27
970922	0950	48.04	-24.1657	-67.1138	179.47	2.75	370.00	70.00	-100.00	263.93	63.66	107.75	24.36
970923	1048	37.98	-23.3258	-66.7752	209.15	1.85	130.00	25.00	-120.00	274.08	64.11	62.49	22.46
970913	1108	08.48	-24.1073	-66.9353	191.92	2.19	10.00	60.00	-110.00	239.2	68.28	114.36	12.82
970923	1121	23.81	-24.1482	-67.1037	181.73	2.06	205.00	25.00	-50.00	227.91	60.43	85.08	24.33
970921	1141	21.22	-23.4258	-66.7758	204.15	1.84	140.00	10.00	-150.00	299.79	49.27	102.44	39.42
970913	1152	21.02	-24.1970	-66.8790	197.74	2.54	125.00	60.00	-130.00	341.92	55.35	242.23	6.64
970922	1154	24.97	-24.0909	-66.7962	201.20	1.53	0.00	70.00	-100.00	253.93	63.66	97.75	24.36
970912	1214	44.85	-23.7384	-67.0709	191.85	2.67	20.00	60.00	-100.00	265.07	73.06	117.28	14.45
970923	1318	13.50	-23.9277	-67.0277	185.42	1.98	205.00	25.00	-60.00	240.92	64.11	92.51	22.46
970921	1357	23.02	-23.3416	-66.7777	201.02	1.84	135.00	90.00	80.00	234.85	44.14	35.15	44.14
970917	1403	19.51	-24.0276	-66.9628	192.25	1.92	145.00	90.00	90.00	235.00	45.00	55.00	45.00
970912	1517	19.44	-24.0199	-66.8217	204.55	3.02	35.00	55.00	-90.00	305.00	80.00	125.00	10.00
970923	1519	43.60	-24.1430	-67.1909	168.50	1.73	200.00	15.00	-60.00	249.12	57.3	85.46	31.64

origin time			latitude	longitude	depth	M_l	focal mechanism			P axis		T axis	
yymmdd	hhmm	ss.ss	[°]	[°]	[km]		strike	dip	rake	az	dip	az	dip
970922	1623	07.39	-23.8213	-66.6176	218.53	2.25	130.00	10.00	-150.00	289.79	49.27	92.44	39.42
970920	1721	47.97	-23.9057	-66.8357	199.79	2.63	0.00	65.00	-100.00	250.49	68.43	97.48	19.41
970919	1752	27.44	-23.3795	-66.7589	208.38	3.76	157.00	90.00	90.00	247.00	45.00	67.00	45.00
970918	1805	05.29	-23.9643	-66.8076	206.08	3.01	195.00	15.00	-60.00	244.12	57.3	80.46	31.64
970912	1910	51.87	-24.0114	-66.8221	206.60	2.96	10.00	75.00	-100.00	266.28	58.83	108.1	29.32
970921	1917	33.38	-23.1684	-66.8403	195.69	2.48	145.00	20.00	-130.00	294.55	58.18	86.19	28.63
970922	1954	32.55	-24.0331	-66.8746	190.44	2.04	180.00	65.00	90.00	270.00	20.00	90.00	70.00
970912	2159	21.07	-24.1503	-67.0563	181.24	2.74	15.00	20.00	100.00	277.2	25.23	88.42	64.51
970915	2223	44.34	-24.5039	-67.5323	136.61	1.65	155.00	90.00	-80.00	74.85	44.14	235.15	44.14
970916	2317	52.91	-24.1620	-67.0581	181.85	2.76	170.00	90.00	110.00	241.12	41.64	98.88	41.64
970916	2323	08.80	-24.0355	-66.8714	195.70	2.58	30.00	80.00	-90.00	300.00	55.00	120.00	35.00
970921	2332	19.20	-24.0287	-66.7890	200.12	2.22	145.00	90.00	100.00	225.15	44.14	64.85	44.14
970920	2335	03.49	-24.2305	-67.1549	175.23	3.60	174.00	28.00	-96.00	278.35	72.65	88.44	17.11
971117	0027	03.64	-24.3621	-67.0670	175.77	2.33	45.00	45.00	160.00	270.28	19.21	18.66	42.15
971117	0106	20.96	-24.0282	-66.8859	196.82	2.98	0.00	75.00	-100.00	256.28	58.83	98.1	29.32
971112	0135	05.00	-24.1279	-66.8272	198.68	2.51	5.00	65.00	-110.00	241.11	64.3	109.7	17.66
971111	0348	36.30	-23.4189	-66.7703	205.03	2.16	145.00	20.00	-130.00	294.55	58.18	86.19	28.63
971111	0455	36.90	-23.1393	-66.3487	234.64	1.87	155.00	25.00	-110.00	283.56	67.17	80.02	21.1
971112	0606	47.63	-22.5674	-66.2963	250.00	4.05	90.00	15.00	170.00	293.42	40.63	84.72	45.63
971111	0637	07.19	-22.6131	-66.2164	244.11	1.77	55.00	10.00	170.00	254.29	42.46	54.85	45.86
971117	0645	37.15	-24.2268	-67.0346	186.90	2.05	365.00	55.00	-130.00	215.58	58.13	122.06	2.19
971116	0651	15.22	-23.9770	-66.7520	203.98	3.62	10.00	80.00	-100.00	267.95	53.96	108.54	34.26
971119	0751	16.99	-24.0363	-66.9787	190.39	2.32	160.00	60.00	150.00	32.19	2.71	124.57	41.28
971112	0924	28.96	-24.2248	-67.0800	183.74	1.96	105.00	50.00	-130.00	308.06	60.4	42.06	2.27
971111	1027	04.70	-24.2130	-67.0729	177.40	1.59	5.00	65.00	-110.00	241.11	64.3	109.7	17.66
971117	1453	31.75	-24.0707	-66.8073	200.26	2.75	170.00	15.00	-100.00	274.08	59.68	88.17	30.18
971115	1546	02.18	-23.3182	-66.7386	210.93	1.76	150.00	20.00	-110.00	272.3	63.09	75.6	25.93
971115	1554	13.30	-24.2259	-66.9782	189.77	1.49	140.00	15.00	-120.00	270.88	57.3	74.54	31.64
971119	1722	18.27	-24.2581	-67.1821	174.12	2.49	180.00	55.00	150.00	51.94	6.66	148.42	44.04
971111	1754	11.74	-23.9951	-66.8277	204.96	2.10	15.00	70.00	-90.00	285.00	65.00	105.00	25.00
971116	1905	51.87	-24.1005	-66.8048	203.09	2.35	215.00	40.00	-80.00	247.73	81.61	117.92	5.4
971112	2124	03.58	-24.0404	-67.0029	186.27	2.58	65.00	70.00	-90.00	335.00	65.00	155.00	25.00
971112	2146	27.66	-23.6475	-66.8601	208.35	2.60	170.00	20.00	-100.00	276.58	64.51	87.8	25.23
971110	2226	18.41	-24.1580	-66.8575	197.62	2.41	21.00	56.00	-99.00	261.52	77.01	117.46	10.58
971116	2300	17.93	-24.2820	-67.1187	178.20	2.86	10.00	75.00	-110.00	254.67	55.57	115.79	27.31
971115	2157	59.02	-24.2881	-67.2049	174.70	2.94	70.00	70.00	20.00	21.65	0.84	291.2	27.98

Table B.1: Focal parameters for intermediate depth earthquakes from Figure 3.4, determined from first motion polarities.

origin time			latitude	longitude	depth	M_w	focal mechanism			P axis		T axis	
yymmdd	hhmm	ss.ss	[°]	[°]	[km]		strike	dip	rake	az	dip	az	dip
971105	1135	07.02	-24.4412	-66.0951	8.26	1.54	137.00	74.00	-22.00	94.00	27.00	186.00	3.00
971107	0219	14.17	-24.4393	-66.0968	7.96	1.69	223.00	50.00	159.00	90.00	15.00	193.00	41.00

Table B.2: Focal parameters for two crustal earthquakes from Figure 3.5, determined by waveform inversion.
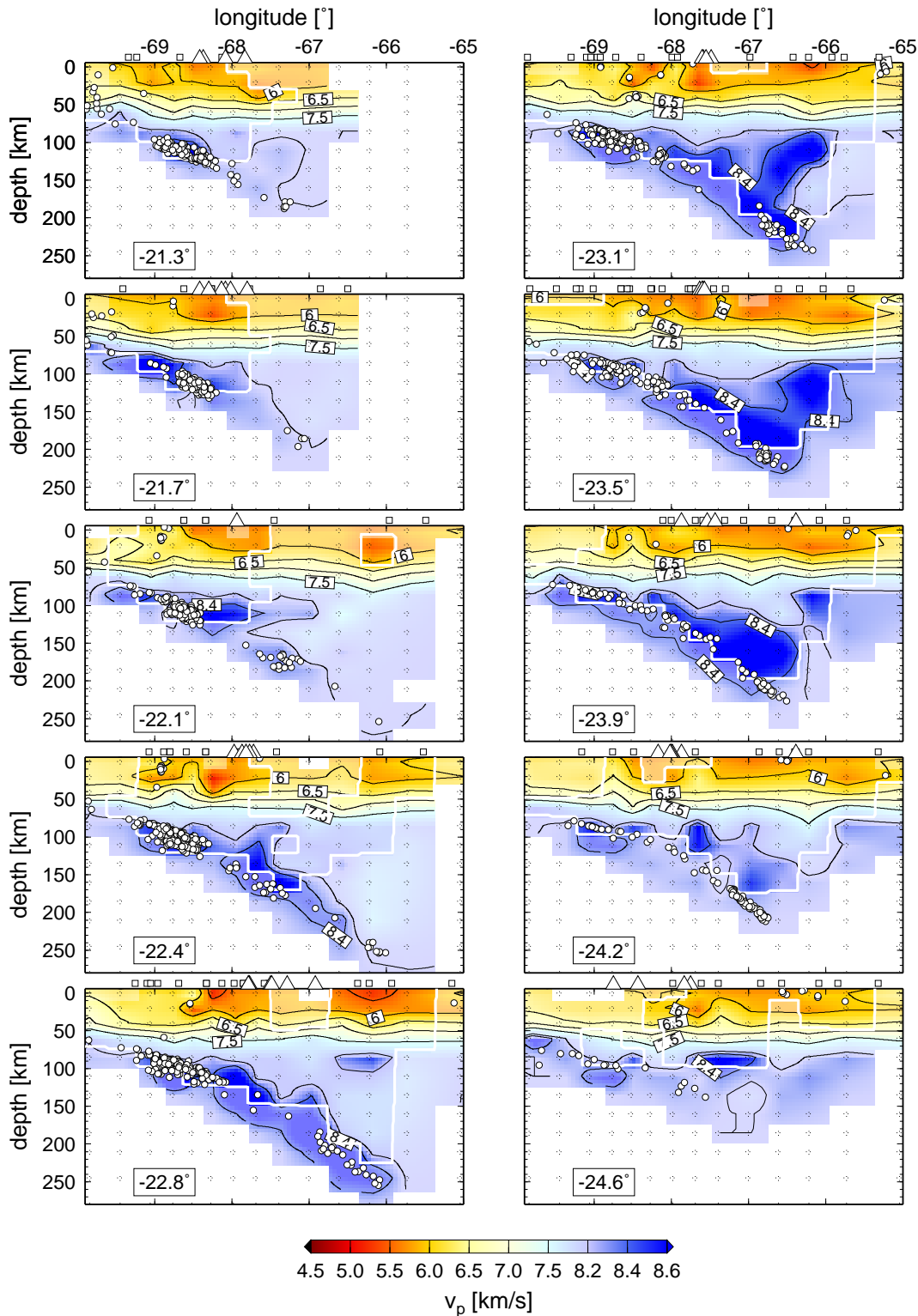
Appendix C

Absolute velocities

Figure C.1: West-east depth sections through the 3-D v_p model. Latitude of sections is indicated in the lower left corner. Earthquakes, stations, and volcanoes within 20 km of the section are also plotted. The thick white contour encloses regions of good resolution defined by the spread value. Regions of poor resolution are displayed in slightly faded colour.

Acknowledgments

Curriculum Vitae

<u>Personal Data</u>

Name:	<u>Bernd</u> Dieter Schurr
Born:	November 8th 1968 in Waiblingen

<u>Education</u>

1975 – 1979	Grundschule in Waiblingen-Hohenacker
1979 – 1988	Staufer-Gymnasium, Waiblingen
06/1988	Allgemeine Hochschulreife (Abitur)
1990 – 1993	Studienfach Geophysik, Universität Karlsruhe
10/1992	Vordiplom Geophysik
1993 – 1997	Geophysics at Oregon State University, Corvallis, U.S.A.
01/1997	M.Sc. in geophysics

<u>Professional Experience/Internships</u>

1988 – 1990	Civil service at the SOS Kinderdorf Württemberg
06/1995 – 02/1996	Internship at *Paradigm Geophysical Inc.* in Houston, Texas and Tel Aviv, Israel
01/1997 – 06/1997	Research assistant at the Oregon State University, Corvallis
07/1997 – 10/2000	Research assistant at the GeoForschungsZentrum Potsdam